State Estimation for Nanosatellite-Class Reaction Wheels

R.F. Florea

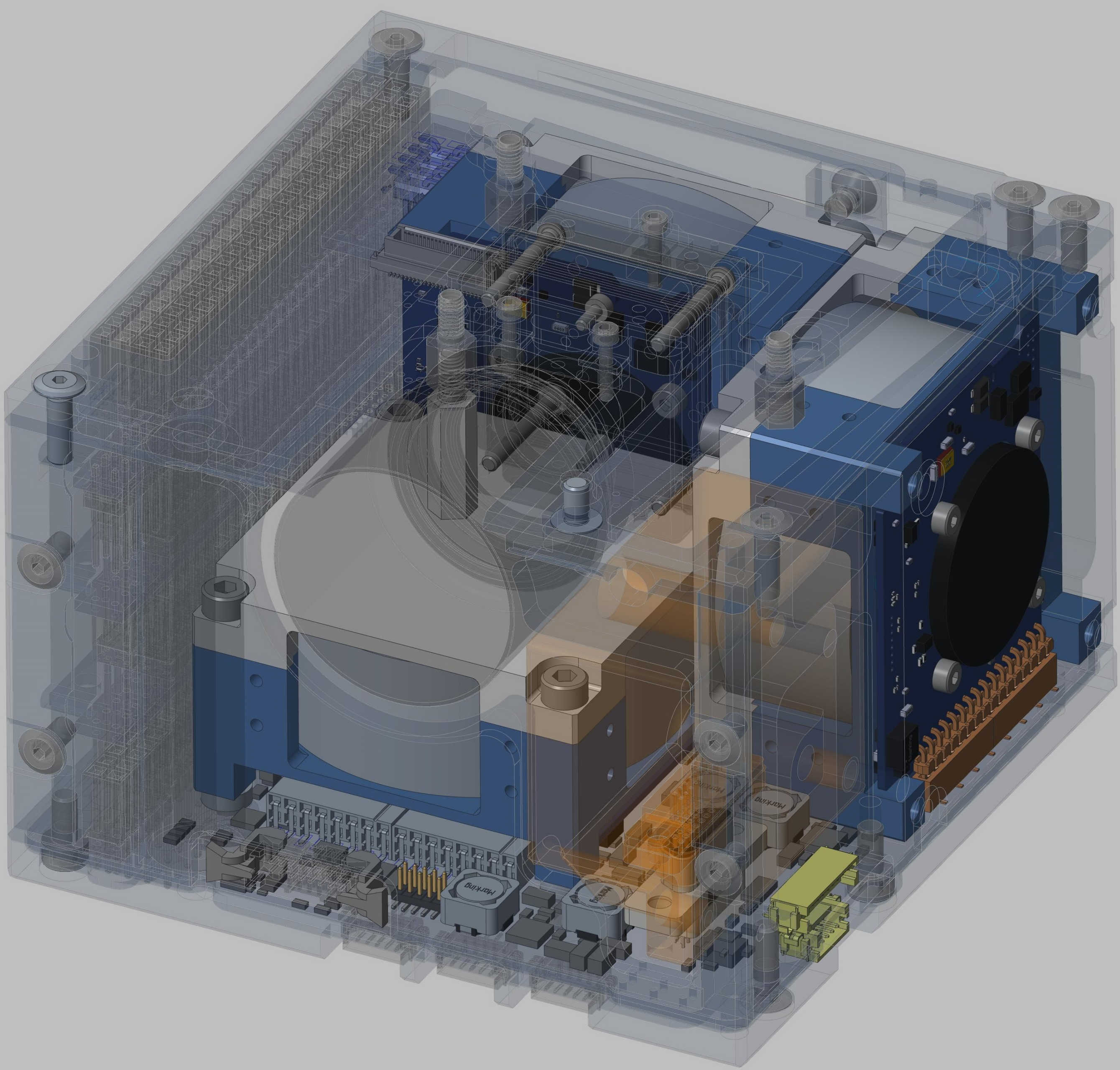

Technische Universiteit Delft

TUDelft

State Estimation for Nanosatellite-Class Reaction Wheels

by

R.F. Florea

in partial fulfilment of the requirements for the degree of

Master of Science
in Systems and Control

at Delft University of Technology,
to be defended publicly on Tuesday, December 18th, 2018, at 09:00.

Student number:	4330358	
Supervisor:	Prof. Dr. Ir. J. Hellendoorn,	TU Delft
Thesis committee:	Prof. Dr. Ir. J. Hellendoorn (chair),	TU Delft
	Dr. S. Baldi,	TU Delft
	Dr. S.H. Hossein Nia Kani,	TU Delft
Guest members:	Dr. Ir. G.L.E. Monna,	Hyperion Technologies
	Dr. Ir. S. Engelen,	Hyperion Technologies

This thesis is confidential and cannot be made public until December 18, 2023.

Cover photo credit: ir. M. Klein, Hyperion Technologies

TU Delft

Summary

In recent years, nanosatellites have seen a significant boost in their usage for both scientific, as well as commercial missions/applications. These nanosatellites are based on the CubeSat form factor, which has become the industry standard when it comes to the design and integration of nanosatellites.

The standardisation of this satellite class has led to the development of a variety of plug-and-play, commercial off-the-shelf subsystems. This has resulted in the decrease of the time and cost associated with satellite design, manufacturing, and integration.

Prompted by the emergence of a strong ecosystem around CubeSat-type satellites, missions with increasing performance requirements are being developed. Missions involving earth-imaging, space telescopy, or laser communication, to name a few, require high accuracy pointing of the satellite. Thus, they require high performance attitude determination and control systems.

Reaction wheels are the main satellite attitude actuators. Therefore, in order to satisfy the stringent pointing accuracy requirements of different space missions, high accuracy, low torque ripple control of the reaction wheel angular velocity is essential. Hyperion Technologies aims to achieve the necessary control accuracy for its HT-RW4xx reaction wheel system.

Due to the high level of integration specific to nanosatellite subsystems, the reaction wheels designed for such a platform must compromise on the amount and on the accuracy of the sensors it uses. As a result, the HT-RW4xx makes use of three digital Hall-effect sensors to obtain rotor position information, and to compute its angular velocity.

In order to achieve a highly precise control of the wheel's angular velocity, while maintaining low torque ripple levels, high resolution, high accuracy information of the reaction wheel angular position, velocity, and phase currents is critical. Seeing that the Hall-effect sensors do not meet the needed high accuracy and resolution measurements of the position and velocity, two linear parameter varying state estimators are designed to satisfy the requirements, and have a good robustness in the face of reaction wheel disturbances.

The first state estimator is designed using phase current measurements, as well as Hall sensor based position and velocity measurements. The second estimator is designed using only the Hall sensor position and velocity measurements. The angular position and velocity estimates of the first observer have a standard deviation of $\sigma_{\theta_e} = 2.554 \cdot 10^{-4}\ rad$, and $\sigma_{\omega_m} = 2.191 \cdot 10^{-3}\ rad/s$, respectively, when the wheel is in steady-state operation. The second observer gives angular position and velocity estimates that have a standard deviation of $\sigma_{\theta_e} = 6.605 \cdot 10^{-3}\ rad$, and $\sigma_{\omega_m} = 7.392 \cdot 10^{-3}\ rad/s$, respectively, again, when the wheel is operating in steady-state.

Both state estimators have a good performance in the face of reaction wheel friction torque variations, and micro-vibrations. The disturbance created by the stator coil resistance variation is more difficult to address. The first observer, making use of the phase current measurements, is able to eventually eliminate the error, caused by this disturbance, from the state estimates.

Preface

This document represents the final report of my Master of Science thesis project. With it, the conclusion of my university graduate studies is all but here. It has been a long journey, with many bumps along the way. But it was worth it. It has enriched me, it gave me the opportunity to meet and form friendships with so many great people, and it has prepared me to take on the world with more ease (at least I like to think so).

I would like to thank my supervisor, Hans Hellendoorn, for his incredible understanding, support, and steady friendly pressure that helped me find my way to the final moment of this thesis. Without his help and guidance things would have been much more difficult. I am very grateful for all his help.

My gratitude goes to Bert Monna, for his trust in me throughout this whole time, for always pushing me to explore a problem from a different angle/with a different perspective, and for all those awesome monthly company barbecues. A big thank you to Steven Engelen for all the interesting discussions, opening me up to the space industry, and showing me how every day is a Monday. Thank you to Cor in 't Veld for all his help with software related tasks, but also for all the good spirited weekend conversations.

I would also like to thank Hassan Hossein Nia Kani and Simone Baldi for taking the time out of their busy schedules to read my thesis, and making themselves available on such short notice.

Special thank you to everyone from Delft Aerospace Rocket Engineering (DARE), especially the Stratos II propulsion team. They have made my time at the TU Delft joyful, while getting to experience truly unique moments. Thank you to all the other people from Hyperion Technologies for simply being nice and accepting of my randomness. To all my friends, thank you for your support and for being you.

I want to express my deepest and most sincere gratitude to my parents and grandparents for their relentless support, for always sending way too much food all the way from Romania, for always taking so long to end a call. Last, but not least, I want to thank Daniela Hallak from the bottom of my heart for always being there for me, picking me up when I needed it the most, looking out for me, and overall putting up with me.

R.F. Florea
Delft, December 2018

Contents

List of Figures

List of Tables

1
Introduction

Curiosity is one of the prevalent traits of humankind. This drive for discovery has pushed humanity towards ever greater discoveries. Starting with the launch of Sputnik 1, the world's first artificial satellite, the desire to travel and explore the mysteries that lie beyond the Earth's sky has been ever increasing, thus, sparking major advancements in the field of space technology throughout the years.

Benefiting from the continuous development of space technology, satellites have become widely employed in both civil and military applications. An important milestone in satellite development and applications is the definition of the CubeSat reference design by professors Jordi Puig-Suari and Bob Twiggs, in 1999. The design makes use of the so-called CubeSat unit (a $10cm \times 10cm \times 10cm$ cube, referred to as $1U$) to define the dimension of the satellite [4]. The CubeSat reference design eventually evolved into the standard design for both academic and commercial nano-satellites. This is due to the fact that the design allowed for the development of standardized subsystems, resulting in the emergence of readily available commercial off-the-shelf (COTS) subsystems. Thus, leading to a reduction in the development time of a satellite, as well as its overall cost.

Although, at first, CubeSats were mainly being built by universities and research institutes, commercial companies are launching an increasing amount of CubeSats. This is best showcased by companies such as Planet and Spire Global, which have launched 324 and 85 CubeSats, respectively, within five years of operation[1].

Proving its commercial feasibility, the CubeSat standard is employed in missions with increasingly stringent requirements on volume, power consumption, pointing accuracy, vibrations, etc. These highly demanding requirements are fuelling the development of miniaturised, highly integrated, high performance subsystems. The satellite's attitude determination and control system (ADCS) is one of the subsystems most affected by increasingly strict requirements, the most important being its achievable pointing accuracy [8]. The ADCS controls the orientation (also known as attitude) of the satellite, by first determining its orientation with the help of attitude sensors, and then adjusts the orientation through the use of attitude actuators.

The overall pointing accuracy of the ADCS is determined by numerous factors. First, and foremost, the measurements obtained from the absolute attitude sensors (e.g. star trackers, sun sensors) must be of sufficiently high accuracy. Secondly, the relative attitude sensors (e.g. accelerometers, gyros) must also provide measurements of an adequately high accuracy. Lastly, the torque generated by the attitude actuators must be highly smooth (low torque ripple), and of sufficient amount such that the satellite is maintained at the desired attitude, with the required accuracy [8].

Reaction wheels (RWs) are one of the main actuators used on satellites, and are present on almost every fine-pointing Earth-observing missions [24], as well as on majority of deep space missions [20]. Reaction wheels are flywheels that make use of the conservation of momentum principle to control the

[1]Source: https://www.nanosats.eu/tables.html#constellations, accessed 01-12-2018.

orientation of the satellite. Therefore, high accuracy control of the RW angular velocity is necessary in order to meet stringent pointing accuracy requirements.

In Section 1.1 of this chapter, the challenges facing accurate angular velocity control of reaction wheels are discussed, and the objectives of this thesis are formulated. The thesis outline is then given in Section 1.2.

1.1. High Performance Reaction Wheels Challenges and Thesis Objective Formulation

Angular velocity control for classical reaction wheels is rather straightforward, since, due to their comparatively larger dimensions, there is enough room for a high amount of rotor position sensors, angular velocity sensors, current sensors, temperature sensors, etc. Moreover, the wheel drive electronics (WDE) are not necessarily always integrated into the reaction wheel, leaving even more space in the RW unit itself.

However, when the reaction wheel system is required to be miniaturized, the space available for rotor position sensors, current sensors, and temperature sensors becomes nearly non-existent. Additionally, the WDE are required to be integrated into the reaction wheel.

This leads to reaction wheel designs that have the bare minimum in terms of instrumentation, i.e. just enough to be able to operate. This is especially bad for the rotor position measurements, which, for miniaturized wheels, is performed by three digital Hall sensors. This results in an extremely low-resolution ($pi/3\ rad$) measurement of the most important piece of information for motor commutation, the angular position. Furthermore, the placement of these Hall sensors is in fact inaccurate, resulting in a biased position measurement.

Apart from the issues created by the use of three digital Hall sensors for angular position measurements, miniaturized reaction wheels are also susceptible to friction variation [7]. In fact, friction related disturbances have a significant contribution to the degradation of the pointing accuracy of satellites, as discussed in [14], and in [17]. Moreover, in [7] it is concluded that an integrated speed controller in the reaction wheel drive electronics reduces the impact of wheel friction transients on the pointing accuracy of the satellite. Additionally, micro-vibration disturbances and operating temperature variation have a significant impact on the control performance of the wheel.

Reaction wheel control can be separated into three interconnected parts (see Figure 1.1), where each part can be tackled separately. As can be observed from Figure 1.1, the state estimation block provides accurate estimations of the phase currents, rotation speed, and rotor position, all of which are required for adequate phase commutation, and for speed control. It can, thus, be viewed as the main component/building block in the high accuracy control of high performance reaction wheels.

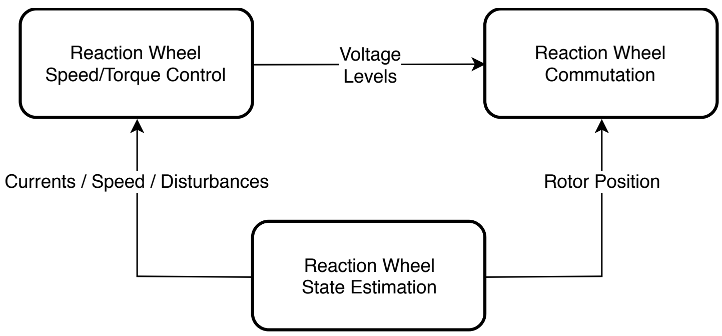

Figure 1.1: The three parts in the control of high accuracy reaction wheels

Having a background in highly integrated, high performance nanosatellite subsystem, Hyperion Technologies aims to achieve the necessary control accuracy for its HT-RW4xx reaction wheel system. The following thesis project aims to provide the stepping-stone for this goal, by developing a detailed model of the HT-RW4xx reaction wheel, and a state estimator that is able to provide high accuracy information, to be utilised in the control of the reaction wheel. The goal of the thesis project is then formulated as follows:

> The goal of this thesis is to obtain an accurate, un-biased estimation of the HT-RW4xx reaction wheel states that is robust against reaction wheel specific disturbances, and parameter variations that appear due to rotor imbalance, bearing vibration, lubricant viscosity, operating temperature, and zero-speed crossings, while using a minimal amount of sensors.

In order to achieve the main thesis goal, the following secondary objectives are formulated:

1. Create a detailed simulation of the HT-RW4xx reaction wheel.
2. Design a reaction wheel state observer that is able to account for changing system parameters.
3. Compare the performance of an observer designed using all available sensors, to the performance of an observer designed using only Hall-sensor base measurements.

To achieve these objectives, a three-phase model of the reaction wheel system is created first. The reaction wheel model includes a model of the angular position, and angular velocity measurements performed using the three digital Hall sensors that the HT-RW4xx contains. A detailed characterisation campaign is performed on the wheel in order to obtain information about the various disturbances that are present in the unit. The reaction wheel simulation is then updated with disturbance models based on the gathered data.

Seeing that some of the wheel parameters vary over time, a linear parameter varying (LPV) approach is selected for the state observer design. Synthesis of the observer is then performed through the use of linear matrix inequality (LMI) methods.

The performance of the two synthesised observers is then evaluated by analysing their estimation accuracies, behaviour during zero-speed transitions, as well as robustness to friction and coil resistance mismatch.

1.2. Thesis Outline

The thesis starts with the detailed modelling of the reaction wheel, described in Chapter 2. A good model of the reaction wheel is highly desirable as it allows for the quick and adequate evaluation of the to-be-designed state observer. Moreover, it reduces the time necessary for modifying and re-flashing firmware on the RW drive electronics.

The model developed in Chapter 2 is further improved by conducting a thorough characterisation campaign on the reaction wheel, in order to determine all the disturbances acting on them. The tests (thermal cycling, micro-vibration, etc.) conducted throughout this test campaign, together with their results, are discussed in detail in Chapter 3. Furthermore, disturbance models based on the gathered experimental data are proposed, and integrated into the reaction wheel simulation.

In the first part of Chapter 4, the Hall sensor position estimation algorithm is described, and its performance is evaluated. The second part of Chapter 4 focuses on the design and synthesis of the LPV observer, formulated as an optimization problem. Two observers are designed: one using current measurements, as well as Hall-sensor based angular position and velocity measurement; the other using only Hall-sensor based measurements of the angular position and velocity. The performance of these two observers is then compared for a few representative cases in the reaction wheel's operation.

Lastly, conclusions related to the work performed throughout this thesis project are drawn in Chapter 5. Additionally, recommendations for further work and improvement of the reaction wheel simulation, and, especially, of the state estimator are given in the same chapter.

2

Modelling and Characterisation of Reaction Wheels Driven by Brushless Motors

The first electric motor to be successfully introduced in industry was invented by Zénobe Gramme in 1873. It was followed soon by the first brushless motor, patented by Nikola Tesla in 1888 (a two-phase alternating current motor). Throughout the years, electric motors have become the major workhorse in a multitude of fields, obtaining a key role in all industries.

Following the development of the space industry, brushless motors have been given special interest for space applications due to the lack of a physical commutator. This offers a significant increase in mechanism lifetimes, while also eliminating the electrical arcing of the commutator brushes, which affects the performance of the surrounding instrumentation on-board the spacecraft. The importance of brushless motors in space applications is especially highlighted with the development of the first brushless direct current motors (BLDCM) by the National Aeronautics and Space Administration (NASA), in the 1960s.

Throughout this chapter, a simulation of the Hyperion Technologies HT-RW4xx reaction wheel series is developed. This simulation can then be used to evaluate the performance of the state observers that are to be designed in Chapter 4. Section 2.1 offers a brief discussion on brushless motor integration into reaction wheel systems, including the construction and operation of BLDCMs. This is followed, in Section 2.2, by a detailed model of the HT-RW4xx reaction wheels, accounting for the free-wheeling diode effect in the voltage source inverter, as well as Hall sensor hysteresis and placement error. In Section 2.3, the reaction wheel is characterised in order to obtain better approximations of the Hall sensor placement error, the magnetic flux distribution, and of the nominal wheel friction profile.

2.1. Brushless Motors in Reaction Wheels

Reaction wheels are among the mechanisms that greatly benefit from the development of BLDCMs, due to the high rotation speeds and overall operational life requirements. A reaction wheel is, in essence, a mass with a high moment of inertia, spun by a brushless DC motor, controlled by the WDE, as can be observed in Figure 2.1. Therefore, for all modelling purposes, the wheel can simply be treated as a BLDCM with a high inertia rotor. It is evident that technological advancement and innovation in the field of motor control algorithms and electronics, brings an invaluable benefit to the development of reaction wheels.

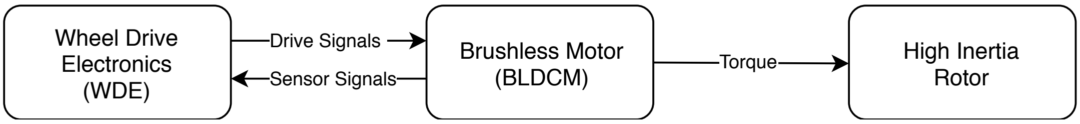

Figure 2.1: Reaction wheel system schematic.

In Section 2.1.1, insight is given into the design choices that can be made for a reaction wheel. Different types of brushless motors, together with their advantages and disadvantages, that can be utilized in a reaction wheel are discussed, as well as the possible options for rotor position sensors. Section 2.1.2 then gives an explanation of the working principle behind driving the reaction wheel.

2.1.1. Reaction Wheel Construction

The general outline of BLDCM powered reaction wheels is the following: permanent magnets attached to rotor with a high moment of inertia; stator containing the motor coils, and the rotor position sensors.

Different types of brushless DC motors have been developed over time, each type being better suited for certain applications. These motor types are classified based on the placement of their permanent magnet rotors with respect to their stator, i.e.: in-runner motors, for which the rotor is internal to the stator; out-runner motors, having the rotor external to the stator; pancake motors, which have an axial magnetic field design, thus, the rotor is placed on top of the stator. The in-runner and out-runner motor types are presented in Figure 2.2, while the pancake motor type is presented in Figure 2.3(b).

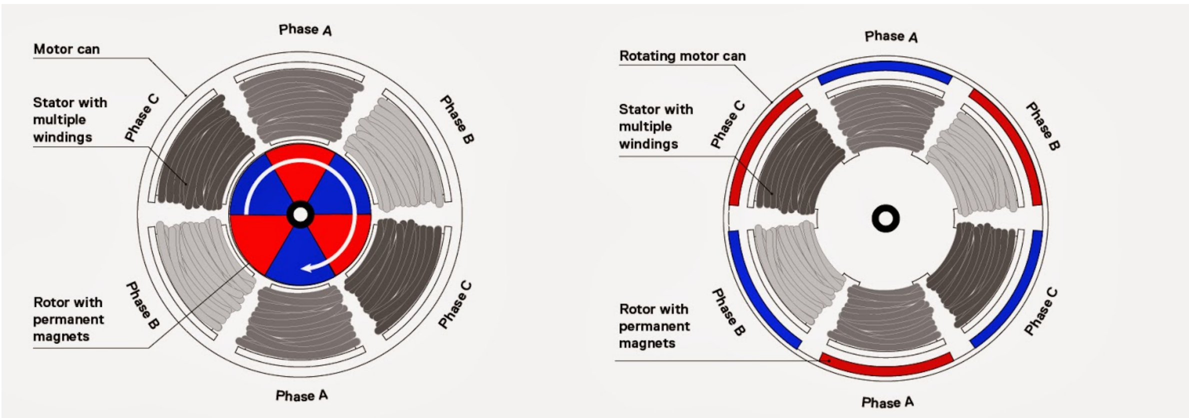

(a) In-runner brushless DC motor. (b) Out-runner brushless DC motor.

Figure 2.2: The two main brushless motor configurations[1].

New reaction wheel designs, most of them aimed at the nano- and small- satellites market, are subjected to extremely challenging requirements, such as high momentum storage in a small form factor, low and very-low power consumption, integrated wheel drive electronics, etc. Based on these requirements, various design choices are made, which impact the wheel's motor.

Classical space reaction wheel designs make use of custom-made motors to power them. However, with nowadays NewSpace philosophy, COTS motors are benefiting from an increase in popularity. This is due to a shorter time-to-market of reaction wheels, since motor development time is ultimately eliminated from the total reaction wheel development time. Evidently, designing a new, custom motor would allow for a better performing reaction wheel. However, the choice to go for a COTS motor or for a custom one, ultimately boils down to a trade-off between development time and reaction wheel performance.

Although BLDCMs of any configuration type can be used to drive the wheel, employing out-runner type motors results in a simpler and more efficient reaction wheel design. As can be observed from Figure 2.3, apart from out-runner motors, pancake motors could form analternative, especially for miniature reaction wheels.

[1]URL: http://www.rclab.info/2014/01/the-basics-of-electric-power-brushless.html [retrieved July 2018]

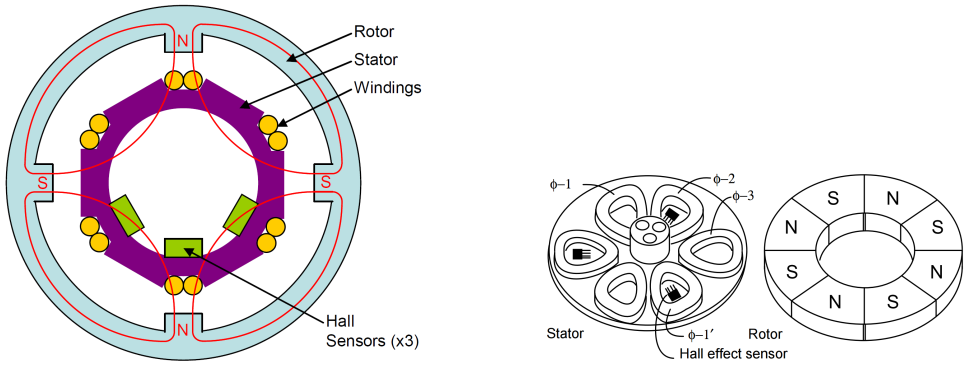

(a) Out-runner type motor designed for reaction wheels [21].

(b) Pancake type motor used in some reaction wheel designs [15].

Figure 2.3: Motor types used in reaction wheel designs.

Based on the choices made during the motor's design, a certain magnetic flux distribution is obtained in the air gap between the stator and the rotor. In an ideal brushless motor, this flux distribution is either sinusoidal or trapezoidal. However, real-world motors deviate from these two ideal shapes. This is caused both by the coil winding and placement process (e.g.: the coils have a non-/ferromagnetic core; the coils are wound using single-/multi-stranded wires or the coils are directly fabricated into a printed circuit board), as well as by the magnet distribution onto the rotor.

Once the overall design choices for the motor have been established, adequate rotor position sensors must be chosen in order to obtain reliable information. The two main options for rotor position sensors (that are also suited for space applications) are optical encoders, and Hall effect sensors. While it can provide a higher resolution position feedback, optical encoders are more cumbersome to integrate in the new, miniaturized reaction wheel designs.

On the other hand, Hall effect sensors have a straightforward implementation into the reaction wheels, since they rely on measuring the magnetic field generated by the permanent magnets in the wheel's rotor (as can be seen in Figure 2.3). The loss of resolution associated with Hall sensors can be compensated by increasing the amount of magnet pole pairs.

2.1.2. Reaction Wheel Operation

In a brushless motor, a magnetic field vector is produced by the current that flows through each one of the three stator coils. By summing these three magnetic field vectors, the stator magnetic field vector is obtained. In order to control the direction and magnitude of the stator's magnetic field vector the currents present in the stator coils are varied. Torque is, thus, produced through the attraction/repulsion between the stator magnetic field and the rotor magnetic field (see Figure 2.4).

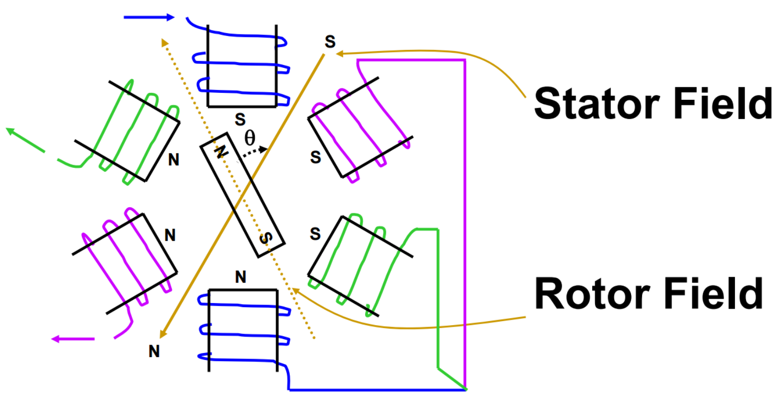

Figure 2.4: Brushless DC motor stator magnetic field vector and rotor magnetic field vector [2].

The stator magnetic field is made up of two components: one parallel, and one orthogonal to the rotor field. Out of these two components, the orthogonal (quadrature) component produces torque, while the parallel (direct) component produces compression forces that act on the motor bearings. Thus, in order to maximize the effectiveness of the reaction wheel, the direct field component must be minimized, while maximizing the quadrature component [1]. Moreover, in order to obtain the maximum torque output from the reaction wheel motor, at any point in its operation, the stator magnetic field must be orthogonal to the rotor magnetic field.

In order to apply the required currents on the reaction wheel's motor coils, a DC voltage is commutated by solid state drives, based on information obtained from the rotor position sensors. The two most utilized commutation methods for reaction wheels are six step commutation (due to its simplicity of implementation), and field oriented control (due to its ability to greatly reduce commutation torque ripple). These two methods are described in detail in [8].

2.2. Reaction Wheel Modelling

The HT-RW4xx reaction wheel series makes use of a three-phase, star-connected BLDCM. Three Hall sensors, placed around the stator, provide rotor position information, with a resolution of $60°$. Driving the wheel's motor is achieved by a voltage inverter that uses metal-oxide-semiconductor field-effect transistors (MOSFETs), presented in Figure 2.5.

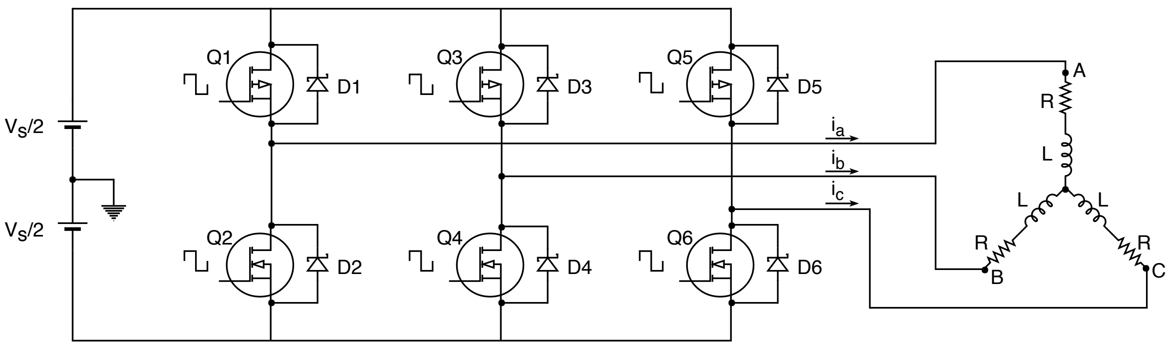

Figure 2.5: Reaction wheel motor drive scheme, using a voltage inverter.

In order to develop the simulation that is to be used to evaluate the performance of the state estimators developed in Chapter 4, a high degree of detail is required in addition to the base electrical and mechanical model. To this end, the three-phase electrical model, as well as the mechanical model of the reaction wheel are derived in Section 2.2.1. The Hall-based rotor position sensors, and their placement error is discussed in Section 2.2.2, followed by the Hall-sensor based angular velocity computation that is described in Section 2.2.3. The six-step commutation logic is described in Section 2.2.4. Finally, the voltage inverter model is discussed in Section 2.2.5.

2.2.1. Electrical and Mechanical Model

The equations defining the voltages across each of the three stator coils are given in (2.1).

$$\begin{bmatrix} v_{an} \\ v_{bn} \\ v_{cn} \end{bmatrix} = \begin{bmatrix} R_s & 0 & 0 \\ 0 & R_s & 0 \\ 0 & 0 & R_s \end{bmatrix} \cdot \begin{bmatrix} i_a \\ i_b \\ i_c \end{bmatrix} + \frac{d}{dt} \begin{bmatrix} \psi_a \\ \psi_b \\ \psi_c \end{bmatrix} \tag{2.1}$$

where $v_{an},\ v_{bn},\ v_{cn}$ represent the phase voltages, $i_a,\ i_b,\ i_c$ represent the phase currents, and R_s denotes the phase resistance. The rate of change of the magnetic flux in each stator winding is denoted by $\frac{d\psi_a}{dt},\ \frac{d\psi_b}{dt},\ \frac{d\psi_c}{dt}$.

The total magnetic flux linking each stator winding, $\psi_a,\ \psi_b,\ \psi_c$, is defined in (2.2).

$$\begin{bmatrix} \psi_a \\ \psi_b \\ \psi_c \end{bmatrix} = \begin{bmatrix} L_{aa} & L_{ab} & L_{ac} \\ L_{ba} & L_{bb} & L_{bc} \\ L_{ca} & L_{cb} & L_{cc} \end{bmatrix} \cdot \begin{bmatrix} i_a \\ i_b \\ i_c \end{bmatrix} + \begin{bmatrix} \psi_{am} \\ \psi_{bm} \\ \psi_{cm} \end{bmatrix} \tag{2.2}$$

where L_{aa}, L_{bb}, L_{cc} denote the self-inductances of each stator coils, L_{ab}, L_{ac}, L_{ba}, L_{bc}, etc. represent the mutual inductances of the stator coils, and ψ_{am}, ψ_{bm}, ψ_{cm} denote the permanent magnet fluxes that link the stator coils.

Knowing that the back-EMF represents the rate of change of flux over time, the relation presented in (2.3) can be computed.

$$\begin{bmatrix} e_a \\ e_b \\ e_c \end{bmatrix} = \frac{d}{dt} \begin{bmatrix} \psi_{am} \\ \psi_{bm} \\ \psi_{cm} \end{bmatrix} = k_e \cdot \omega_m \cdot \begin{bmatrix} f\left(\theta_e\right) \\ f\left(\theta_e - \frac{2\pi}{3}\right) \\ f\left(\theta_e - \frac{4\pi}{3}\right) \end{bmatrix} \tag{2.3}$$

where e_a, e_b, e_c represent the induced EMF (back-EMF) of each phase, N denotes the number of magnetic pole pairs, ω_m is the mechanical angular velocity, and ψ_m represents the magnetic flux linkage factor. Note that ψ_m determines both the motor's back-EMF constant, denoted by k_e, and the motor's torque constant, denoted by k_t.

Furthermore, $f\left(\theta_e\right)$ denotes the motor's magnetic flux distribution shape function (which gives the shape of the motor's back-EMF), with a maximum amplitude of ± 1, and is a function of the rotor's electrical angular position θ_e. This shape function is obtained by measuring the back-EMF of the motor, and it will be performed in Section 2.3.

Assuming that the there is no change in the rotor reluctance as a function of angle, and assuming that the three motor phases are symmetric, it follows that the self-inductances of the three phases are equal to each other. Furthermore, the mutual inductances between the phases are equal to one another. The relation in (2.4) can, thus, be written.

$$\begin{gathered} L_{aa} = L_{bb} = L_{cc} = L \\ L_{ab} = L_{ba} = L_{ac} = L_{ca} = L_{bc} = L_{cb} = M \end{gathered} \tag{2.4}$$

Furthermore, the stator currents are constrained to be balanced, hence, the relation given in (2.5) holds.

$$i_a + i_b + i_c = 0 \tag{2.5}$$

Having set these constraints, the voltage equations of the reaction wheel motor are re-formulated in (2.6).

$$\frac{d}{dt} \begin{bmatrix} i_a \\ i_b \\ i_c \end{bmatrix} = \begin{bmatrix} -\frac{R_s}{L_s} & 0 & 0 \\ 0 & -\frac{R_s}{L_s} & 0 \\ 0 & 0 & -\frac{R_s}{L_s} \end{bmatrix} \cdot \begin{bmatrix} i_a \\ i_b \\ i_c \end{bmatrix} + \begin{bmatrix} -\frac{1}{L_s} & 0 & 0 \\ 0 & -\frac{1}{L_s} & 0 \\ 0 & 0 & -\frac{1}{L_s} \end{bmatrix} \cdot \begin{bmatrix} e_a \\ e_b \\ e_c \end{bmatrix} + \begin{bmatrix} \frac{1}{L_s} & 0 & 0 \\ 0 & \frac{1}{L_s} & 0 \\ 0 & 0 & \frac{1}{L_s} \end{bmatrix} \cdot \begin{bmatrix} v_{an} \\ v_{bn} \\ v_{cn} \end{bmatrix} \tag{2.6}$$

where L_s represents the phase inductance, and is defined as $L_s = L - M$.

Having the dynamic equations for the electric part of the reaction wheel established, the mechanical equation of motion can be introduced in (2.7).

$$T_e = J \cdot \frac{d}{dt}\omega_m + T_f\left(\omega_m\right) + T_l\left(\omega_m\right) \tag{2.7}$$

where J represents the wheels mass moment of inertia, T_e denotes the electromagnetic torque generated by the motor, $T_f\left(\omega_m\right)$ is the non-linear reaction wheel friction torque (determined experimentally in Section 2.3, as a function of angular velocity), and $T_l\left(\omega_m\right)$ represents the load/disturbance torque acting on the reaction wheel (discussed and modelled in detail in Chapter 3).

The electromagnetic torque is defined in (2.8).

$$T_e = k_t \cdot \left[f\left(\theta_e\right) \cdot i_a + f\left(\theta_e - \frac{2\pi}{3}\right) \cdot i_b + f\left(\theta_e - \frac{4\pi}{3}\right) \cdot i_c\right] \tag{2.8}$$

As it can be observed, the electromagnetic torque is highly dependent on the phase currents, and on the magnetic flux distribution of the motor (shape of the back-EMF signals). It is, thus, necessary to drive the stator coils such that the phase currents align with the magnetic flux, resulting in the maximum torque output. Therefore, accurate rotor position information is vital for a high performance, highly efficient reaction wheel system.

The relation between the electrical angular position and the mechanical angular velocity is given in (2.9).

$$\frac{d}{dt}\theta_e = N \cdot \omega_m \tag{2.9}$$

By combining (2.6), (2.7), and (2.9), a state-space system of the form given in (2.10) is obtained.

$$\dot{x}(t) = A \cdot x(t) + B \cdot u(t) \tag{2.10}$$

with the state vector defined in (2.11).

$$x = \begin{bmatrix} i_a & i_b & i_c & \omega_m & \theta_e \end{bmatrix}^T \tag{2.11}$$

The system matrices are then described in (2.12).

$$A = \begin{bmatrix} -\frac{R_s}{L_s} & 0 & 0 & 0 & 0 \\ 0 & -\frac{R_s}{L_s} & 0 & 0 & 0 \\ 0 & 0 & -\frac{R_s}{L_s} & 0 & 0 \\ 0 & 0 & 0 & 0 & 0 \\ 0 & 0 & 0 & N & 0 \end{bmatrix} \qquad B = \begin{bmatrix} \frac{1}{L_s} & 0 & 0 & 0 \\ 0 & \frac{1}{L_s} & 0 & 0 \\ 0 & 0 & \frac{1}{L_s} & 0 \\ 0 & 0 & 0 & \frac{1}{J} \\ 0 & 0 & 0 & 0 \end{bmatrix} \tag{2.12}$$

Lastly, the input vector is defined by (2.13).

$$u = \begin{bmatrix} v_{an} - e_a \\ v_{bn} - e_b \\ v_{cn} - e_c \\ T_e - T_f - T_l \end{bmatrix} \tag{2.13}$$

As it can be observed, all non-linear components have been moved into the systems input vector. This has been done in order to allow for a more straightforward and faster reaction wheel simulation implementation.

2.2.2. Hall Sensor Modelling

Having defined the main electrical and mechanical equations of a reaction wheel system, attention must be given to the wheel's Hall sensors, which are critical in the correct and efficient commutation of the motor's phases. In the Hyperion Technologies reaction wheels, three Hall sensors, placed around the stator at $120°$ from one another, are used to obtain information about the rotor's electrical position.

Hall sensors function based on the Hall-effect theory, which states that when a magnetic field is passed through a conductor that is carrying electric current, the charge build-up at the ends of the conductor will produce a measurable voltage, proportional to the magnetic field's strength. The Hall-effect principle is presented in Figure 2.6.

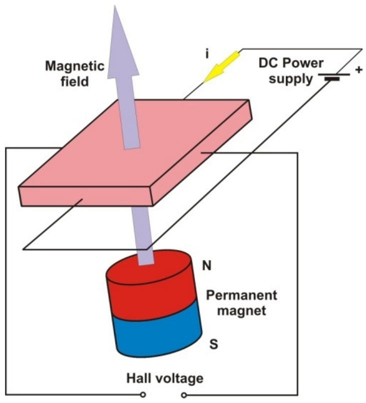

Figure 2.6: Hall-effect principle [11].

Each Hall sensor has internal signal conditioning circuitry which takes as input the voltage generated by the Hall element, removes its offset voltage, amplifies the signal, and passes it through a Schmitt trigger (i.e.: hysteresis comparator). This results into a binary (on/off) signal that is output by the sensor IC (integrated circuit). Combining the binary signals from all three sensors, a rotor electrical position feedback with a resolution of $60°$ is obtained.

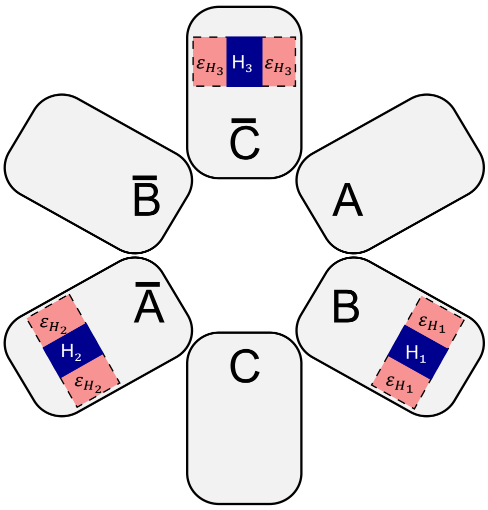

Figure 2.7: Hall sensor placement error in the reaction wheels stator.

As noted in Section 2.2.1, correct information on the rotor's position is crucial for maximum torque generation, and efficient wheel operation, thus, the placement of Hall sensors around the stator must be exact. Furthermore, the output of the Hall sensors must correspond precisely to the position they have been placed in. Unfortunately, this is not possible in practice, both due to manufacturing techniques that result in sensor misplacement (presented in Figure 2.7, with ε_{p_1}, ε_{p_2}, ε_{p_3} representing the placement error values for each Hall sensor), as well as due to the presence of the hysteresis band in the Hall sensors (depicted in Figure 2.8).

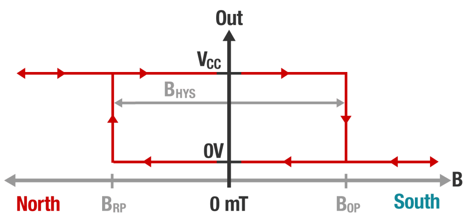

Figure 2.8: Hysteresis band in digital Hall-effect sensors[1].

Sensor placement errors due to manufacturing can be reduced through the use of higher accuracy production techniques, which, aided by the constant advancements in manufacturing technologies, eventually results in extremely low errors. However, besides the fact that these placement errors can never be fully eliminated, the use of high accuracy motor production technologies comes at a significant increase in production times and costs.

The business model of NewSpace companies, especially nanosatellite subsystems suppliers, relies on high volume sales of low-priced systems (achieved through optimization, for both time and cost, of the entire production cycle of the systems), as opposed to the classical space approach of highly expensive, one-off systems. It is, thus, not desirable to have exceedingly high manufacturing times and costs for one of the most important parts of the reaction wheel system.

The integrated hysteresis band within the Hall sensor ICs prevents the output of the sensor from extremely fast on-off transitions that would occur during the transition between two magnetic poles. Typically the hysteresis band has fixed values for its on and off thresholds, although, for some sensors it is possible to program these thresholds. However, completely eliminating the hysteresis band is not desirable, due to the very reason mentioned in the beginning of the paragraph. Thus, position information obtained from the Hall sensors always contains a bias both due to placement errors, and due to their hysteresis band.

Algorithm 1 Rotor position to Hall sensor output mapping

$\Theta_{ew} \leftarrow \theta_e \bmod 2\pi$
$H_1 \leftarrow 0$
$H_2 \leftarrow 0$
$H_3 \leftarrow 0$
if $\Theta_{ew} < \frac{5\pi}{3}$ and $\Theta_{ew} \geq \frac{2\pi}{3}$ **then**
    $H_1 \leftarrow 0$
else
    $H_1 \leftarrow 1$
end if
if $\Theta_{ew} \geq \frac{\pi}{3}$ and $\Theta_{ew} < \frac{4\pi}{3}$ **then**
    $H_2 \leftarrow 1$
else
    $H_2 \leftarrow 0$
end if
if $\Theta_{ew} \geq \pi$ and $\Theta_{ew} < 2\pi$ **then**
    $H_3 \leftarrow 1$
else
    $H_3 \leftarrow 0$
end if

[1]URL: www.ti.com/content/dam/ticom/images/products/ic/sensing-products/diagrams/latch-functionality-1920x1080-dm8791.png [retrieved July 2018]

In terms of modelling the binary output of the Hall sensors present on the Hyperion Technologies reaction wheels, the electrical rotor position, θ_e, obtained from the dynamic equations defined in Section 2.2.1, is fed into three separate look-up tables, giving the output specific to each of the three sensors. These look-up tables are obtained by directly mapping the electrical rotor position to the Hall sensor output, as described in Algorithm 1.

The rotor position can then be obtained from the combination of the three Hall sensor signals, as presented in Table 2.1.

Table 2.1: Position output of the combined three Hall sensors.

Position Interval	Hall Sensor Output H_1	H_2	H_3	Position Output
$0 - \frac{\pi}{3}$	1	0	0	0
$\frac{\pi}{3} - \frac{2\pi}{3}$	1	1	0	$\frac{\pi}{3}$
$\frac{2\pi}{3} - \pi$	0	1	0	$\frac{2\pi}{3}$
$\pi - \frac{4\pi}{3}$	0	1	1	π
$\frac{4\pi}{3} - \frac{5\pi}{3}$	0	0	1	$\frac{4\pi}{3}$
$\frac{5\pi}{3} - 2\pi$	1	0	1	$\frac{5\pi}{3}$

In order to model the measurement bias that is induced by the placement error and sensor hysteresis, the sensor position error values are added to the electrical position output of the simulated reaction wheel system. The biased position values are then fed into the Hall sensor look-up tables, as can be observed in Figure 2.9.

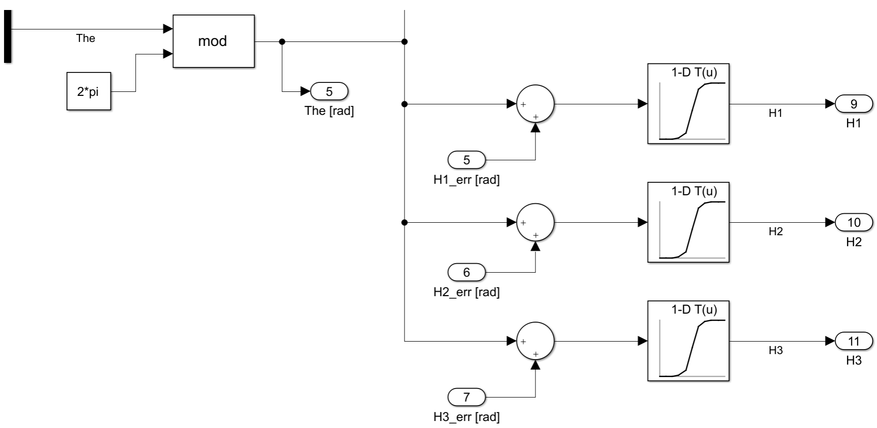

Figure 2.9: Hall sensor simulation, including the error due to sensor placement.

The overall sensor position error values, denoted by ε_{H_1}, ε_{H_2}, ε_{H_3} (defined in the simulation as *H1_err, H2_err, H3_err*) are defined in (2.14).

$$\begin{aligned} \varepsilon_{H_1} &= \varepsilon_{p_1} + \varepsilon_{hyst_1} \\ \varepsilon_{H_2} &= \varepsilon_{p_2} + \varepsilon_{hyst_2} \\ \varepsilon_{H_3} &= \varepsilon_{p_3} + \varepsilon_{hyst_3} \end{aligned} \tag{2.14}$$

As can be observed, position errors due to sensor placement (ε_{p_1}, ε_{p_2}, ε_{p_3}), and due to sensor hysteresis (ε_{hyst_1}, ε_{hyst_2}, ε_{hyst_3}) are contained in the overall sensor position error values. Characterisation of the sensor errors is performed in Section 2.3, where the Hall sensors' output is compared to the back-EMF of the motor, which is a highly position dependent signal, as can be observed from (2.3). The simulated output signals of the Hall sensors, and the position obtained from combining those signals, are presented in Figure 2.10.

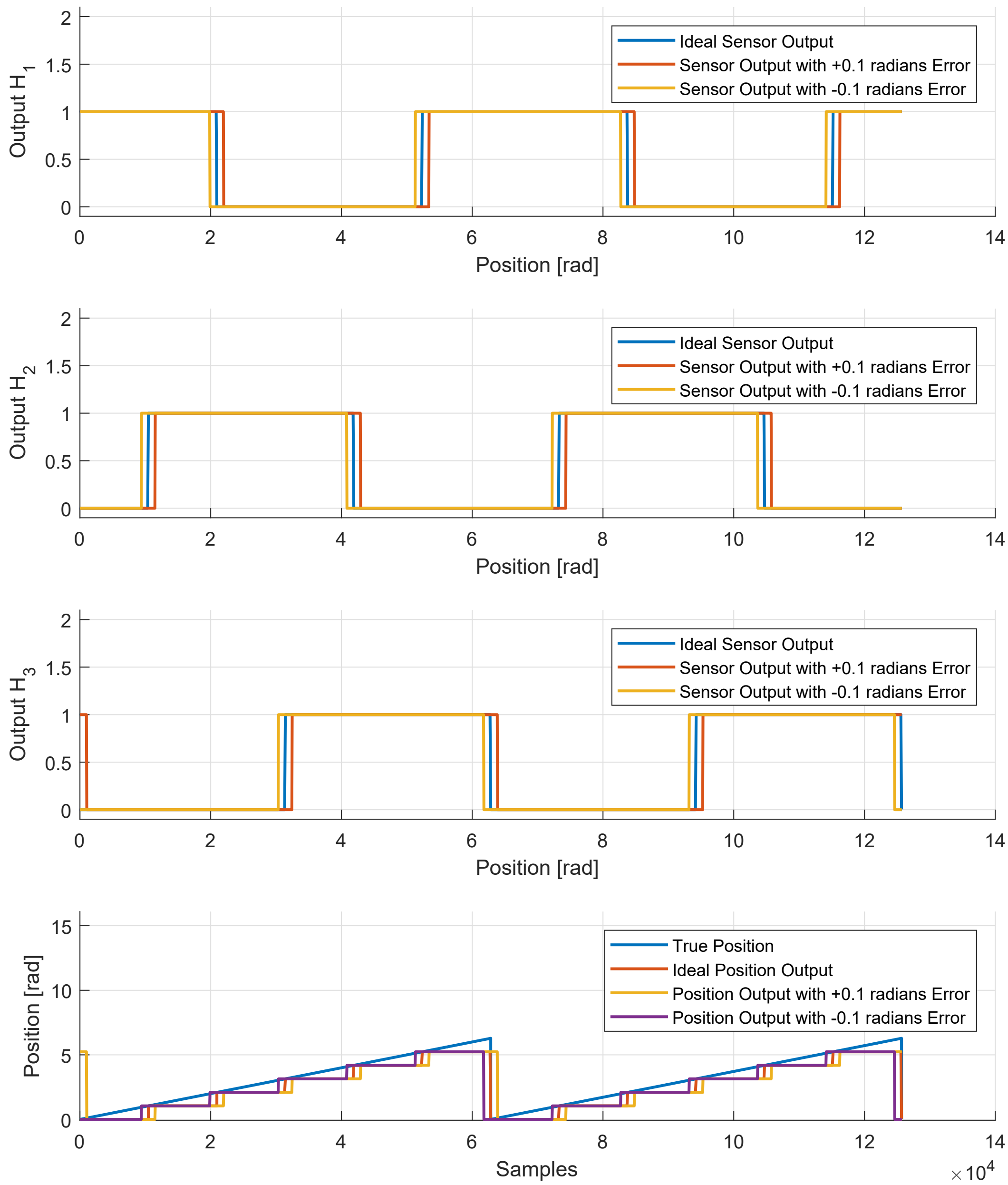

Figure 2.10: Hall sensor individual output signals (including measurement error), and rotor position measurement from the combined Hall sensor outputs.

2.2.3. Angular Velocity Computation

Angular velocity, together with rotor position, represents a crucial piece of information in a properly functioning reaction wheel assembly. Due to the high level of integration and miniaturization that the Hyperion Technologies reaction wheels are subjected to, angular velocity measurement options are rather limited.

Dedicated rotation speed sensors, especially high accuracy ones, are high both in mass and in volume, therefore they are immediately discarded from the solution space. The remaining options are to make use of the already installed Hall sensors, or to employ back-EMF amplitude measurements (since it is directly proportional to the reaction wheel's angular velocity). However, the back-EMF measurements are close to unusable at low rotation speeds, due to the very low signal-to-noise ratio (SNR).

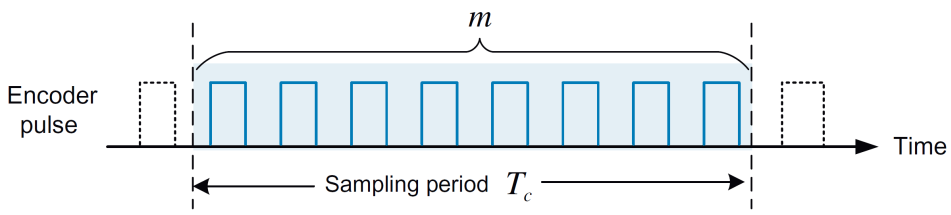

Figure 2.11: The M method for angular velocity computation [13].

Computation of reaction wheel rotation speed using Hall sensors is performed using one of the methods used for rotary encoders. These methods are the *M method*, the *T method*, and the *M/T method*, all three being described in detail in [13]. The M, and the M/T methods make use of a fixed sampling interval, during which the number of pulses is counted, with the addition that, for the M/T method, the sampling interval is extended up to the beginning of a new pulse (as can be seen in Figure 2.11, and in Figure 2.12). The M, and M/T methods require a high number of pulses per rotation in order to be able to use a sampling interval that is high enough to be used for rotation speed control. Therefore, due to the low pulse count of wheel's stator Hall sensors, the M, and M/T methods cannot be used for angular velocity computation.

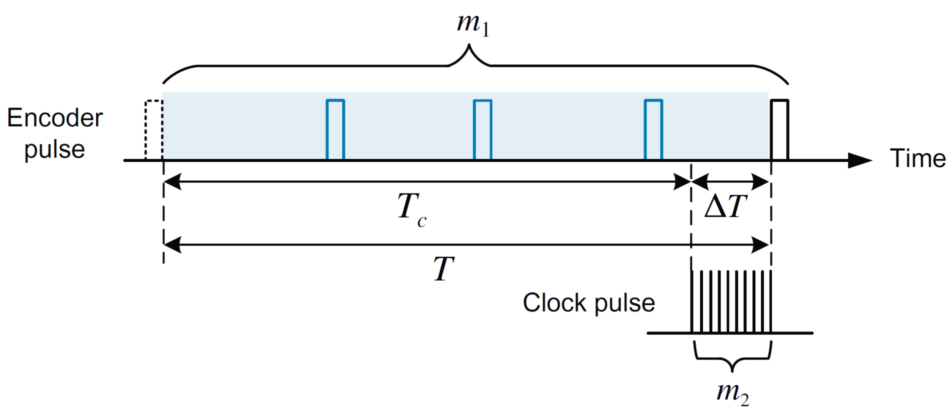

Figure 2.12: The M/T method for angular velocity computation [13].

The T method relies on measuring the time interval, T_c, between two consecutive pulses, as shown in Figure 2.13. By measuring the time between both rising edges, and falling edges of the Hall sensor signals, the equivalent pulses per revolution, PPR, is given in (2.15).

$$PPR = 2 \cdot n_H \cdot N \tag{2.15}$$

where n_H represents the number of Hall sensors that are mounted on the wheel's stator, and N represents the number of magnetic pole pairs. The angular velocity can, thus, be computed using the relation given in (2.16).

$$\omega_m = \frac{2\pi}{PPR \cdot T_c} \tag{2.16}$$

Although the T method allows for an accurate measurement of the reaction wheel's speed at steady-state, it suffers from three issues (same issues apply to the M, and M/T methods). First of all, due to the approach used for the speed measurement, the T method has a changing sampling time. While this does not cause major control issues at high rotation speeds, it becomes detrimental to the performance of the speed controller when the wheel operates at low rotation speeds [13]. Due to the fact that the sampling frequency can reach values below $20\,Hz$, the ability of the control algorithm to handle various torque disturbances (e.g.: random changes in friction) is significantly diminished.

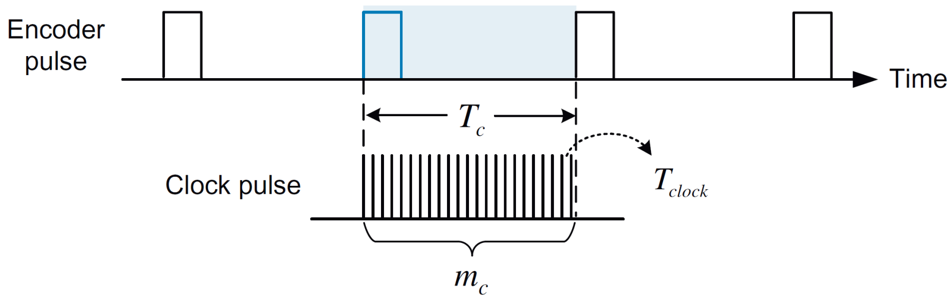

Figure 2.13: The T method for angular velocity computation [13].

The second issue faced by the angular velocity computation is quantization. Since the speed computation of the T method is, in its essence, position differentiation, the obtained angular velocity has a rather coarse resolution that is directly related to the coarseness of the Hall sensor pulses. Quantization is also influenced by the sampling period used. However, by comparison, this does not play a significant role in the rotation speed computation, since today's processors are able to easily measure the time between two events with below nanosecond accuracy.

The third, and final issue is that the T speed computation method can only output a discrete average speed over the sample period, instead of the true instantaneous rotation speed [13]. As can be observed from Figure 2.14, the T method is able to provide a good angular velocity measurement when the wheel is in steady-state. However, during the wheel's acceleration, the computed angular velocity is erroneous (also shown in Figure 2.14).

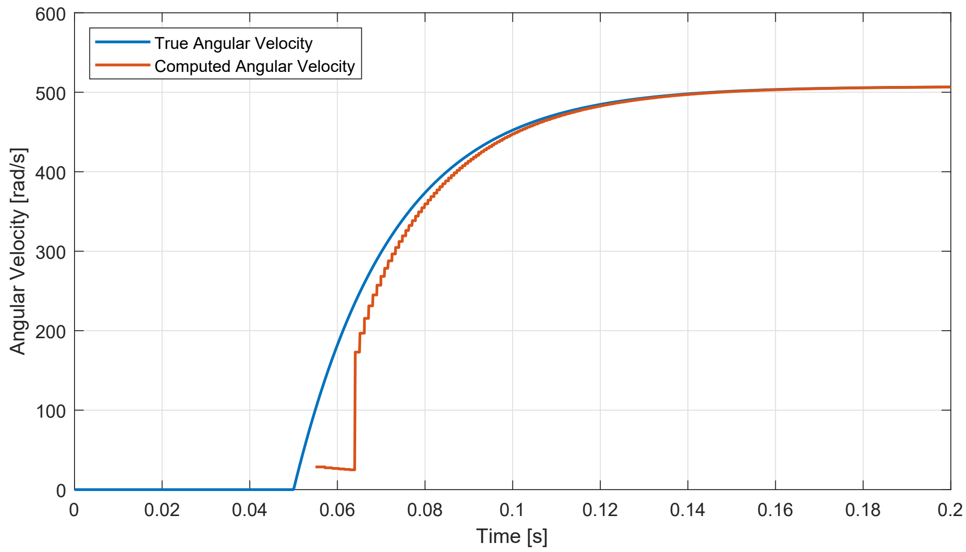

Figure 2.14: Angular velocity computed using the T method, compared to the true rotation speed.

This error is due to the lack of information between two sensor transitions. Thus, when the angular velocity of the reaction wheel changes quickly (i.e. the angular acceleration is of a high value), the measurement error also increases. When the angular acceleration decreases in value, becoming almost zero (i.e. the wheel is in steady-sate), the measurement error also becomes zero, since the angular velocity does not change in between two Hall sensor transitions.

2.2.4. Commutation Logic

The Hyperion Technologies reaction wheels currently make use of the six step commutation (also known as trapezoidal commutation) technique. Six step commutation is the simplest brushless motor driving technique. The commutation method consists in energising two motor stator coils at a time, each coil being active for $120°$ intervals. The two coils to be energised are selected based on feedback from the wheel's Hall sensors. Although simple to implement, the six step commutation method results in increased torque ripple, especially in motors that have a non-trapezoidal magnetic flux distribution.

The commutation is performed with the help of the voltage source inverter (VSI – presented in Figure 2.5). The switching sequence, phase current polarity, and Hall sensor signals, characteristic to each commutation interval, are presented in Table 2.2. The commutation patterns for both clockwise (CW) and counter-clockwise (CCW) reaction wheel spinning directions are presented in Table 2.2 as well.

Table 2.2: Reaction wheel commutation logic for clockwise and counter-clockwise rotation directions.

Commutation Interval	Hall Sensor Output			Clockwise Rotation					Counter-clockwise Rotation				
				Active Switch		Phase Current			Active Switch		Phase Current		
	H_1	H_2	H_3			i_a	i_b	i_c			i_a	i_b	i_c
$0 - \frac{\pi}{3}$	1	0	0	Q_1	Q_4	+	-	off	Q_3	Q_2	-	+	off
$\frac{\pi}{3} - \frac{2\pi}{3}$	1	1	0	Q_1	Q_6	+	off	-	Q_5	Q_2	-	off	+
$\frac{2\pi}{3} - \pi$	0	1	0	Q_3	Q_6	off	+	-	Q_5	Q_4	off	-	+
$\pi - \frac{4\pi}{3}$	0	1	1	Q_3	Q_2	-	+	off	Q_1	Q_4	+	-	off
$\frac{4\pi}{3} - \frac{5\pi}{3}$	0	0	1	Q_5	Q_2	-	off	+	Q_1	Q_6	+	off	-
$\frac{5\pi}{3} - 2\pi$	1	0	1	Q_5	Q_4	off	-	+	Q_3	Q_6	off	+	-

2.2.5. Voltage Inverter Model

The voltage source inverter takes a DC voltage, usually supplied by a battery, and turns it into an AC voltage. The inverter output voltage can have various shapes (e.g.: square wave, sinusoidal wave, modified sine wave, etc.) and frequencies. Inverters are able, theoretically, to have any number of output phases. Evidently, limitations related to the practicality of a high phase count inverter provide an upper boundary to the number of phases that are implemented in real-world inverters.

The VSI used to drive the Hyperion Technologies reaction wheels has a three-phase output, with varying frequency and amplitude. An on-board processor controls both the output frequency and the output amplitude based on the feedback obtained from the reaction wheel motor.

As presented in Section 2.2.4, the six-step commutation technique is used to drive the reaction wheels. This commutation logic is implemented on the on-board processor. The processor controls the output voltages of each phase by activating or de-activating the low- and high-side MOSFETs of the inverter. The MOSFETs are activated based on the rotor position. The exact position interval, in which each inverter FET is active, is presented in Table 2.2.

It can be observed that the load connected to the inverter's output phases is not a simple resistive load, it is in fact an inductive load. Based on Faraday's law of induction, when the current through an inductor changes, the inductor induces a voltage in order to keep the current flowing through. If there is no path for the current to flow through, except through air, the induced voltage becomes extremely high, which can easily damage the inverter switches. In order to prevent this from happening, fly-back diodes (also known as free-wheeling diodes) are added to the VSI circuit.

When modelling the reaction wheel voltage inverter, this free-wheeling diode needs to be accounted for. The modelling method for the VSI mainly consists in determining the voltage that is output to each phase of the reaction wheel motor. Performing a quick analysis on a single output phase of the voltage inverter, four different states can be determined for the phase.

The first state has both the low- and high-side switches in a conducting state. This results in a short circuit, which will destroy the switches, and, thus, it is undesirable. The second state consists of an open low-side switch, and a conducting high-side switch, resulting in a positive phase voltage, v_P, being output, as can be seen in Figure 2.15(a). The third state is complementary to the second one, in the sense that the low-side is conducting, and the high-side is open, resulting in a negative output phase voltage, as shown in Figure 2.15(b).

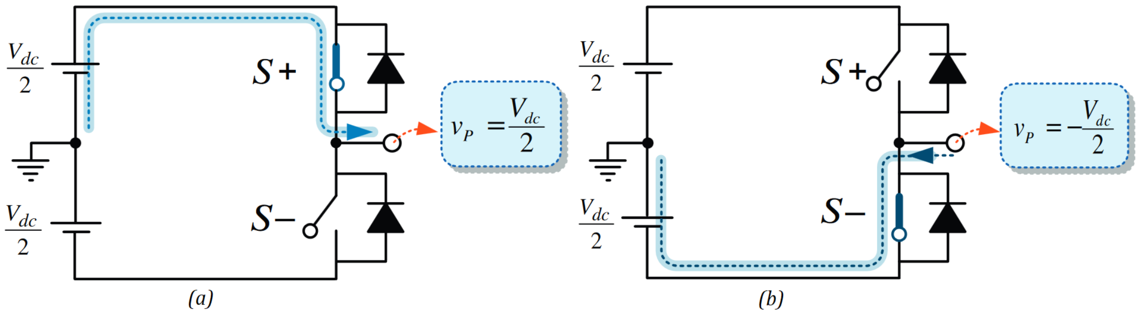

Figure 2.15: Inverter circuit configurations determined by: $(a)$the high-side switch being closed, $(b)$the low-side switch being closed [12].

Lastly, the fourth state consists of both low- and high-side switches being open. However, since there is current flowing through the motor's stator coil, a voltage at the inverter's output phase will be produced. This voltage depends on the direction in which the current is flowing, as can be observed in Figure 2.16.

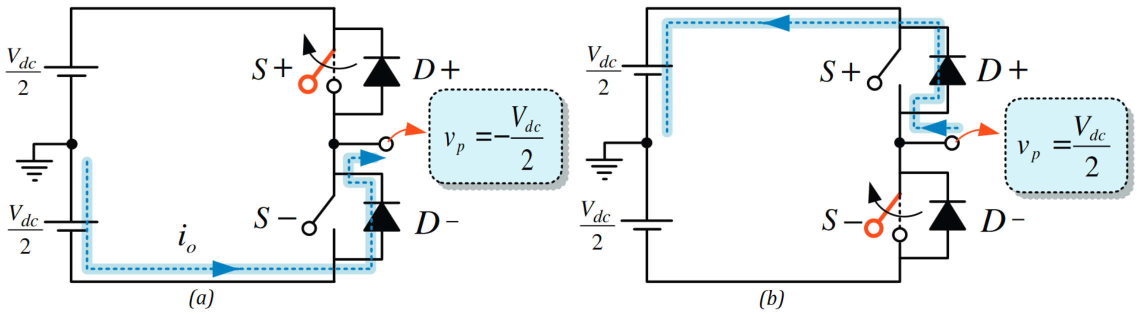

Figure 2.16: Inverter circuit configurations determined by: $(a)$the high-side switch opening, $(b)$the low-side switch opening [12].

Having laid the foundation for the method used in modelling the free-wheeling diode effect, attention can be given to the electrical circuit formed by the full three-phase voltage inverter and the motor stator coils, and its model. It is worth noting that in modelling the reaction wheel VSI, the MOSFETs are assumed to be ideal (zero On-resistance), instantaneous switches. Furthermore, the voltages that the inverter model outputs already contain the back-EMF, thus, the outputs can be directly fed into the electrical model of the reaction wheel.

The instantaneous switch assumption is made due to the fact that the turn-on and -off times of the MOSFETs are extremely fast compared to the rest of the wheel's electrical dynamics. The zero On-resistance assumption is justified by the fact that the resistance of the switch is included directly into the phase resistance value.

When using the six-step commutation technique, two different circuit topologies can be distinguished. The first circuit topology, shown in Figure 2.17, presents the equivalent electric circuit for the case when the high-side switch has been active in the previous commutation interval, and it is turned off in the current interval. Note that all three phases have the same complex impedance, Z, which is composed of the real part, representing the phase resistance R_s, and the imaginary part, which represents the phase inductance L_s.

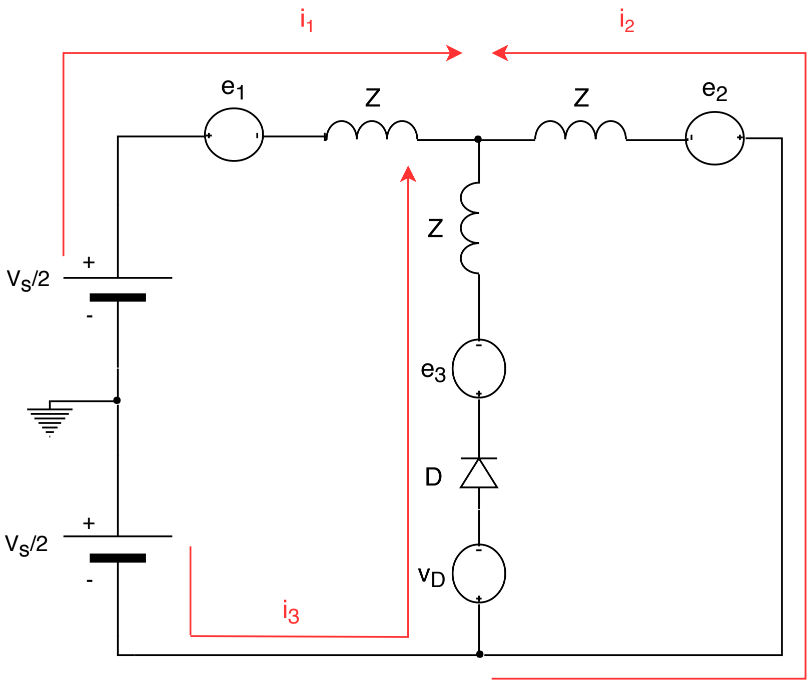

Figure 2.17: Voltage inverter and motor coils equivalent electric circuit topology one. Created when the high-side switch from the previous switching interval is turned off.

The equations describing the phase currents i_1, i_2, i_3 of the first electrical circuit topology are given in (2.17).

$$
\begin{aligned}
i_1 &= \left(\frac{V_{DC}}{2} - e_1\right) \cdot Z \\
i_2 &= \left(-\frac{V_{DC}}{2} - e_2\right) \cdot Z \\
i_3 &= \left(-\frac{V_{DC}}{2} - e_3 - v_D\right) \cdot Z
\end{aligned}
\tag{2.17}
$$

The phase voltages v_1, v_2, v_3, are easily deduced from (2.17), and are given in (2.18).

$$
\begin{aligned}
v_1 &= \frac{V_{DC}}{2} - e_1 \\
v_2 &= -\frac{V_{DC}}{2} - e_2 \\
v_3 &= -\frac{V_{DC}}{2} - e_3 - v_D
\end{aligned}
\tag{2.18}
$$

with e_1, e_2, e_3 representing the back-EMF signals of each phase, V_{DC} represents the DC supply voltage, and v_D denotes the diode voltage.

It is clear that the final value of the v_3 phase voltage depends on the diode voltage, which varies based on the state of the diode. If the diode is conducting, the phase current i_3 is non-zero, thus, the diode is not creating any voltage to oppose the flow of current through it, hence, $v_D = 0$. When the phase current i_3 is zero, the diode voltage v_D becomes non-zero, such that it stops any current from flowing through. Therefore, the value of the phase voltage v_3 is given in (2.19).

$$v_3 = \begin{cases} 0, & \text{if } i_3 = 0 \\ -\frac{V_{DC}}{2} - e_3, & \text{if } i_3 \neq 0 \end{cases} \tag{2.19}$$

The second circuit topology is presented in Figure 2.18. It shows the equivalent electric circuit for the case when the low-side switch has been active in the previous commutation interval, and it is turned off in the current interval.

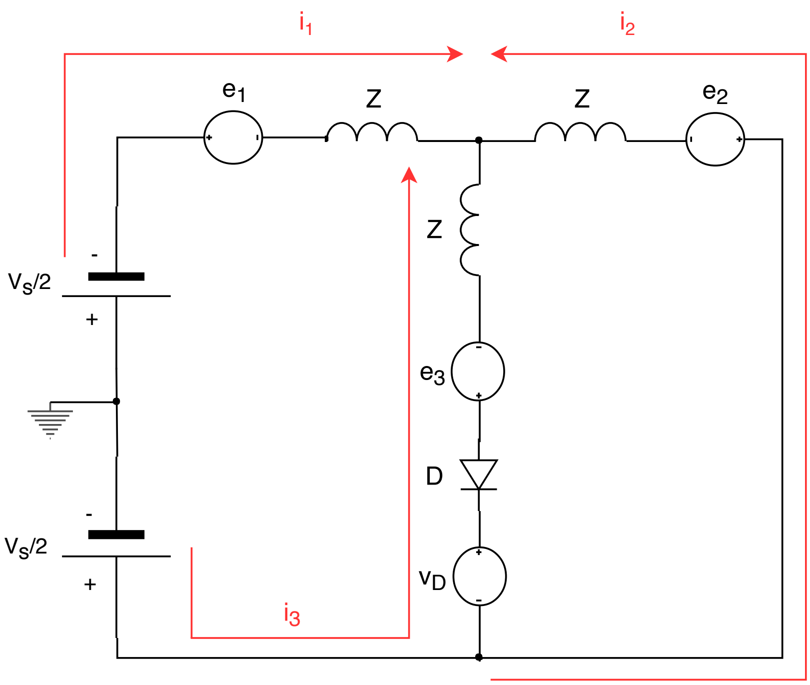

Figure 2.18: Voltage inverter and motor coils equivalent electric circuit topology two. Created when the low-side switch from the previous switching interval is turned off.

The equations describing the phase currents i_1, i_2, i_3 of the second electrical circuit topology are given in (2.20).

$$\begin{aligned} i_1 &= \left(-\frac{V_{DC}}{2} - e_1\right) \cdot Z \\ i_2 &= \left(\frac{V_{DC}}{2} - e_2\right) \cdot Z \\ i_3 &= \left(\frac{V_{DC}}{2} - e_3 + v_D\right) \cdot Z \end{aligned} \tag{2.20}$$

The phase voltages v_1, v_2, v_3, are then given in (2.21).

$$\begin{aligned} v_1 &= -\frac{V_{DC}}{2} - e_1 \\ v_2 &= \frac{V_{DC}}{2} - e_2 \\ v_3 &= \frac{V_{DC}}{2} - e_3 + v_D \end{aligned} \quad (2.21)$$

Following the same reasoning given for the first circuit topology, the value of the phase voltage v_3 is given in (2.22).

$$v_3 = \begin{cases} 0, & \text{if } i_3 = 0 \\ \frac{V_{DC}}{2} - e_3, & \text{if } i_3 \neq 0 \end{cases} \quad (2.22)$$

In order to correctly assign the phase voltage values, the inverter and stator coils circuit has been drawn for every commutation interval of the clockwise rotation direction of the reaction wheel. The circuits are presented in Figure 2.19. For the counter-clockwise rotation direction, the equivalent circuit configurations are not drawn, however, it is a straightforward task.

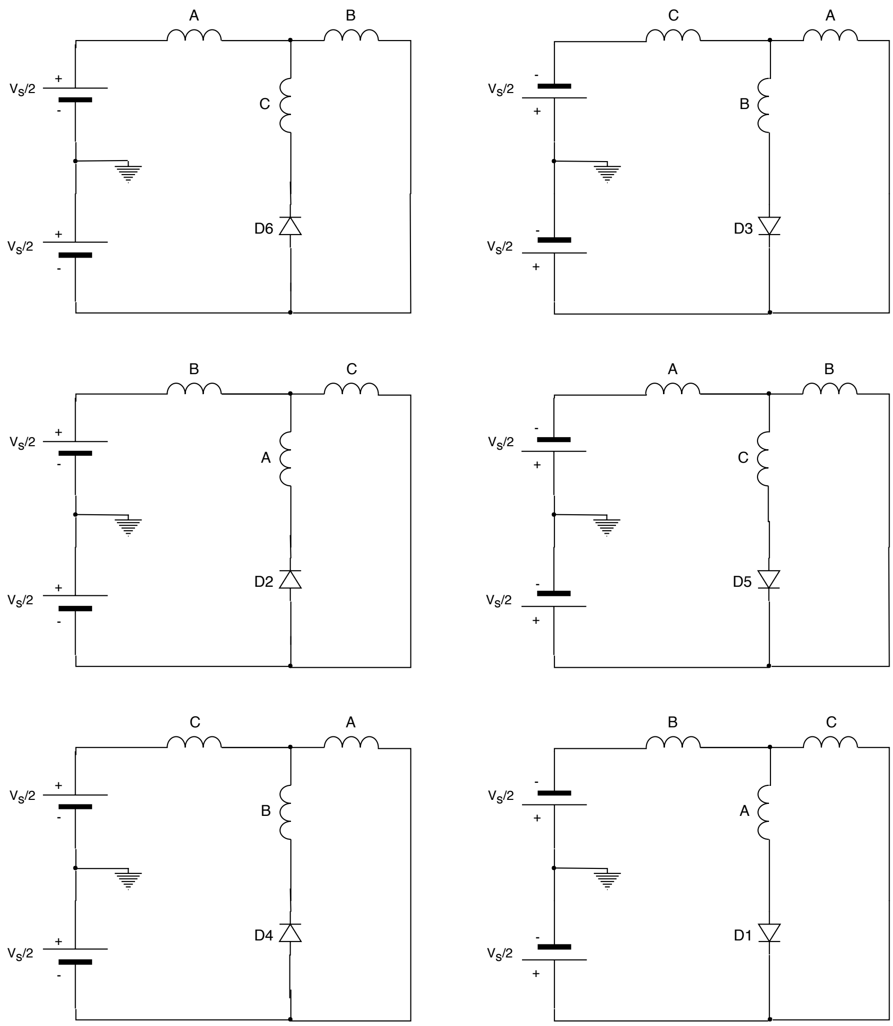

Figure 2.19: Voltage and motor coils equivalent electric circuit configuration for each commutation interval.

The voltage inverter output voltages, both for clockwise and counter-clockwise wheel spinning directions, are given in Table 2.3.

Table 2.3: Voltage inverter output voltages for clockwise and counter-clockwise rotation.

Commutation Interval	Fly-back Current	Clockwise Rotation			Counter-clockwise Rotation		
		Phase Voltage			Phase Voltage		
		v_a	v_b	v_c	v_a	v_b	v_c
$0-\frac{\pi}{3}$	$i_c = 0$	$\frac{V_{DC}}{2}-e_a$	$-\frac{V_{DC}}{2}-e_b$	0	$-\frac{V_{DC}}{2}-e_a$	$\frac{V_{DC}}{2}-e_b$	0
	$i_c \neq 0$	$\frac{V_{DC}}{2}-e_a$	$-\frac{V_{DC}}{2}-e_b$	$-\frac{V_{DC}}{2}-e_c$	$-\frac{V_{DC}}{2}-e_a$	$\frac{V_{DC}}{2}-e_b$	$\frac{V_{DC}}{2}-e_c$
$\frac{\pi}{3}-\frac{2\pi}{3}$	$i_b = 0$	$\frac{V_{DC}}{2}-e_a$	0	$-\frac{V_{DC}}{2}-e_c$	$-\frac{V_{DC}}{2}-e_a$	0	$\frac{V_{DC}}{2}-e_c$
	$i_b \neq 0$	$\frac{V_{DC}}{2}-e_a$	$\frac{V_{DC}}{2}-e_b$	$-\frac{V_{DC}}{2}-e_c$	$-\frac{V_{DC}}{2}-e_a$	$-\frac{V_{DC}}{2}-e_b$	$\frac{V_{DC}}{2}-e_c$
$\frac{2\pi}{3}-\pi$	$i_a = 0$	0	$\frac{V_{DC}}{2}-e_b$	$-\frac{V_{DC}}{2}-e_c$	0	$-\frac{V_{DC}}{2}-e_b$	$\frac{V_{DC}}{2}-e_c$
	$i_a \neq 0$	$-\frac{V_{DC}}{2}-e_a$	$\frac{V_{DC}}{2}-e_b$	$-\frac{V_{DC}}{2}-e_c$	$\frac{V_{DC}}{2}-e_a$	$-\frac{V_{DC}}{2}-e_b$	$\frac{V_{DC}}{2}-e_c$
$\pi-\frac{4\pi}{3}$	$i_c = 0$	$-\frac{V_{DC}}{2}-e_a$	$\frac{V_{DC}}{2}-e_b$	0	$\frac{V_{DC}}{2}-e_a$	$-\frac{V_{DC}}{2}-e_b$	0
	$i_c \neq 0$	$-\frac{V_{DC}}{2}-e_a$	$\frac{V_{DC}}{2}-e_b$	$\frac{V_{DC}}{2}-e_c$	$\frac{V_{DC}}{2}-e_a$	$-\frac{V_{DC}}{2}-e_b$	$-\frac{V_{DC}}{2}-e_c$
$\frac{4\pi}{3}-\frac{5\pi}{3}$	$i_b = 0$	$-\frac{V_{DC}}{2}-e_a$	0	$\frac{V_{DC}}{2}-e_c$	$\frac{V_{DC}}{2}-e_a$	0	$-\frac{V_{DC}}{2}-e_c$
	$i_b \neq 0$	$-\frac{V_{DC}}{2}-e_a$	$-\frac{V_{DC}}{2}-e_b$	$\frac{V_{DC}}{2}-e_c$	$\frac{V_{DC}}{2}-e_a$	$\frac{V_{DC}}{2}-e_b$	$-\frac{V_{DC}}{2}-e_c$
$\frac{5\pi}{3}-2\pi$	$i_a = 0$	0	$-\frac{V_{DC}}{2}-e_b$	$\frac{V_{DC}}{2}-e_c$	0	$\frac{V_{DC}}{2}-e_b$	$-\frac{V_{DC}}{2}-e_c$
	$i_a \neq 0$	$\frac{V_{DC}}{2}-e_a$	$-\frac{V_{DC}}{2}-e_b$	$\frac{V_{DC}}{2}-e_c$	$-\frac{V_{DC}}{2}-e_a$	$\frac{V_{DC}}{2}-e_b$	$-\frac{V_{DC}}{2}-e_c$

2.3. Reaction Wheel Characterisation

In order for the simulation to give an adequate representation of the real-world reaction wheel system, a few experiments are required to obtain higher accuracy values for the parameters used in modelling the reaction wheel. Performing these characterisation experiments allows for an accurate simulation, making it possible to properly evaluate the state and disturbance estimation algorithms that are developed in Chapter 4.

Characterisation of the reaction wheel is limited to bearing friction torque, motor back-EMF shape, motor torque and back-EMF constants, and Hall sensor placement error. The phase inductance and resistance values will be taken from the motor datasheet, as they do not suffer any modification during assembly of the reaction wheel. A more involved characterisation of reaction wheel disturbances due to thermal effects, micro-vibration, etc. is performed in Chapter 3. This is done in order to keep the more fundamental part of the reaction wheel simulation separated from the highly detailed disturbance modelling and characterisation that is detailed in Chapter 3.

Performing experiments to determine the bearing friction torque, Hall sensor placement errors, and motor torque and back-EMF constants, is necessary due to variations throughout production.

During the reaction wheel manufacturing process, the distance between the wheel's stator and rotor varies, which results in torque and back-EMF constants that are of different values from the ones given in the motor's datasheet. Furthermore, the bearing friction torque of the reaction wheel must be determined experimentally, since it has a rather non-linear behaviour due to the use of space-rated lubricants. Lastly, the placement error value of the wheel's Hall sensors varies for each wheel.

2.3.1. Bearing Friction Torque

The experiment required to determine the bearing torque friction of the Hyperion Technologies reaction wheels consists of an un-powered coast-down of the wheel from its maximum rotation speed. This results in an angular velocity coasting curve, from which the wheel friction curve can be computed. Since this experiment is aimed at obtaining the nominal wheel friction curve, multiple experiment runs are required for the same reaction wheel. The results are presented in Figure 2.20.

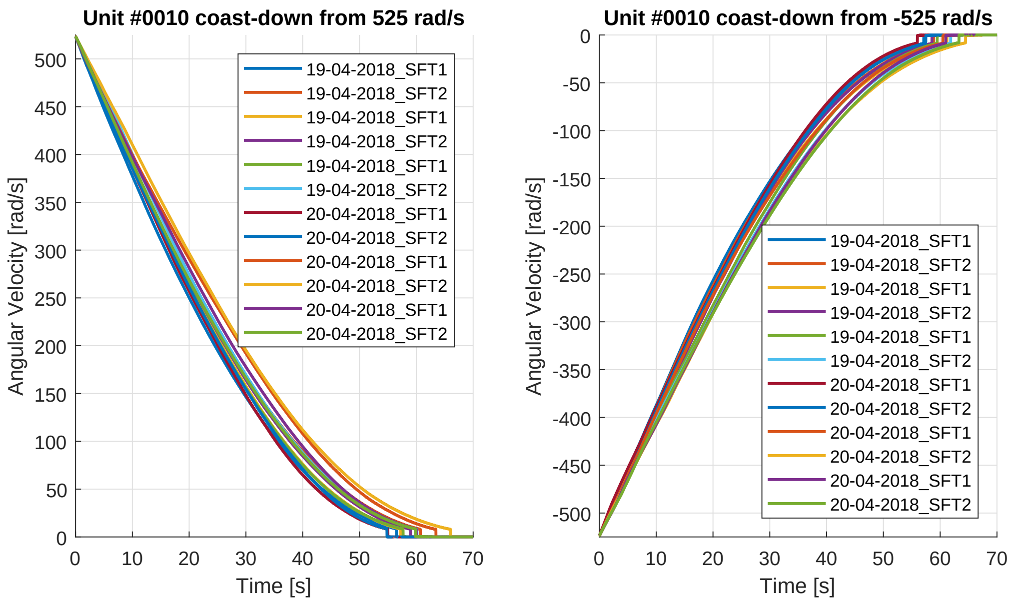

Figure 2.20: Reaction wheel angular velocity coast-down curves.

As it can be observed, a spread of approximately 10 seconds is present between the wheel coast-down times. Since these coasting times are approximately evenly spread around 60 seconds, the coast-down curve closest to the middle point is selected for the computation of the nominal wheel friction torque. The computed friction curve is presented in Figure 2.21, and it is incorporated into the reaction wheel simulation via a look-up table.

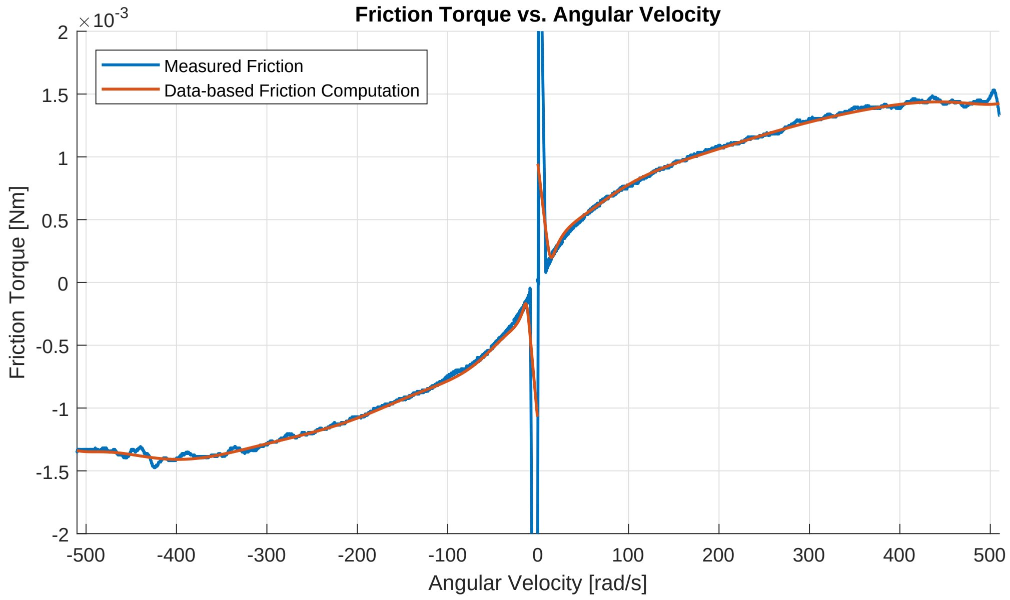

Figure 2.21: Reaction wheel friction torque curve.

It is necessary to note that the friction torque varies from wheel to wheel, thus, it needs to be determined for each wheel individually. This is due to variations in the bearing lubricant fill volume, bearing balls' contact angle and radial play, etc. These variations, and their root-cause, are thoroughly discussed in Chapter 3.

2.3.2. Magnetic Flux Distribution

In order to characterise the magnetic flux distribution (i.e. shape of the back-EMF) of the reaction wheel motor, a straightforward experiment is performed: the reaction wheel is spun-up to a constant angular velocity, using an external actuator. Once the wheel is at a constant velocity, the back-EMF of the stator phases is measured. Since the reaction wheel has symmetric stator coil windings, only one back-EMF signal is necessary to determine the wheel's magnetic flux distribution.

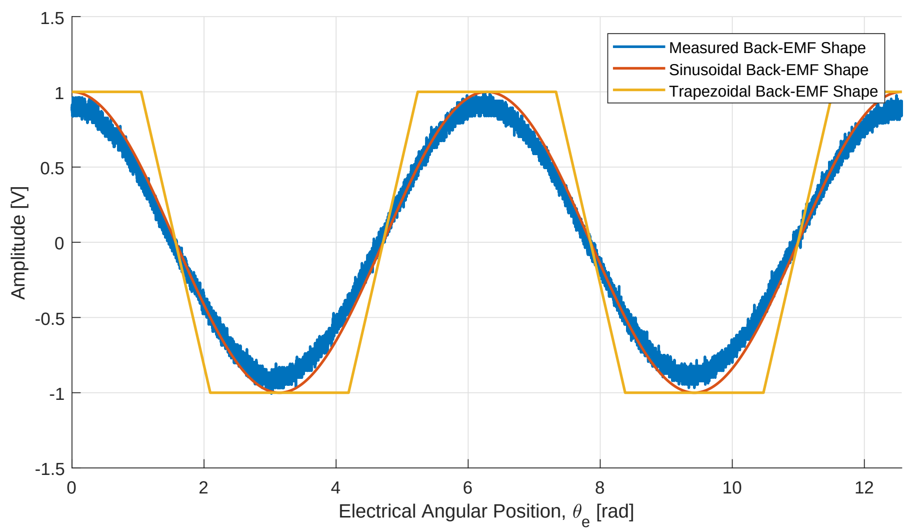

Figure 2.22: Reaction wheel measured back-EMF curve, showing the wheel's magnetic flux distribution.

Based on the measured back-EMF signal presented in Figure 2.22, it can be concluded that the flux distribution is in fact sinusoidal.

2.3.3. Motor Torque and Back-EMF Constants

The motor torque, k_t and back-EMF, k_e, constants are determined by the same motor property, i.e. the magnetic flux linkage. The relation between the two constants is given in (2.23).

$$k_t = \frac{\sqrt{3}}{2} \cdot k_e \tag{2.23}$$

The experimental data required to obtain the value of these two parameters is, in fact, the back-EMF signal. By spinning the reaction wheel at a constant angular velocity, the amplitude of the measured back-EMF signal can then be used to compute the k_t and k_e values.

With an amplitude value of $0.2031\ V$ (as observed from Figure 2.22), at an angular velocity of approximately $34.103\ rad/s$, the value of the two parameters is given in (2.24).

$$\begin{aligned} k_t &= 5.15761 \cdot 10^{-3}\ \frac{Nm}{A} \\ k_e &= 5.95548 \cdot 10^{-3}\ \frac{V}{rad/s} \end{aligned} \tag{2.24}$$

2.3.4. Hall Sensor Output Error

Determining the Hall sensor output error, which is equivalent to their placement error, requires comparing the measured sensor outputs with a signal that is directly dependent on the rotor position, and which is not subject to measurement errors. The motor's back-EMF is the best signal for this.

The reaction wheel is, once again, spun-up to a constant angular velocity. Each Hall sensor output signal is then measured, together with the back-EMF signals. The measurement results are presented in Figures 2.23, 2.24, and 2.25.

Based on the results from Figures 2.23, 2.24, and 2.25, the Hall sensor output error can be determined by comparing the moment of the rising and falling edge of the sensor signal to the back-EMF signal. Thus, the Hall sensor placement error is given in (2.25).

$$\begin{aligned} \varepsilon_{H_1} &= +0.032\ rad \\ \varepsilon_{H_2} &= -0.045\ rad \\ \varepsilon_{H_3} &= +0.026\ rad \end{aligned} \tag{2.25}$$

2.4. Conclusion

Throughout this chapter, a dynamic model of the HT-RW4xx reaction wheel system has been developed. The model includes a detailed representation of the Hall-sensor based rotor angular position, and angular velocity measurements. Additionally, the reaction wheel friction torque, magnetic flux distribution, torque and back-EMF constants, and Hall-sensor output error are characterised. An adequate model is thus obtained that allows for a representative simulation of the HT-RW4xx reaction wheels.

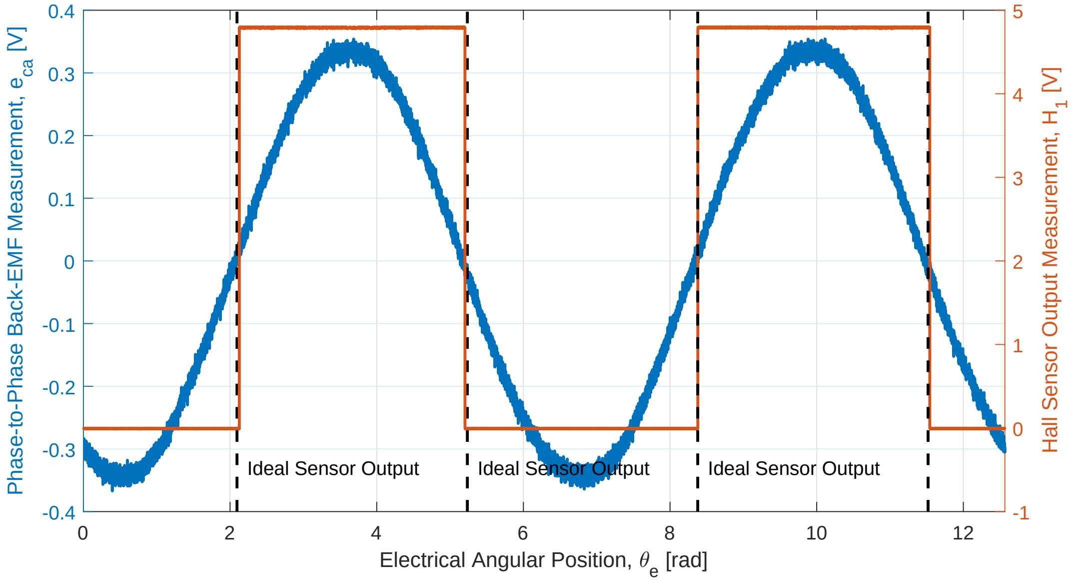

Figure 2.23: Comparison between Hall sensor H_1 output, and motor phase-to-phase back-EMF signal e_{ca}.

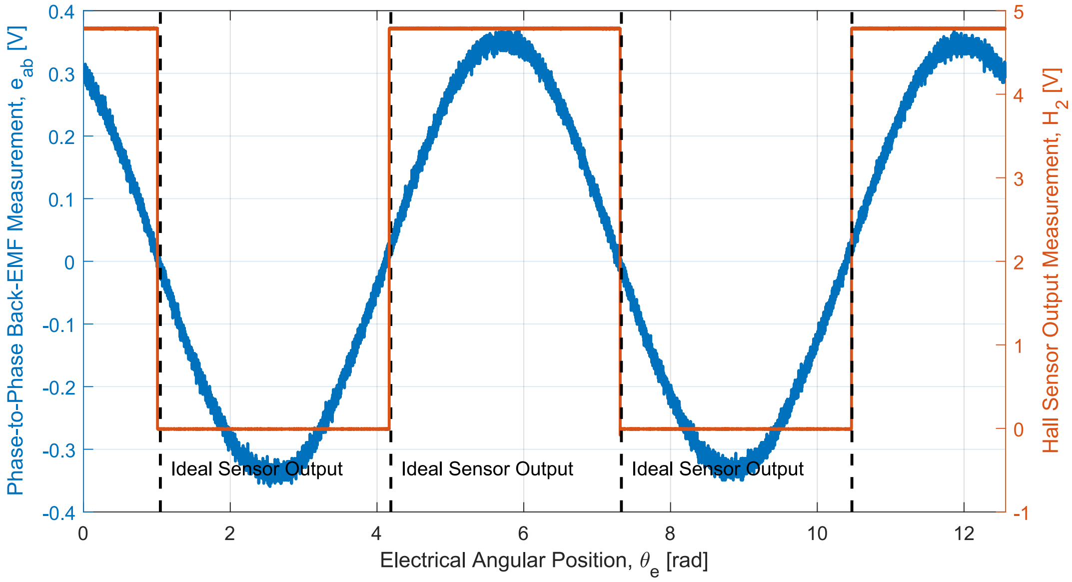

Figure 2.24: Comparison between Hall sensor H_2 output, and motor phase-to-phase back-EMF signal e_{ab}.

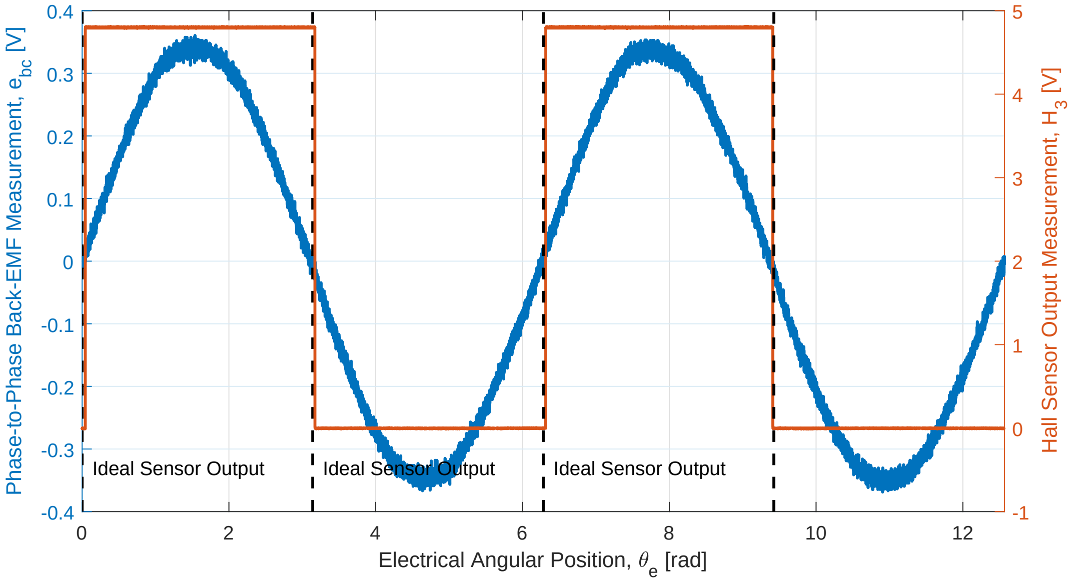

Figure 2.25: Comparison between Hall sensor H_3 output, and motor phase-to-phase back-EMF signal e_{bc}.

3
Reaction Wheel Disturbances

In this chapter, reaction wheel disturbances will be analysed in depth. These disturbances, despite having different root causes, they each affect, to a certain degree, the output and friction torque of the wheel. This directly impacts the speed control accuracy of the reaction wheel. It is, thus, logical that the analysis performed in this chapter will be focused on the impact of various disturbance sources on the torque output of the wheel. Furthermore, disturbance models will be proposed, evaluated, and integrated into the reaction wheel simulation developed in Chapter 2.

It is well known that disturbances in the reaction wheel induce a deviation from the wheel's nominal behaviour, such as changes in the power consumption, variation in the wheel output torque, and even loss of speed control accuracy. The causes for these disturbances are numerous and highly varied. However, the main ones are: bearing lubricant roughness and viscosity, bearing geometry, bearing cage instabilities, environmental temperature variation, rotor imbalance, exposure to high/launch vibration levels. Furthermore, there is an inherent variation in the performance of every reaction wheel, resulting from manufacturing tolerances. This variation can also be treated as a disturbance, a constant one, to be more precise.

In order to characterise the magnitude, as well as the impact of these disturbances on the wheel's performance, an in depth test campaign has been performed on a number of reaction wheel units. This test campaign consists of numerous functional tests, thermal cycling tests, micro-vibration measurements, and shaker tests.

3.1. Thermal Effects

Reaction wheel systems, like all other satellite subsystems, are designed to operate within a certain temperature range. However, the behaviour of the wheels does, in fact, change as a result of thermal variation. This is due to multiple reasons, the main ones being: changes in bearing lubricant viscosity, thermal expansion and contraction of parts, variation in the inverter On-resistance, variation in motor coil resistance.

The property affected most by thermal variation is the reaction wheel's friction. This is evident, seeing that variation in both lubricant viscosity, as well as in the mechanical fits between bearings, rotor, and axle direct affect the friction curve of the wheel.

The reaction wheel bearings have a highly accurate fit (in the order of a few micrometers) with the rotor, and with the axle. With varying environmental temperature, the wheel parts will expand/contract, resulting in changes in the fits between the bearings, rotor, and axle. This, in turn, leads to a change in the contact angle and stress between the bearing raceway and the bearing balls, thus, leading to variations in the friction curve.

In order to ensure that the reaction wheel units are able to survive the vacuum of space, special space-rated grease is used to lubricate the wheel bearings. As with any fluid, the kinematic viscosity of the bearing lubricant varies with temperature, having a higher viscosity at low temperatures, and a lower viscosity at high temperatures. The lubricant viscosity variation due to temperature is presented in Figure 3.1.

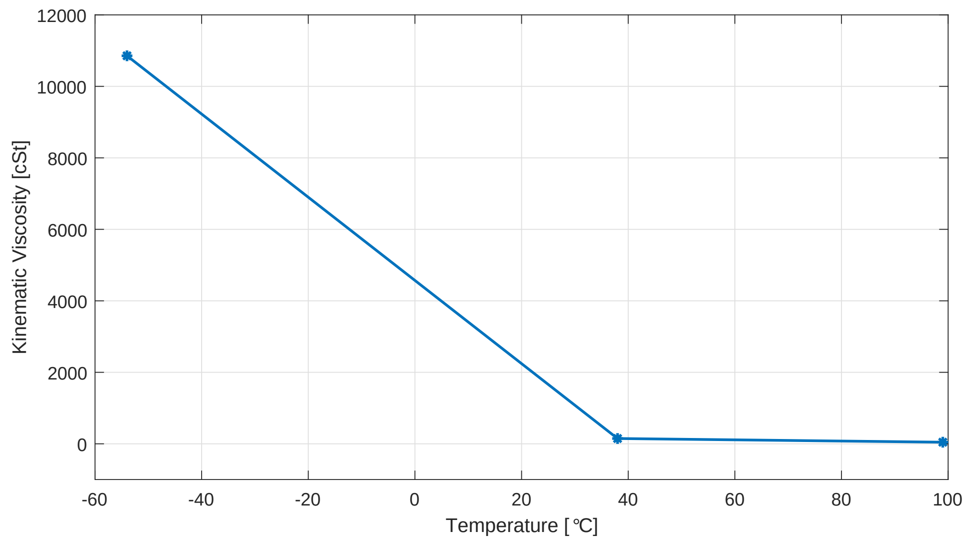

Figure 3.1: Bearing lubricant viscosity variation over temperature. Based on information provided by the lubricant datasheet.

It must be noted that the behaviour of grease lubricated bearings is much less understood than the behaviour of bearings using an oil lubricant. Following the churning process, where the grease is pushed to the sides of the bearing raceway, the contact surfaces of grease lubricated bearings are fed by the oil that is bleeding from the grease present on the sides [9]. Thus, the elasto-hydrodynamic (EHD) layer thickness is maintained by this oil. When the wheel is operating at high speeds, or in low temperature conditions (hence, high lubricant viscosity), the oil bleeding from the grease does not have enough time to replenish the bearing raceway, resulting in the reduction of the EHD layer thickness. This is known as the *kinematic starvation* effect, and it results in the friction levelling off, or even decreasing.

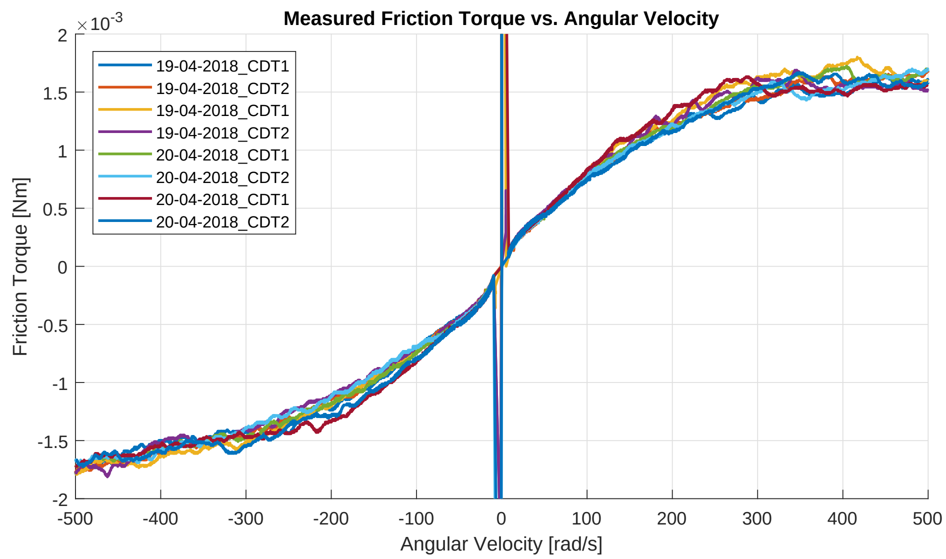

Figure 3.2: Reaction wheel measured friction torque curves at $+40°C$.

A series of eight full thermal cycles have been performed on the reaction wheel units, in order to evaluate the friction variation over temperature. One thermal cycle consists of wheel coast-down tests from its maximum angular velocity, in both directions of rotation, performed at $-20°C$ and $+40°C$. The measured friction curves from these experiments are presented in Figure 3.2, and in Figure 3.3.

As it can be observed, from both figures, the reaction wheel friction behaviour changes between low and high operating temperatures. At the environmental temperature of $+40°C$ (Figure 3.2), the bearing friction displays the behaviour specific to operation with a full lubricant film for more than 90% of the wheel's angular velocity range, while a slight lubricant starvation effect becomes observable close to the edge of the speed range. At $-20°C$ (Figure 3.3), the bearing friction displays a prominent kinematic starvation effect due to the increased viscosity of the lubricant.

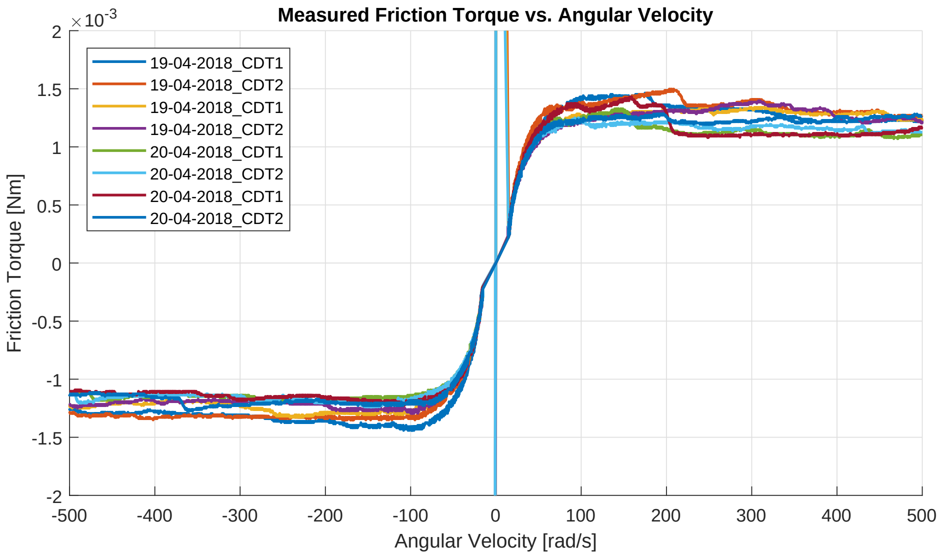

Figure 3.3: Reaction wheel measured friction torque curves at $-20°C$.

Another property affected by environmental temperature variation is the total resistance of the motor coil, and the inverter MOSFETs. The combined resistance variation (based on manufacturer datasheet information) over temperature is presented in Figure 3.4.

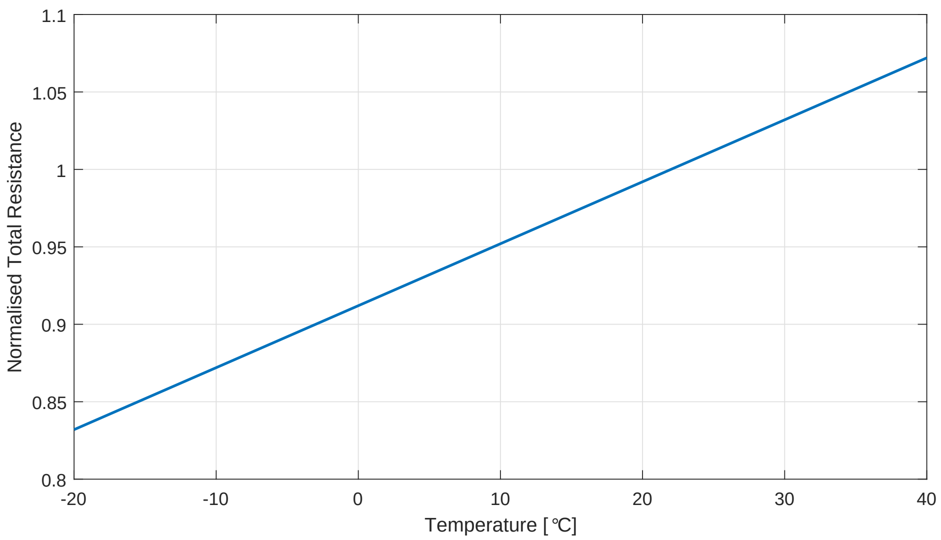

Figure 3.4: Combined motor coil and inverter MOSFET resistance variation over temperature.

Throughout the performed thermal cycles, the reaction wheel power consumption during its acceleration to maximum rotation speed is measured. The results are presented in Figure 3.5, from which it can be observed that a difference of over 16% is present between the power consumption at $-20°C$, and power consumption at $+40°C$, confirming the fact that a change in resistance occurs.

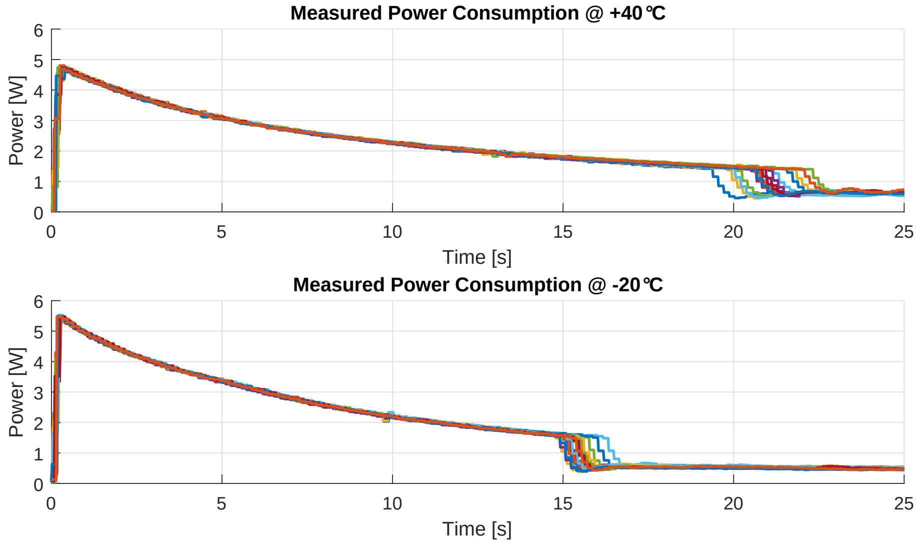

Figure 3.5: Reaction wheel power consumption when accelerating from stand-still to $525\ rad/s$, at $+40°C$ and $-20°C$.

3.2. Bearing Friction Disturbances

Disturbances related to bearing friction manifest themselves as spikes in the wheel's friction, as plateau-like variation in the friction torque, and, lastly, in the form of overall friction curve variation between units.

3.2.1. Bearing Friction Spread

Spread in the reaction wheel friction torque appears in two distinct situations. Firstly, friction varies between runs of the same reaction wheel unit. This variation is due to the run-in effects of the bearings used in each reaction wheel unit, such as warm-up and re-distribution of the bearing lubricant. From the previously presented figures (namely Figure 3.2, and Figure 3.3), a clear variation between each test run can be observed.

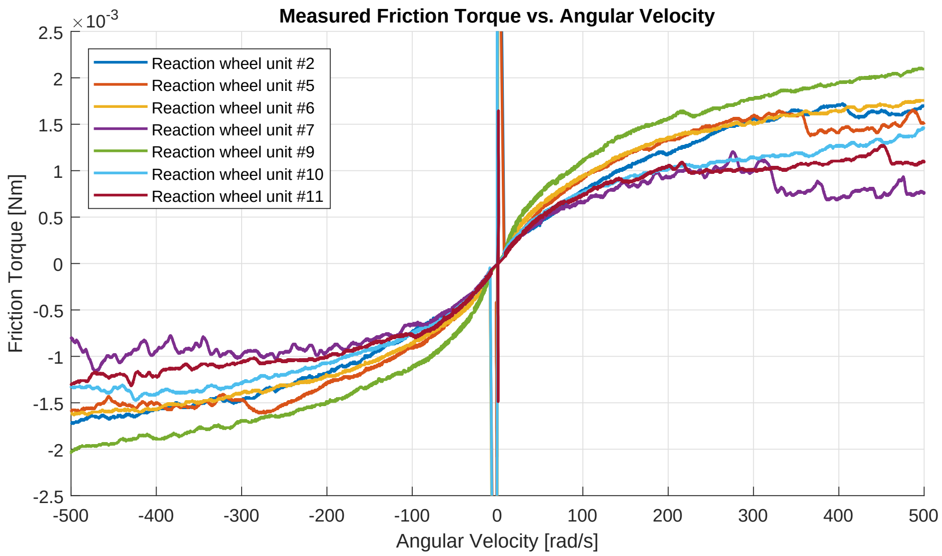

Figure 3.6: Comparison of the friction torque curves of different reaction wheel units.

Secondly, friction variation between each reaction wheel is easily observed by simply comparing the friction measurements of each unit. The comparison is presented in Figure 3.6, from which it can be observed that even a variation of 65% is possible from one wheel to another. This variation in friction has a myriad of possible causes: ball-raceway contact angle, ball-cage interaction, bearing-rotor fit (the tighter the interference fit, the less space the bearing balls have to move), large spread in bearing radial play, lubricant quantity. The causes previously enumerated require highly specialised tribological equipment to characterise, and, thus, have not been further investigated.

3.2.2. Bearing Friction Spikes and Plateaus

Spikes and plateau-like disturbances in the bearing friction curve are characterised by a rather sudden change in the friction, followed by the as sudden disappearance of the disturbance. While the spike disturbances are very brief in their duration, the plateau-like friction disturbances last much longer than the spikes. Both disturbance types are presented in Figure 3.7.

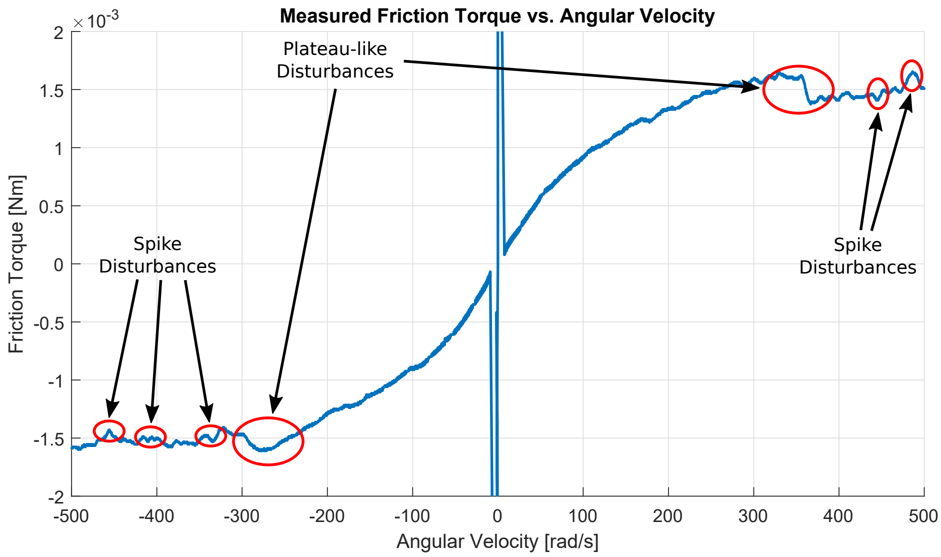

Figure 3.7: Spike and plateau-like disturbances occurring in reaction wheel friction curve.

The possible sources these disturbance phenomena are related to raceway smoothness, lubricant movement inside the bearing, particles in the lubricant, bearing cage instabilities [17], bearing-axle fit (if the sliding fit is too tight, the inner ring of the bearing can stick to the axle for brief moments, which causes a change in the ball-raceway contact angle), changes in the bearing pre-load, etc.

3.3. Micro-vibration Disturbances

Every reaction wheel has an inherent micro-vibration signature, which affects the nominal behaviour of the wheel. The sources of these micro-vibration disturbances can be divided into three categories: rotating mass imbalance, motor noise, and bearing disturbances. Furthermore, these disturbances interact with the wheel's structural dynamics, which determines their behaviour and impact on the reaction wheel unit.

3.3.1. Rotor Imbalance Disturbances

Rotor imbalance is the most significant disturbance source in a reaction wheel. It is characterised by two different errors in the rotor's symmetry with respect to its axis of rotation. These errors are known as static and dynamic imbalance.

Static imbalance is caused by the offset of the rotor's centre of gravity from the rotation axis. This is represented by a small mass, m, at a radius, r, as shown in Figure 3.8. The rotating radial force, that results from the imbalance, appears as a sinusoid, from a fixed reference frame, having a frequency equal to the wheel's mechanical angular velocity, ω_m. It, thus, has order $k_{si} = 1$. The amplitude of the force is given by the following equation:

$$F_i = m \cdot r \cdot \omega_m^2 \tag{3.1}$$

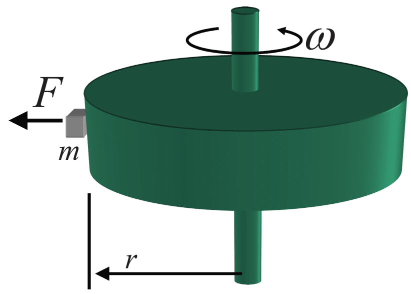

Figure 3.8: Schematic representation of rotor static imbalance[5].

Dynamic imbalance is caused by the misalignment between the rotor's principal inertia and its spin axis. This is represented by two masses of equal value, placed at $180°$ from each other, as shown in Figure 3.9. The resulting torque also appears as a sinusoid having a frequency equal to the wheel's angular velocity, thus, order $k_{di} = 1$. The amplitude of the imbalance torque is given by:

$$T_i = m \cdot r \cdot d \cdot \omega_m^2 \tag{3.2}$$

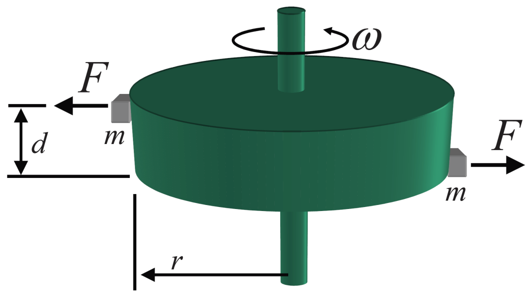

Figure 3.9: Schematic representation of rotor dynamic imbalance[5].

3.3.2. Motor Torque Disturbances

The two sources for reaction wheel motor torque disturbances are commutation ripple, and cogging. Commutation torque ripple is a result of the commutation method employed in driving the wheel, and the shape of the motor's back-EMF (magnetic flux distribution). Since it is not a pure sinusoidal occurrence, the commutation torque ripple contains extra higher order harmonics. The order of the commutation torque ripple base harmonic is given in (3.3).

$$k_{cr} = 2 \cdot n_P \cdot N \tag{3.3}$$

where n_P represents the number of motor phases, and N is the number of magnetic pole pairs in the rotor. In the case of the HT-RW4xx reaction wheels, this order is $k_{cr} = 12$.

Cogging torque is normally present in motors that have an iron core stator, caused by the change in reluctance of the iron stator under a rotating magnetic field. The order of cogging torque disturbances is given in the following equation:

$$k_{ct} = 2 \cdot n_T \cdot N \tag{3.4}$$

where n_T is the number of teeth in the stator.

Since the Hyperion Technologies reaction wheels have a zero-cogging motor design, cogging torque disturbances are completely eliminated from the reaction wheels.

3.3.3. Ball Bearing Disturbances

Disturbance generated by ball bearings are inevitable due to the imperfect nature of manufacturing, which results in imperfections in the bearing balls, and on the inner and outer raceways. Bearing cage disturbances are created due to a certain degree of cage imbalance, or in the ball complement [10]. Furthermore, bearing misalignment will result in a disturbance, of order $k_{bma} = 2$, being created. This is due to the fact that the bearing ball track becomes oval when an angular misalignment occurs [5].

Models for bearing disturbances are presented in both [5], and [10]. These models depend on a few bearing geometry parameters, namely: ball diameter, d_b; bearing pitch diameter, d_p; ball number, N_b; bearing contact angle, α; diameter ratio, $\delta = d_b/d_p$; and $\gamma = \delta \cdot \cos(\alpha)$. The main bearing disturbances of the HT-RW4xx reaction wheels, together with their order values are presented Table 3.1. Evidently, these disturbances contain higher order harmonics, as well as upper and lower side-bands, as presented in [10].

Table 3.1: Main bearing disturbance orders of the HT-RW4xx reaction wheels, based on formulas presented in [10].

Disturbance Name	Order Formula	Order Value
Bearing Misalignment (BMA)	–	$k_{bma} = 2$
Fundamental Train Frequency Inner Race (FTFI)	$\frac{1}{2}(1-\gamma)$	$k_{ftfi} = 0.3927$
Fundamental Train Frequency Outer Race (FTFO)	$\frac{1}{2}(1+\gamma)$	$k_{ftfo} = 0.6073$
Ball Pass Frequency Inner Race (BPFI)	$\frac{N_b}{2}(1+\gamma)$	$k_{bpfi} = 4.8586$
Ball Pass Frequency Outer Race (BPFO)	$\frac{N_b}{2}(1-\gamma)$	$k_{bpfo} = 3.1414$
Ball Spin Frequency (BSF)	$\frac{1}{2\delta}\left(1-\gamma^2\right)$	$k_{bsf} = 2.1463$
Double Ball Spin Frequency (DBSF)	$\frac{1}{\delta}\left(1-\gamma^2\right)$	$k_{dbsf} = 4.2927$

While the amplitude of the disturbance created by static and dynamic imbalances scales with the square of the angular velocity, the amplitude of the ball bearing disturbances, although not known for certain [10], will be assumed to vary linearly with the angular velocity. Thus, the amplitude of the disturbance torque is given by (3.5).

$$T_d = k_d \cdot \omega_m \tag{3.5}$$

where k_d is a scaling coefficient specific to a generic disturbance d. To obtain the torque amplitude of each disturbance type, the corresponding scaling coefficient is simply plugged into the equation.

The scaling coefficient, as well as the accuracy of the disturbance order estimates will be determined in Section 3.3.5.

3.3.4. Structural Dynamics

The structure of reaction wheels has an important role in the production of disturbances, due to the fact that any structural dynamic modes have a major effect on the disturbances' amplitude.

Reaction wheels have three dominant structural modes, namely the axial translation mode, the radial translation mode, and the radial rocking mode, presented in Figure 3.10. These modes are usually modelled using a single degree of freedom mass-spring in the wheel's axial direction, and a two degree of freedom mass-spring system in the wheel's radial direction, as shown in Figure 3.10.

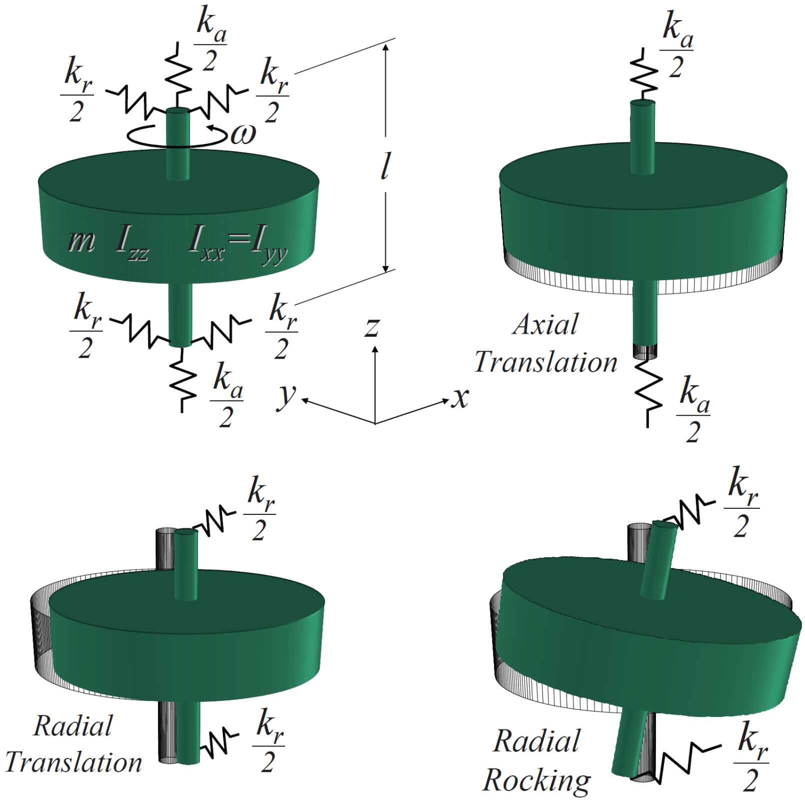

Figure 3.10: Schematic representation of reaction wheel structural modes[5].

The axial translation mode frequency is given by [5]:

$$f_a = \sqrt{\frac{k_a}{m}} \tag{3.6}$$

The radial translation mode frequency is given by:

$$f_r = \sqrt{\frac{k_r}{m}} \tag{3.7}$$

The radial rocking mode frequency is given by:

$$f_o = \sqrt{\frac{k_r \cdot l^2}{4 \cdot I_{xx}}} \tag{3.8}$$

The presence, as well as the resonant frequency of these structural modes are easily identifiable when performing micro-vibration signature characterisation of the reaction wheels.

3.3.5. Micro-vibration Signature Characterisation

In order to evaluate the amplitude of the micro-vibration disturbances, as well as the accuracy of the bearing disturbance order estimations, the reaction wheels' micro-vibration signature must be characterised.

First, the Campbell diagram containing all the modelled disturbances is created, shown in Figure 3.11. Although the diagram does not contain information on the amplitude of the disturbances, it aids in predicting the wheel rotation speed, as well as the frequency at which each of these disturbances will occur.

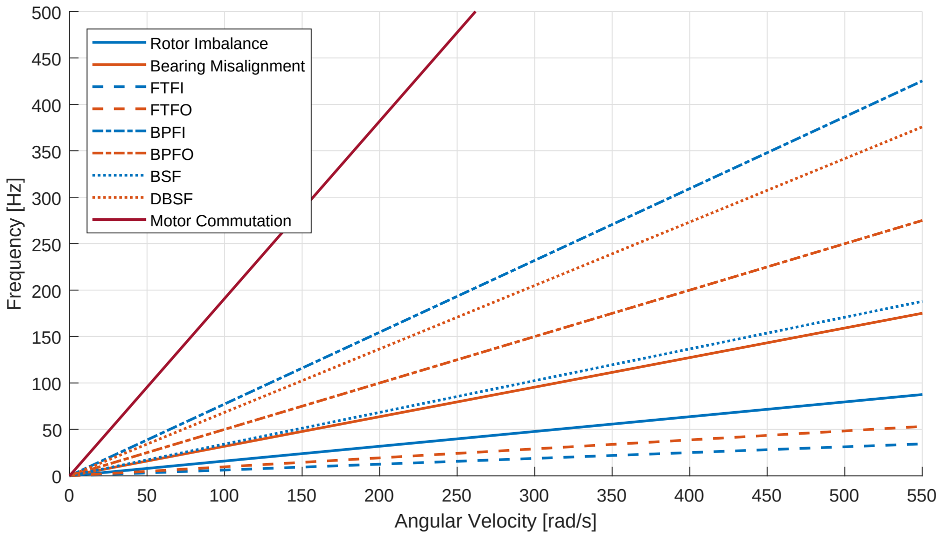

Figure 3.11: Campbell diagram for HT-RW4xx disturbances.

The micro-vibration measurements are performed with the help of a Kistler three-component dynamometer, type 9255A (see Figure 3.12), from which both forces, as well as torques can be measured on all three axes. The sampling frequency is $12800\ Hz$, however, due to the Kistler platform's eigenmodes, wheel disturbance frequencies up to $500\ Hz$ will be analysed. While all of the obtained data is interesting to analyse in depth, for the scope of this thesis work only the torque disturbance measurements around the reaction wheel's Z-axis are considered.

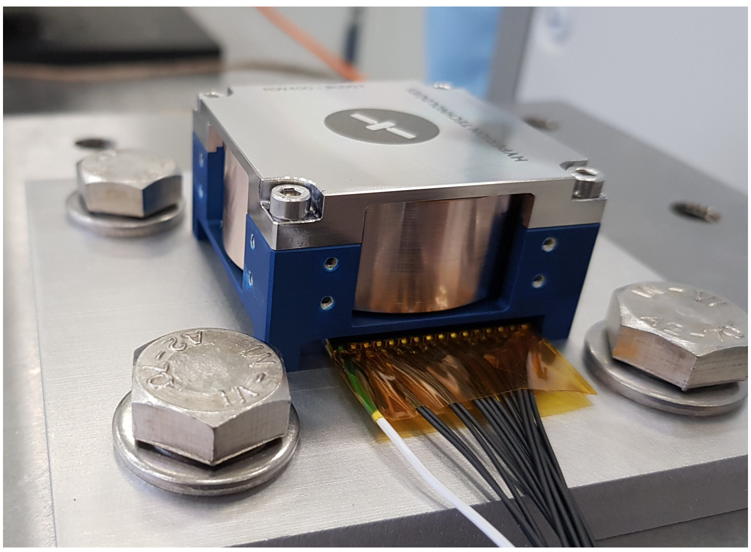

Figure 3.12: HT-RW4xx mounted on a Kistler type 9255A three-component dynamometer.

Prior to performing the actual measurement, a background measurement is performed, with the reaction wheel unit mounted on the Kistler platform. This is done in order to be able to distinguish between the resonance modes caused by the surrounding environment, and the modes of the wheel. The background measurement result is presented in Figure 3.13, and, as it can be observed, a number of resonance frequencies can easily be identified. These are a result of the main supply lines, as well as of the various machines that are running in the facility.

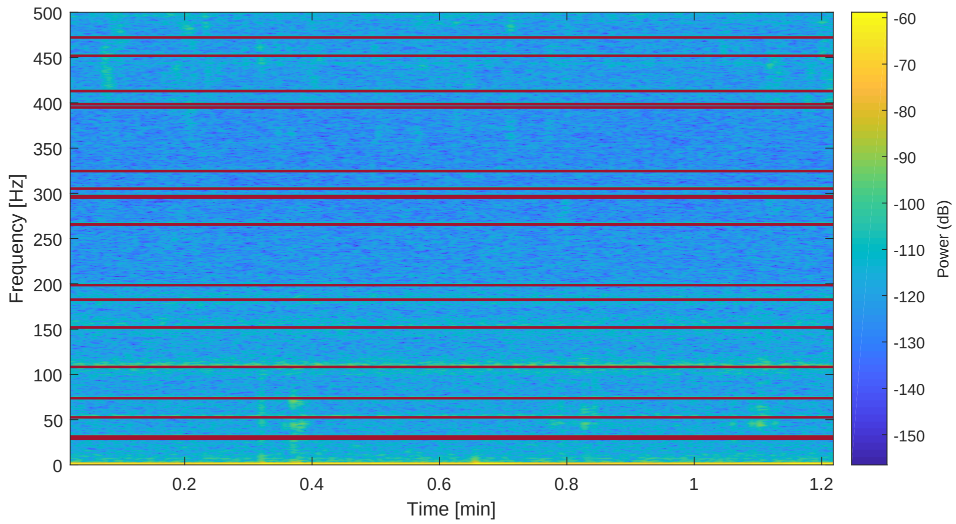

Figure 3.13: Background noise measurements taken with the Kistler platform. The background generated resonances are marked with red lines.

The test profile that has been run on the Kistler platform is a full throttle, open-loop acceleration of the reaction wheel unit. This is done so that any micro-oscillations due to the wheel's speed controller are avoided, while also allowing for the evaluation of the commutation ripple's full impact on the micro-vibration signature of the reaction wheel. The results of the measurement are presented as a waterfall plot, in Figure 3.14. It is important to note that the resonances that appear around $110\ Hz$, $400\ Hz$, and $450\ Hz$ are due to the measurement platform (background noise, as noted in Figure 3.13), and not due to the reaction wheel unit.

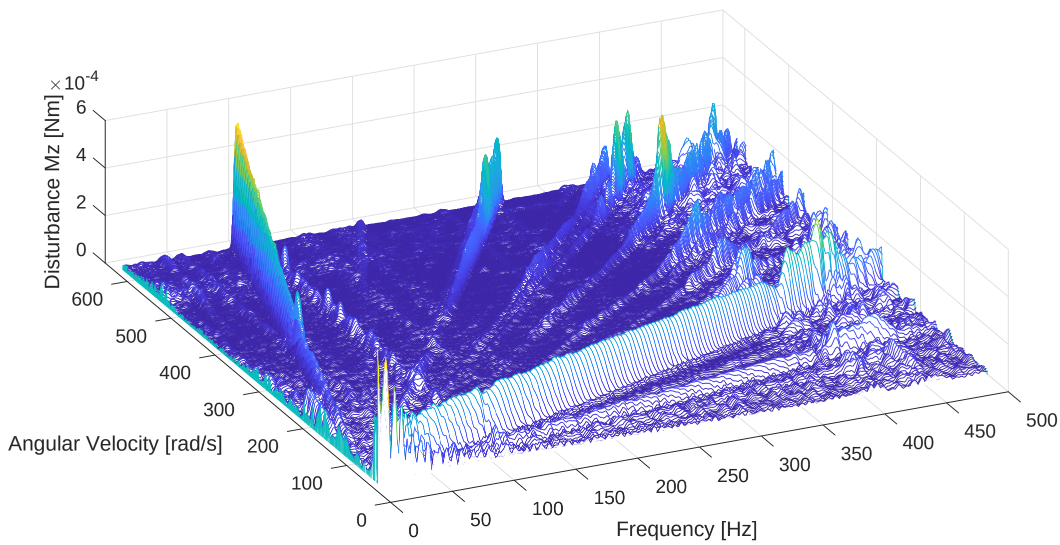

Figure 3.14: Micro-vibration measurement results of the HT-RW4xx.

In order to evaluate the accuracy of the disturbance models, the micro-vibration measurements are re-plotted using a logarithmic scale for the amplitude of the disturbances. The modelled disturbances are then overlayed on top of the measurements. This is shown in Figure 3.15. As it can be observed, not all of the previously discussed disturbance models fit exactly the measurements. Furthermore, more pronounced disturbances appear in the measurements, at orders that have not been initially considered, while some of the discussed disturbances are not as strong, or are not even present in the measurements (i.e. the FTFO, and BSF disturbance orders are not visible even on a logarithmic scale).

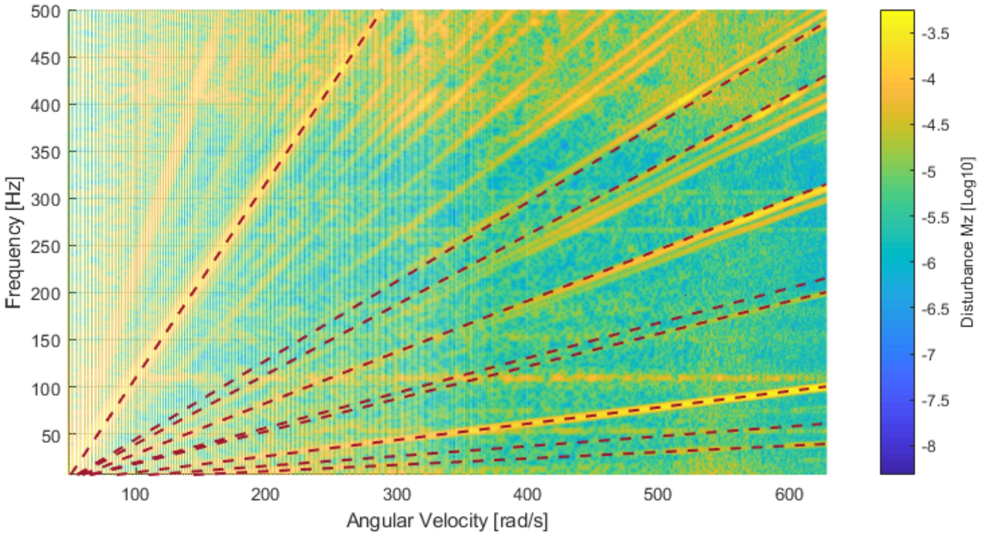

Figure 3.15: Measured disturbance compared to the proposed disturbance models.

As a result of these observations, the FTFO and BSF disturbances are no longer considered. Furthermore, the rest of the previously discussed disturbance models are adjusted to better fit the measurements, while the orders of the disturbances that appear at higher frequencies are determined (up to order 10). Figure 3.16 presents the new disturbance models, as well as the adjusted ones, overlayed on the Kistler platform measurements.

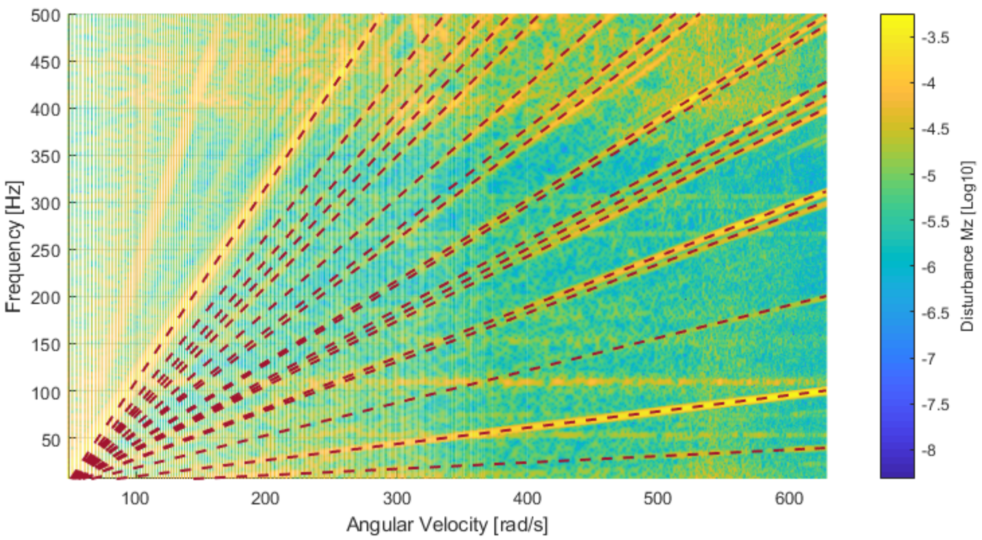

Figure 3.16: Measured disturbances compared to the adjusted disturbance models.

The scaling coefficients required to compute the torque amplitudes corresponding to each disturbance order are also computed using the measurement data, and are presented in Figure 3.17.

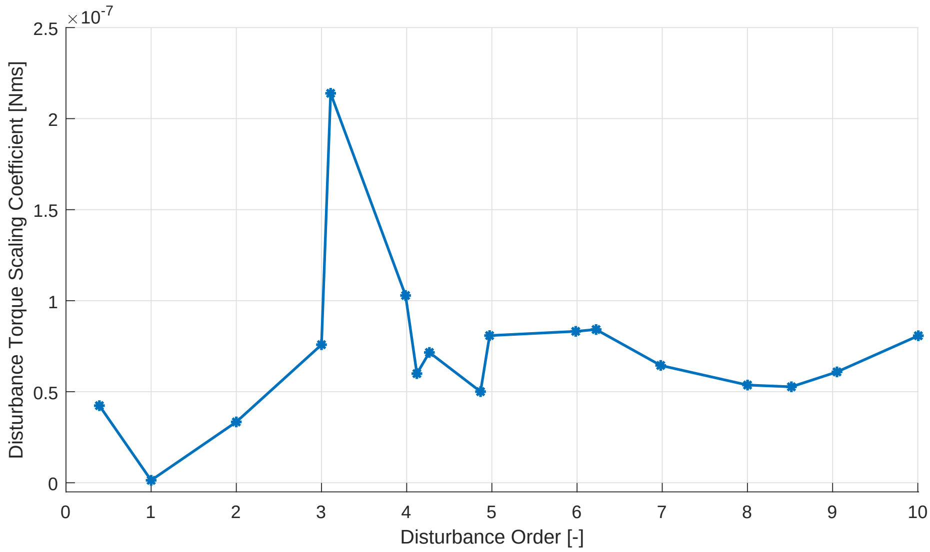

Figure 3.17: Computed disturbance scaling coefficients, required for obtaining the torque amplitudes specific to each disturbance order.

3.4. Impact of Launch Vibrations on Reaction Wheel Disturbances

As with every space system, the reaction wheels experience high vibration levels during launch. As expected, these launch vibrations impact the behaviour of the wheels. However, each wheel is affected in a different way, thus, modelling the effect of launch vibrations is not possible. In order to ensure a certain quality of the units being flown on spacecraft, characterisation experiments must be performed before and after an acceptance vibration test (simulating launch vibrations for a short period of time).

Evidently, the component that is most affected by launch vibration is the bearing assembly of the reaction wheel. Thus, changes will arise both in the micro-vibration signature of the reaction wheels, as well as in their friction behaviour. In terms of the reaction wheel micro-vibration signature, as well as its structural resonance frequencies and amplitudes, variations in the range of $\pm 10\%$ are normally accepted. Changes in bearing friction mostly consist of an increase/decrease in the overall friction, with the occurrence of spikes having a higher probability due to damaged bearings.

3.5. Integration of Disturbance Models into the Overall Simulation

The disturbance models presented in the previous sections of this chapter are integrated into the overall reaction wheel simulation.

In the case of friction variation that arises due to environmental temperature changes, it is integrated into the simulation using a switch, through which the friction curves. specific to $-20°C$, as well as to $+40°C$, are selected. The state of the switch is then controlled by defining the operating temperature in the parameter definition script. The coil resistance variation over temperature is implemented in the parameter definition script as a function of the operating temperature.

Friction disturbances such as spikes, and plateaus, as well as friction spread, are implemented in the simulation with the help of a step function (for friction spread and plateaus), or by using an impulse-like function (for friction spikes).

Micro-vibration type disturbances are periodic in nature, directly related to the rotation speed of the wheel, as has been shown in Section 3.3. Therefore, the disturbances are implemented as sinusoid functions, having the rotation speed of the wheel as input. Thus, the state-space model used to describe the n^{th} sinusoidal disturbance is given in (3.9).

$$\frac{d}{dt}\begin{bmatrix} T_{d_{n_1}} \\ T_{d_{n_2}} \end{bmatrix} = \underbrace{\begin{bmatrix} 0 & k_n \cdot \omega_m \\ -k_n \cdot \omega_m & 0 \end{bmatrix}}_{S_{d_n}} \cdot \begin{bmatrix} T_{d_{k_1}} \\ T_{d_{k_2}} \end{bmatrix} \tag{3.9}$$

The total disturbance torque due to micro-vibration, $T_{d_{vibe}}$, is given in (3.10). This is then simply added as part of the load torque input into the reaction wheel.

$$T_{d_{vibe}} = \begin{bmatrix} -\frac{k_{d_i}}{J}\omega_m^2 & 0 & -\frac{k_{d_1}}{J}\omega_m & 0 & -\frac{k_{d_2}}{J}\omega_m & 0 & \cdots & -\frac{k_{d_{N_d}}}{J}\omega_m & 0 \end{bmatrix} \cdot \begin{bmatrix} T_{d_{i1}} \\ T_{d_{i2}} \\ T_{d_{11}} \\ T_{d_{12}} \\ T_{d_{21}} \\ T_{d_{22}} \\ \vdots \\ T_{d_{N_d}1} \\ T_{d_{N_d}2} \end{bmatrix} \tag{3.10}$$

With these disturbances integrated into the reaction wheel simulation, the observer performance can be adequately evaluated.

3.6. Conclusion

In this chapter, a variety of reaction wheel disturbances have been presented. A detailed discussion of the source of each disturbance is given, followed by numerous experiments that evaluate the impact of the disturbances on the reaction wheel's performance.

Based on the experimental data obtained throughout the characterisation tests, simple, empirical disturbance models are proposed for integration into the reaction wheel simulation. The updated simulation, as a result, is better suited to evaluate the state estimator that is developed throughout Chapter 4.

4

Reaction Wheel State Observer Design and Performance Evaluation

The following chapter, is divided into two parts. First, the Hall sensor placement error estimation problem is discussed in Section 4.1. An approach that makes use of measurements of the motor back-EMF is proposed for the computation of the true rotor position corresponding to the Hall sensor transitions. This is achieved by solving a trigonometric problem, for which the integrated back-EMF signal is used as input. The performance of the Hall sensor placement error estimation algorithm is then evaluated.

In the second part of the chapter, Section 4.2, a linear parameter varying observer structure is proposed in order to estimate the states of the reaction wheel (i.e.: angular position, angular velocity, motor currents, as well as a few disturbances that act on the reaction wheel). The proposed observer makes use of the rotating reference frame model of the reaction wheel, augmented with disturbance models in order to provide the designed observer with a better degree of robustness. This is followed by a system observability analysis, in order to determine the degree to which the reaction wheel states and disturbances can be estimated, with different sensor information. Synthesis of the observer feedback gain is then achieved through an optimization problem, subject to parameter dependent matrix inequalities. Finally, a performance evaluation is carried out on the obtained state and disturbance estimator.

4.1. Hall Sensor Placement Error Estimation

The placement error of the Hall sensors is tackled separately from the other disturbances in the reaction wheel system. This is due to the fact that the available sensor information, during active operation of the reaction wheel, is not sufficient for an adequate estimation of the true angular position of the rotor, and, hence, the sensor placement error.

A different method is proposed in Section 4.1.1, that is run as a calibration routine when the reaction wheel system is turned on, or restarted. The method has been designed such that magnetic flux distribution (back-EMF shape) does not play a role in determining the rotor angular position, thus, the method can be applied un-altered to motors that have different magnetic flux distributions. The estimation performance of the proposed algorithm is then evaluated in Section 4.1.2.

4.1.1. Algorithm Description

First, the reaction wheel is driven to an angular velocity for which the motor back-EMF measurements have a good signal-to-noise ratio (in the case of the HT-RW4xx, this angular velocity would be at around $50\,rad/s$). Once the rotation speed reaches the desired reference, and stabilizes, a coasting command is sent to the reaction wheel. This is done in order to eliminate all the interference in the back-EMF signal caused by driving the motor.

Making the assumption that the reaction wheel is at constant speed, the phase-to-phase back-EMF is measured and integrated (specifically e_{ab}, and e_{bc}). Due to the fact that integration is, in essence, a low-pass filter, the high frequency content of the measured back-EMF is removed (noise, and higher order harmonics present in the back-EMF due to the construction of the motor). Thus, the integrated back-EMF output is a sinusoidal shaped signal (having a $-\pi/2$ phase-shift), which is directly related to the rotor's angular position. Making use of this property, it is easy to apply the algorithm (with absolutely no modifications) to multiple reaction wheel series, which have motors with different magnetic flux distributions.

At the moment of each Hall sensor transition, the value of the integrated back-EMF signals, is saved into an array. Once the measurement part of the routine is over, using the acquired measurements at each Hall transition, the real position of the Hall sensors can be obtained by solving the equation presented in (4.1).

$$\begin{cases} \cos\left(\frac{2\pi}{3} - \theta_x\right) & = & y_1 \\ \cos\left(\frac{2\pi}{3} + \theta_x\right) & = & y_2 \end{cases} \text{, with } \theta_x \in [0;\ 2\pi] \tag{4.1}$$

with θ_x representing the rotor position, and y_1, and y_2 being the values of the two integrated back-EMF signals, at the moment of the Hall sensor transition. The solution to (4.1) is presented in (4.2).

$$\theta_x = \begin{cases} \frac{\pi}{3}, & \text{with } y_1 = \frac{1}{2}, \text{ and } y_2 = -1 \\ \pi, & \text{with } y_1 = \frac{1}{2}, \text{ and } y_2 = \frac{1}{2} \\ 2\left(\pi n - \arctan\left(\frac{\sqrt{3} - 2\sqrt{1 - y_1^2}}{1 - 2y_1}\right)\right), & \text{with } y_1 \neq \frac{1}{2},\ y_2 = \frac{1}{2}\left(-y_1 - \sqrt{3 - 3y_1^2}\right), \text{ and } n \in \mathbb{Z} \\ 2\left(\pi n + \arctan\left(\frac{\sqrt{3} + 2\sqrt{1 - y_1^2}}{2y_1 - 1}\right)\right), & \text{with } y_1 \neq \frac{1}{2},\ y_2 = \frac{1}{2}\left(-y_1 + \sqrt{3 - 3y_1^2}\right), \text{ and } n \in \mathbb{Z} \end{cases} \tag{4.2}$$

The flow diagram of the Hall sensor placement error estimation routine is presented in Figure 4.1. The routine must be run after a reaction wheel system boot-up, or power cycle, however, it can be run at any time during the reaction wheel's service life, as a re-calibration for the Hall sensor placement error values.

Having obtained the real position of the Hall sensor transition, the error between this value and the expected, ideal position of the sensor transition, can be computed. Finally, the computed error is then used to compensate the error in the position measurement that is used in the observer designed in Section 4.2.

4.1.2. Performance Evaluation

As discussed in Section 2.2.2, the HT-RW4xx reaction wheel contains three digital Hall sensors, placed around the stator at $120°$ from one another. These three Hall sensors are denoted by $H1$, $H2$, and $H3$.

In order to evaluate the performance of the Hall sensor placement error estimator, simulations using various back-EMF sampling frequencies, F_s, are performed (400 simulations are executed for each test case). The estimated angular position of the rising edge (transition of the Hall sensor output from logical 0 to logical 1), and the falling edge (transition of the Hall sensor output from logical 1 to logical 0) for each one of the H1, H2, and H3 Hall sensors is compared to the true position by evaluating the estimation error.

First, a noise free test case is performed, using a sampling frequency $F_s = 500\ kHz$ for the back-EMF measurement, in order to establish the ideal accuracy of the method. The result of this test case is presented in Figure 4.2. As can be observed from Figure 4.2, the ideal case accuracy of the method is quite good, the Hall sensor position estimation in all cases remains within $\pm 3 \cdot 10^{-3}$ degrees.

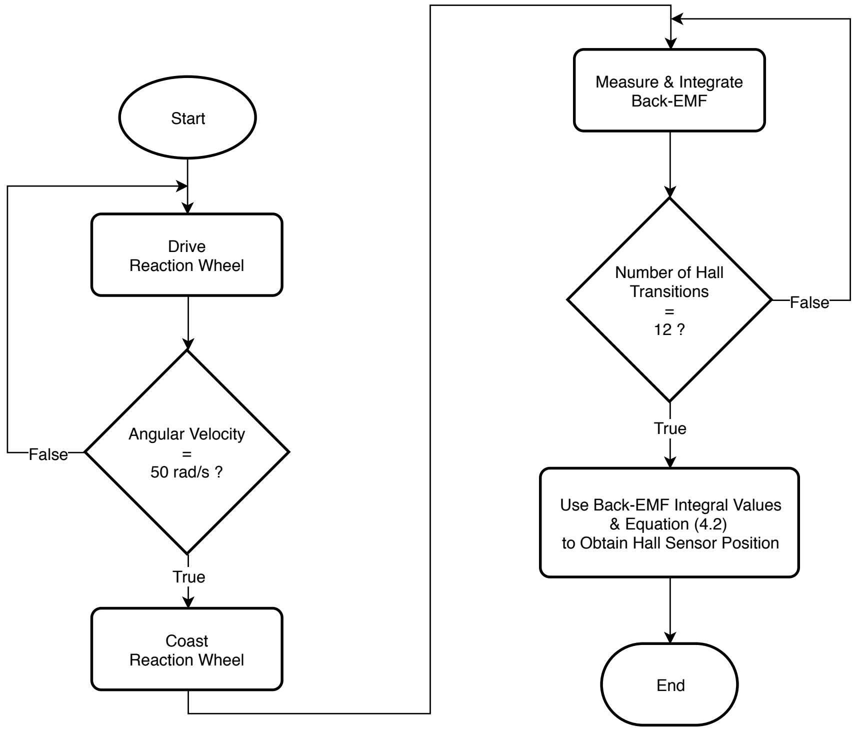

Figure 4.1: Flow diagram of the Hall sensor placement error estimation routine.

The noiseless test case is followed by test cases for which a noise variance of $\sigma_{noise}^2 = 4.258 \cdot 10^{-6}$ (obtained from measurement equipment noise measurement) is used. The performance is evaluated for three different sampling frequencies, namely $F_s = 10\ kHz$ (results presented in Figure 4.3), $F_s = 50\ kHz$ (results presented in Figure 4.4), and $F_s = 500\ kHz$ (results presented in Figure 4.5) for the back-EMF measurements. The mean, μ, and the standard deviation, σ, of each Hall sensor's rising, and falling edges' position estimation error are averaged, in order to provide a more convenient performance metric. An overview of these averaged means and standard deviations, for the different test cases, is presented in Table 4.1. It can be observed that the Hall sensor position estimation accuracy improves with increasing back-EMF sampling frequency. This is to be expected since the back-EMF integral becomes more accurate for higher sampling frequencies.

Table 4.1: Average mean and standard deviation of the Hall sensor placement estimation error, obtained from test runs with $\sigma_{noise}^2 = 4.258 \cdot 10^{-6}$ noise variance, for three different sampling frequencies, F_s.

	$H1$	$H2$	$H3$
$F_s = 10\ kHz$	$\mu = -0.015°$ $\sigma = 0.2°$	$\mu = -0.013°$ $\sigma = 0.088°$	$\mu = 0.011°$ $\sigma = 0.087°$
$F_s = 50\ kHz$	$\mu = 0.003°$ $\sigma = 0.125°$	$\mu = 0.007°$ $\sigma = 0.023°$	$\mu = 0.006°$ $\sigma = 0.023°$
$F_s = 500\ kHz$	$\mu = 0.002°$ $\sigma = 0.034°$	$\mu = -0.002°$ $\sigma = 0.004°$	$\mu = 0.002°$ $\sigma = 0.004°$

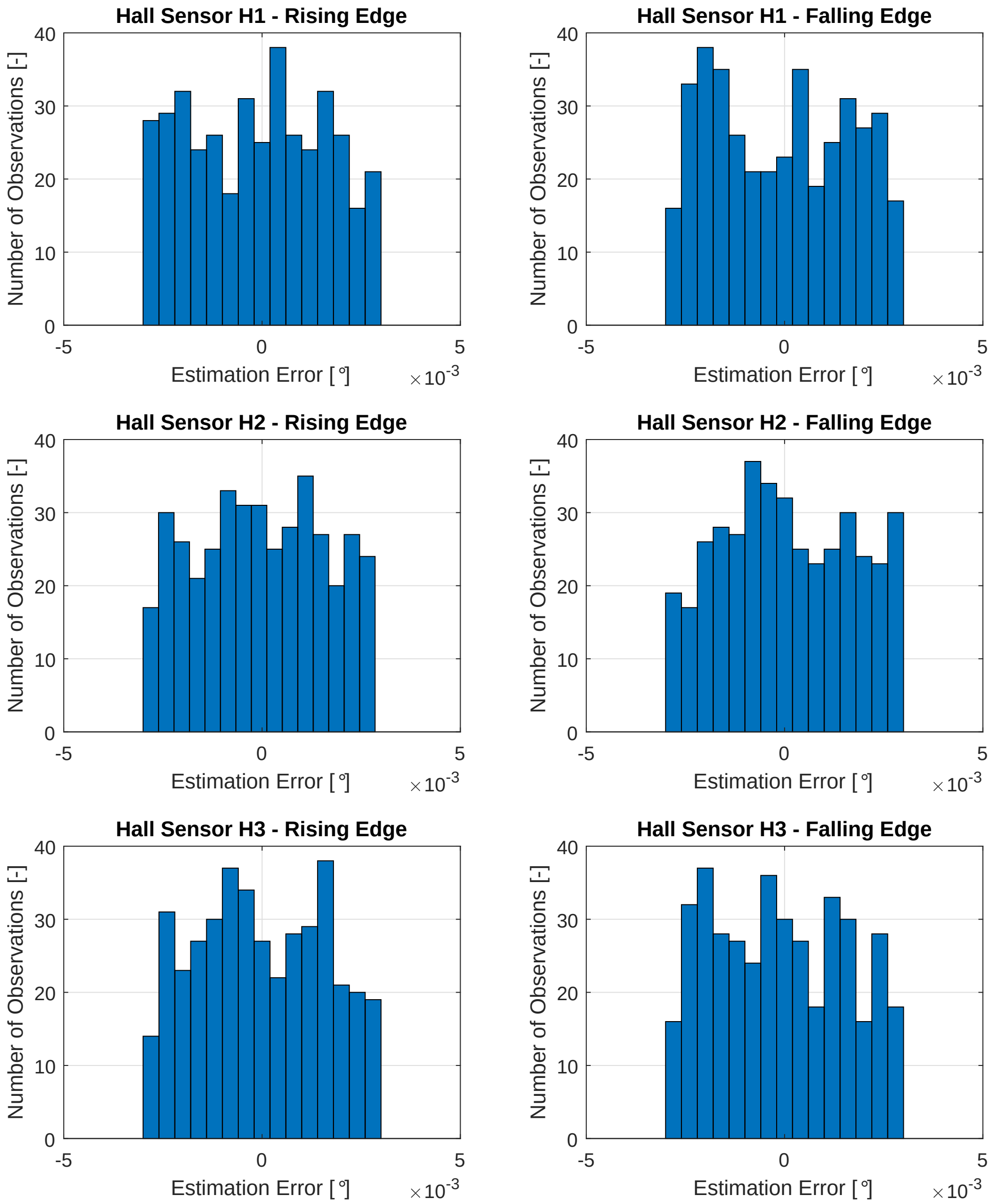

Figure 4.2: Hall sensor position estimation error distribution. Test case: $\sigma^2_{noise} = 0$, $F_s = 500\ kHz$.

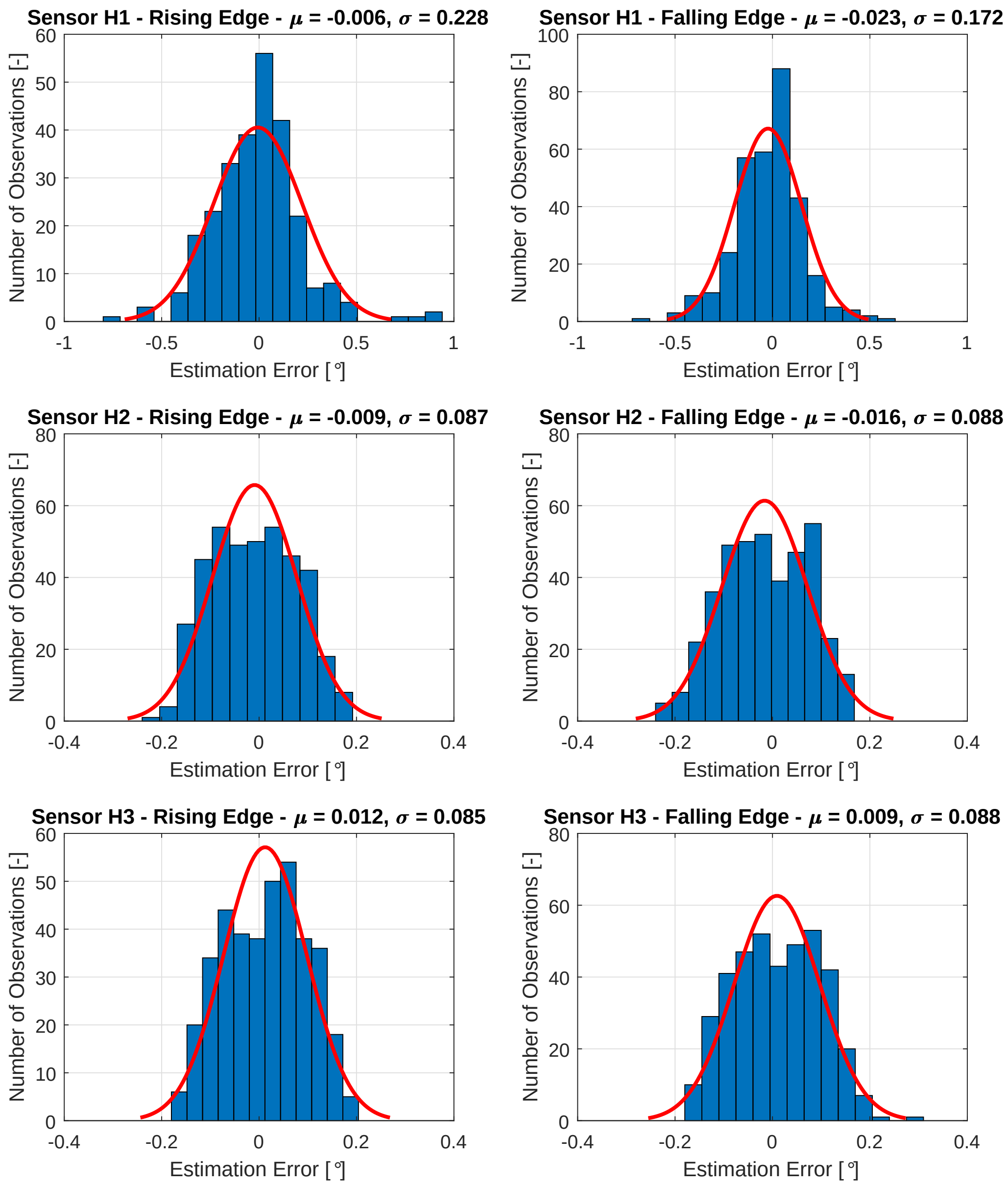

Figure 4.3: Hall sensor position estimation error distribution. Test case: $\sigma^2_{noise} = 4.258 \cdot 10^{-6}$, $F_s = 10\ kHz$.

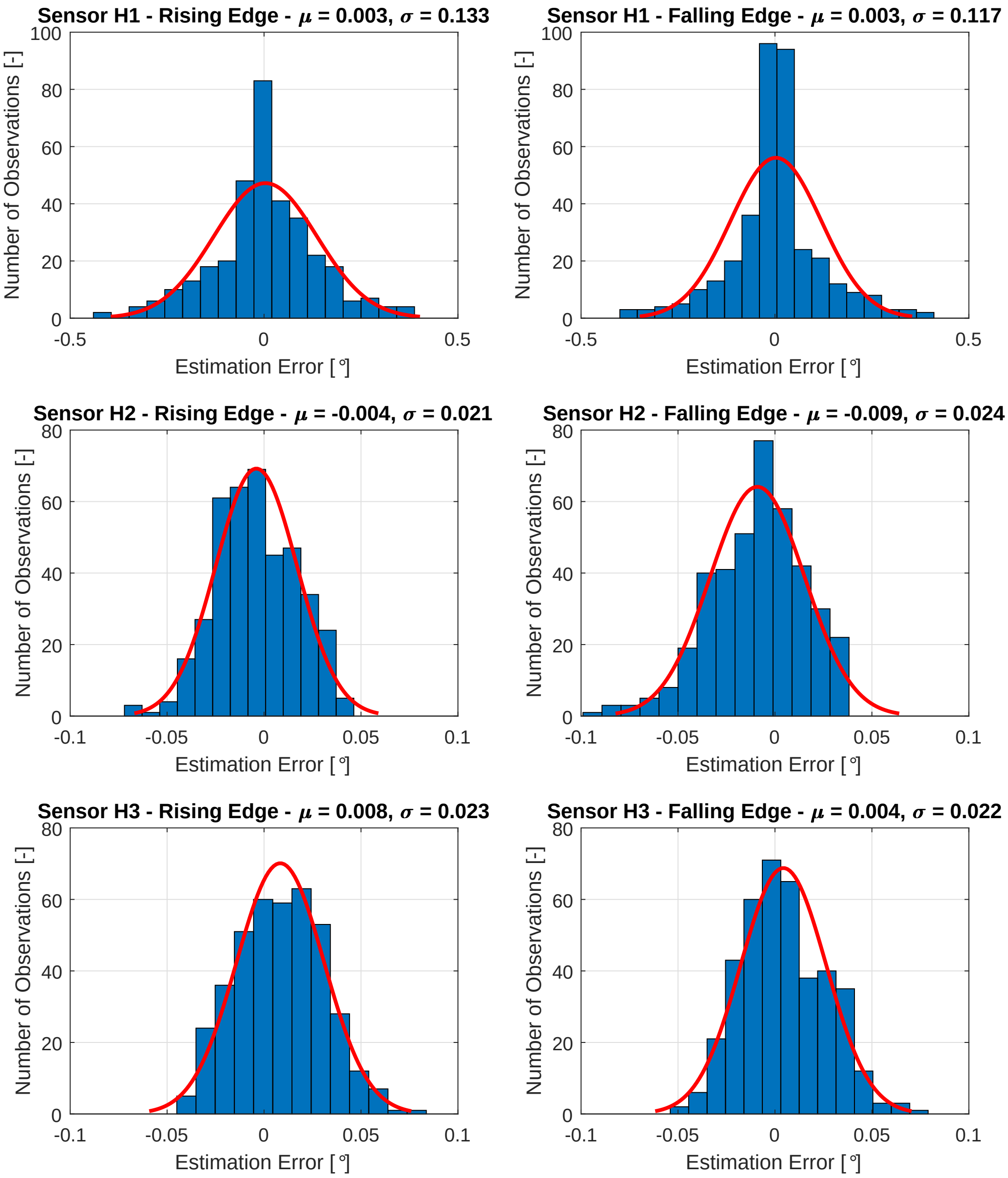

Figure 4.4: Hall sensor position estimation error distribution. Test case: $\sigma^2_{noise} = 4.258 \cdot 10^{-6}$, $F_s = 50\ kHz$.

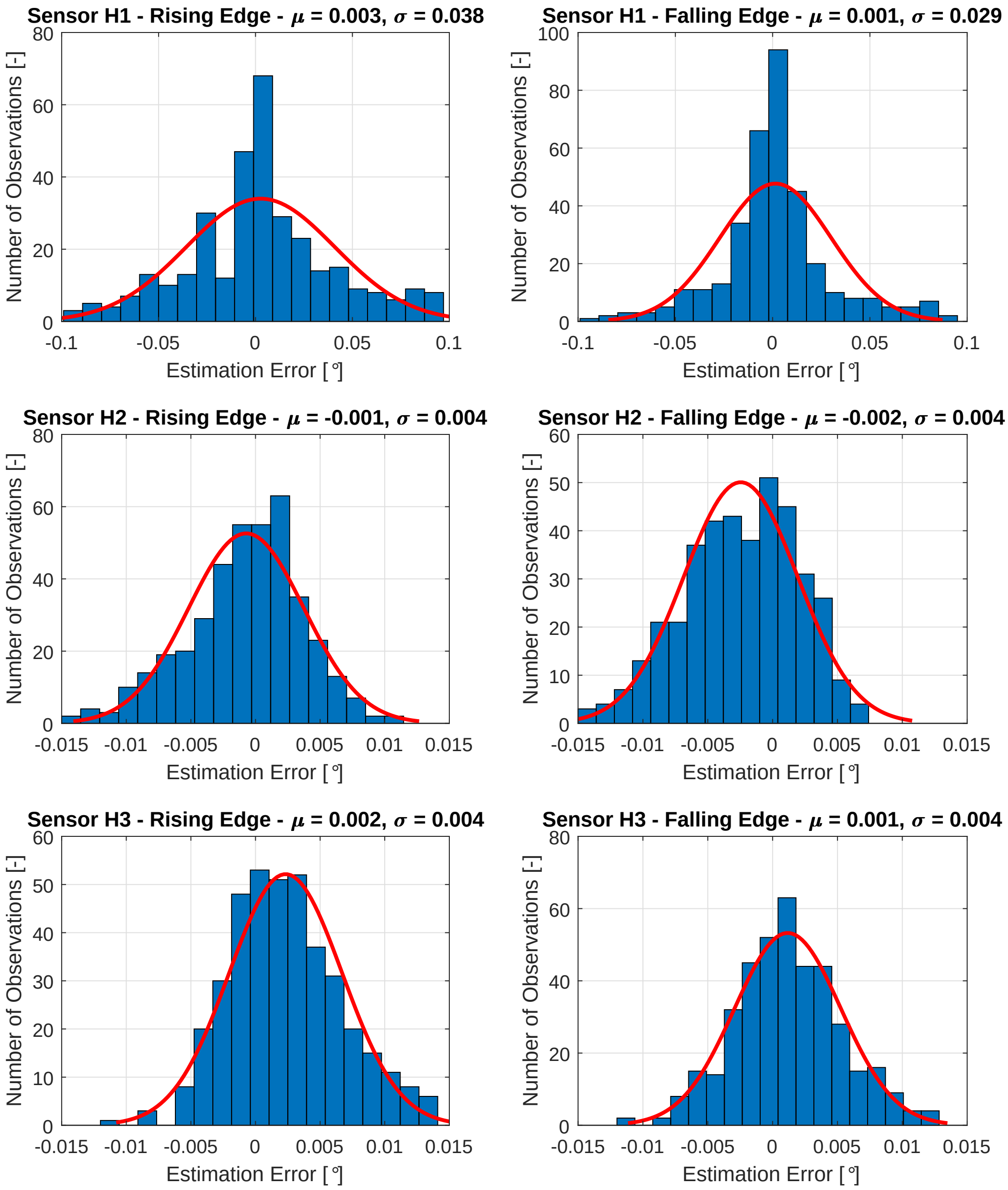

Figure 4.5: Hall sensor position estimation error distribution. Test case: $\sigma^2_{noise} = 4.258 \cdot 10^{-6}$, $F_s = 500\ kHz$.

4.2. Linear Parameter Varying State Observer

Accurate information about the reaction wheel system's states is important for advanced commutation methods, as well as high accuracy angular velocity control. In the pursuit of providing such accurate state information (especially rotor angular position), a state observer is designed and evaluated.

The observer design is performed in several separate steps. First, the rotating reference frame model, which will be at the base of the state estimator, is formulated in Section 4.2.1. The rotating reference frame model is then augmented with additional unknown disturbance signals, in Section 4.2.2, in order to account for un-modelled phenomena, or for modelling/measurement inaccuracies. This is followed by a system observability analysis, in Section 4.2.3, in order to determine what sensor information is required to estimate the augmented system states.

In Section 4.2.4, the observer synthesis is formulated as a mean squared estimation error minimization problem, subject to parameter dependent matrix inequality constraints. Finally, the performance of the observer is evaluated, in Section 4.2.5, for several reaction wheel operating scenarios.

4.2.1. Rotating Reference Frame Model

The model presented in Chapter 2 is used in the simulation of the physical reaction wheel system. The model contains non-linearities, both in its states, as well as in its input signals, that are dependent on the rotor's electrical position, θ_e. Due to this, the complexity of designing and implementing the reaction wheel state observer increases. In order to reduce the complexity of the model used in the observer design, the Clarke and the Park transforms are employed to obtain a rotating reference frame model of the reaction wheel.

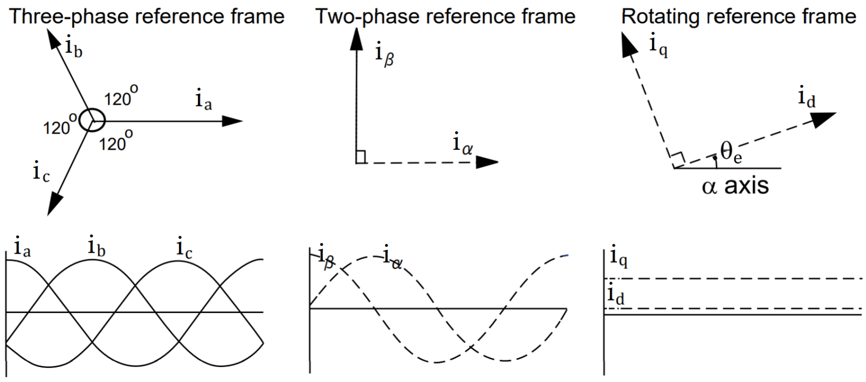

Figure 4.6: Reference frames obtained via the Clarke (middle) and the Park (right) transforms [3].

The graphical representations of the Clarke and Park transforms are presented in Figure 4.6. The Clarke transform converts the balanced three-phase variables into balanced two-phase orthogonal variables. The Park transform further takes these two-phase variables and converts them from the orthogonal stationary reference frame to the orthogonal rotating reference frame. Since the motor used in the HT-RW4xx reaction wheels has balanced voltages and currents, the simplified Clarke transform can be used [22]. The combined Clarke and Park transforms are given in (4.3).

$$P(\theta_e) = \frac{2}{3}\begin{bmatrix} \cos(\theta_e) & \cos\left(\theta_e - \frac{2\pi}{3}\right) & \cos\left(\theta_e + \frac{2\pi}{3}\right) \\ -\sin(\theta_e) & -\sin\left(\theta_e - \frac{2\pi}{3}\right) & -\sin\left(\theta_e + \frac{2\pi}{3}\right) \end{bmatrix} \tag{4.3}$$

The inverse Park transform is used to go back from the rotating reference frame representation to the normal three-phase representation, and is given in (4.4).

$$P^{-1}(\theta_e) = \begin{bmatrix} \cos(\theta_e) & -\sin(\theta_e) \\ \cos\left(\theta_e - \frac{2\pi}{3}\right) & -\sin\left(\theta_e - \frac{2\pi}{3}\right) \\ \cos\left(\theta_e + \frac{2\pi}{3}\right) & -\sin\left(\theta_e + \frac{2\pi}{3}\right) \end{bmatrix} \tag{4.4}$$

Since the magnetic flux distribution of the reaction wheel's motor is sinusoidal, no adjustments are required for the Clarke and Park transforms [16]. Thus, the reaction wheel model, formulated in the motor's rotating reference frame, that is to be used in the observer design, is given in (4.5).

$$\begin{aligned} \frac{d}{dt}\begin{bmatrix} i_d \\ i_q \\ \omega_m \\ \theta_e \end{bmatrix} &= \underbrace{\begin{bmatrix} -\frac{R_s(T)}{L_s} & N\cdot\omega_m & 0 & 0 \\ -N\cdot\omega_m & -\frac{R_s(T)}{L_s} & -\frac{N}{L_s}k_e & 0 \\ 0 & \frac{3}{2}\frac{N}{J}k_t & -\frac{k_f(T,\omega_m)}{J} & 0 \\ 0 & 0 & N & 0 \end{bmatrix}}_{=A(t)} \cdot \underbrace{\begin{bmatrix} i_d \\ i_q \\ \omega_m \\ \theta_e \end{bmatrix}}_{=x(t)} + \underbrace{\begin{bmatrix} \frac{1}{L_s} & 0 \\ 0 & \frac{1}{L_s} \\ 0 & 0 \\ 0 & 0 \end{bmatrix}}_{=B} \cdot \underbrace{\begin{bmatrix} v_d \\ v_q \end{bmatrix}}_{=u(t)} \\ y(t) &= \underbrace{\begin{bmatrix} 1 & 0 & 0 & 0 \\ 0 & 1 & 0 & 0 \\ 0 & 0 & 1 & 0 \\ 0 & 0 & 0 & 1 \end{bmatrix}}_{=C} \cdot \begin{bmatrix} i_d \\ i_q \\ \omega_m \\ \theta_e \end{bmatrix} \end{aligned} \tag{4.5}$$

where $x(t) \in \mathbb{R}^{n_x}$ is the state vector, $u(t) \in \mathbb{R}^{n_u}$ is the known voltage input vector, and $y(t) \in \mathbb{R}^{n_y}$ is the system output vector. Matrix $B \in \mathbb{R}^{n_x \times n_u}$ is the system input matrix, and $C \in \mathbb{R}^{n_y \times n_x}$ is the system output matrix. As can be observed, the state matrix $A(t) \in \mathbb{R}^{n_x \times n_x}$ changes over time due to containing parameters that vary as functions of temperature, T, and as functions of angular velocity, ω_m. It can, thus, be concluded that the system described in (4.5) is a quasi-LPV system, since the system state matrix A is dependent on one of its states, namely the mechanical angular velocity, ω_m.

The advantage of using the rotating reference frame model of the reaction wheel in the state estimator design is twofold. First, this representation allows for the direct estimation of the currents that determine the strength of the quadrature and the direct components of the magnetic field generated by the stator coils, as is described in Section 2.1.2. Secondly, the rotating reference frame representation inherently keeps the rotor magnetic field and the stator magnetic field orthogonal to each other, as long as the rotor position information is of adequate quality.

4.2.2. Augmented LPV System Description

Throughout its operation, the reaction wheel is affected by various disturbances. As it would be expected, not all disturbances can be modelled, and, in the case they are, the models may have inaccuracies, or they would simply become less accurate as the operating parameters of the reaction wheel change, and are not measured accurately. In order to account for these issues, and other unknowns, the state observer model is augmented with a set of disturbances, thus, increasing the estimator's robustness.

As presented in Section 2.2.3, the reaction wheel's angular velocity, ω_m, is obtained by measuring the time between two Hall-sensor transitions. This method provides an adequate measurement of the angular velocity during steady-state operation, however, during the wheel's acceleration, the measurement contains an error due to its inherent averaging behaviour. In order to account for this, an unknown measurement error, $\omega_{m_{err}}$, is inserted into the observer model. It should be noted that no error is considered in the measurement of the rotor electrical angular position, θ_e, as this has been resolved in Section 4.1, thus, an error free position measurement is considered for the observer design.

The output torque of the reaction wheel system is subjected to a number of disturbances. The sources of these disturbances are various, such as lubricant thermal properties, bearing imperfections, rotor imbalance, etc. As explained in Section 3.2.2, friction spikes and plateaus are a common occurrence in reaction wheel systems, although they are unpredictable.

Furthermore, modelling inaccuracies of the reaction wheel's friction requires extra attention. An erroneous value of the friction coefficient is highly likely considering that it is a function of both angular velocity, and temperature (measurement of the bearing temperature being particularly difficult), as shown in Figure . Furthermore, the spread in reaction wheel friction curve (presented in Section 3.2.1) is another point that requires attention. In order to account torque disturbances/mismatches, an unknown load torque disturbance, T_l, is introduced into the observer model.

The last reaction wheel parameter that is highly prone to errors is the motor coil resistance. The reason for the high error susceptibility is due to the high difficulty of obtaining correct/accurate measurements of the motor coil operating temperature, the motor coil resistance being dependent on temperature, as shown in (4.6).

$$R_s(T) = R_{ref} \cdot \left[1 + \alpha \cdot \left(T - T_{ref}\right)\right] \tag{4.6}$$

where $\alpha = 0.004\ K^{-1}$ is the thermal coefficient of the coil, T_{ref} is the reference temperature, and R_{ref} is the coil resistance at the reference temperature. Once again, with the goal of accounting for the likely difference between the coil resistance of the reaction wheel system, and the value used in the state estimator, the unknown disturbance voltages, v_{d_d}, and v_{d_q}, are introduced into the direct current, and into the quadrature current equations, respectively.

The observer model, including state disturbances, and measurement errors, is then described in (4.7), and in (4.8).

$$\begin{aligned}\frac{d}{dt}\begin{bmatrix} i_d \\ i_q \\ \omega_m \\ \theta_e \end{bmatrix} &= \begin{bmatrix} -\frac{R_s(T)}{L_s} & N\cdot\omega_m & 0 & 0 \\ -N\cdot\omega_m & -\frac{R_s(T)}{L_s} & -\frac{N}{L_s}k_e & 0 \\ 0 & \frac{3}{2}\frac{N}{J}k_t & -\frac{k_f(T,\omega_m)}{J} & 0 \\ 0 & 0 & N & 0 \end{bmatrix} \cdot \begin{bmatrix} i_d \\ i_q \\ \omega_m \\ \theta_e \end{bmatrix} + \begin{bmatrix} \frac{1}{L_s} & 0 \\ 0 & \frac{1}{L_s} \\ 0 & 0 \\ 0 & 0 \end{bmatrix} \cdot \begin{bmatrix} v_d \\ v_q \end{bmatrix} + \\ &+ \underbrace{\begin{bmatrix} -\frac{1}{L_s} & 0 & 0 \\ 0 & -\frac{1}{L_s} & 0 \\ 0 & 0 & -\frac{1}{J} \\ 0 & 0 & 0 \end{bmatrix}}_{=B_{d_x}} \cdot \underbrace{\begin{bmatrix} v_{d_d} \\ v_{d_q} \\ T_l \end{bmatrix}}_{=d_x(t)}\end{aligned} \tag{4.7}$$

$$y(t) = \begin{bmatrix} 1 & 0 & 0 & 0 \\ 0 & 1 & 0 & 0 \\ 0 & 0 & 1 & 0 \\ 0 & 0 & 0 & 1 \end{bmatrix} \cdot \begin{bmatrix} i_d \\ i_q \\ \omega_m \\ \theta_e \end{bmatrix} + \underbrace{\begin{bmatrix} 0 \\ 0 \\ 1 \\ 0 \end{bmatrix}}_{=D_{d_y}} \cdot \underbrace{\omega_{m_{err}}}_{=d_y(t)} \tag{4.8}$$

where $B_{d_x} \in \mathbb{R}^{n_x \times n_{d_x}}$ is the disturbance input matrix, $d_x(t) \in \mathbb{R}^{n_{d_x}}$ is the state disturbance vector, $D_{d_y} \in \mathbb{R}^{n_y \times n_{d_y}}$ is the measurement error matrix, $d_y(t) \in \mathbb{R}^{n_{d_y}}$ is the measurement error vector.

Since the previously discussed disturbances/errors need to be estimated as well, a constant/slow-varying signal model is proposed for them. This model is then used to augment the model used in the state estimator.

The augmented observer model is then described in (4.9), and in (4.10).

$$\frac{d}{dt}\begin{bmatrix} i_d \\ i_q \\ \omega_m \\ \theta_e \\ v_{d_d} \\ v_{d_q} \\ \omega_{m_{err}} \\ T_l \end{bmatrix} = \underbrace{\begin{bmatrix} -\frac{R_s(T)}{L_s} & N \cdot \omega_m & 0 & 0 & -\frac{1}{L_s} & 0 & 0 & 0 \\ -N \cdot \omega_m & -\frac{R_s(T)}{L_s} & -\frac{N}{L_s}k_e & 0 & 0 & -\frac{1}{L_s} & 0 & 0 \\ 0 & \frac{3}{2}\frac{N}{J}k_t & -\frac{k_f(T,\omega_m)}{J} & 0 & 0 & 0 & 0 & -\frac{1}{J} \\ 0 & 0 & N & 0 & 0 & 0 & 0 & 0 \\ 0 & 0 & 0 & 0 & 0 & 0 & 0 & 0 \\ 0 & 0 & 0 & 0 & 0 & 0 & 0 & 0 \\ 0 & 0 & 0 & 0 & 0 & 0 & 0 & 0 \\ 0 & 0 & 0 & 0 & 0 & 0 & 0 & 0 \end{bmatrix}}_{=A_a(t)} \cdot \underbrace{\begin{bmatrix} i_d \\ i_q \\ \omega_m \\ \theta_e \\ v_{d_d} \\ v_{d_q} \\ \omega_{m_{err}} \\ T_l \end{bmatrix}}_{=x_a(t)} + \underbrace{\begin{bmatrix} \frac{1}{L_s} & 0 \\ 0 & \frac{1}{L_s} \\ 0 & 0 \\ 0 & 0 \\ 0 & 0 \\ 0 & 0 \\ 0 & 0 \\ 0 & 0 \end{bmatrix}}_{=B_a} \cdot \begin{bmatrix} v_d \\ v_q \end{bmatrix} \tag{4.9}$$

$$y(t) = \underbrace{\begin{bmatrix} 1 & 0 & 0 & 0 & 0 & 0 & 0 & 0 \\ 0 & 1 & 0 & 0 & 0 & 0 & 0 & 0 \\ 0 & 0 & 1 & 0 & 0 & 0 & 1 & 0 \\ 0 & 0 & 0 & 1 & 0 & 0 & 0 & 0 \end{bmatrix}}_{=C_a} \cdot \begin{bmatrix} i_d \\ i_q \\ \omega_m \\ \theta_e \\ v_{d_d} \\ v_{d_q} \\ \omega_{m_{err}} \\ T_l \end{bmatrix} \tag{4.10}$$

where $A_a(t) \in \mathbb{R}^{n_{x_a} \times n_{x_a}}$ represents the augmented state matrix, $C_a \in \mathbb{R}^{n_y \times n_{x_a}}$ is the augmented system output matrix.

By selecting the parameter vector $\rho(t) = \begin{bmatrix} \underbrace{R_s\big(T(t)\big)}_{=\rho_1(t)} & \underbrace{\omega_m(t)}_{=\rho_2(t)} & \underbrace{k_f\big(T(t), \omega_m(t)\big)}_{=\rho_3(t)} \end{bmatrix}$, the augmented state matrix, $A_a(t)$, can be re-written in terms of $\rho(t)$, as shown in (4.10). As can be observed, $A_a\big(\rho(t)\big)$ is affine in $\rho(t)$.

$$A_a\big(\rho(t)\big) = A_{a_0} + \rho_1(t) \cdot A_{a_1} + \rho_2(t) \cdot A_{a_2} + \rho_3(t) \cdot A_{a_3} \tag{4.11}$$

with the matrices $A_{a_0}, A_{a_1}, A_{a_2}, A_{a_3} \in \mathbb{R}^{n_{x_a} \times n_{x_a}}$ being time-invariant. Furthermore, it should be noted that the parameters $\rho_1(t)$, $\rho_2(t)$, and $\rho_3(t)$ are all bounded (i.e.: $\rho_i(t) \in [\underline{\rho}_i \quad \overline{\rho}_i]$, $i = \overline{1,3}$), and varying inside the polytope $\mathcal{P}_\rho$, defined by $Z = 2^3$ vertices, as seen in (4.12).

$$\begin{aligned} \mathcal{P}_\rho \quad = \quad & \big\{(\underline{\rho}_1, \underline{\rho}_2, \underline{\rho}_3), (\underline{\rho}_1, \underline{\rho}_2, \overline{\rho}_3), (\underline{\rho}_1, \overline{\rho}_2, \underline{\rho}_3), (\underline{\rho}_1, \overline{\rho}_2, \overline{\rho}_3), \\ & (\overline{\rho}_1, \underline{\rho}_2, \underline{\rho}_3), (\overline{\rho}_1, \underline{\rho}_2, \overline{\rho}_3), (\overline{\rho}_1, \overline{\rho}_2, \underline{\rho}_3), (\overline{\rho}_1, \overline{\rho}_2, \overline{\rho}_3)\big\} \end{aligned} \tag{4.12}$$

4.2.3. System Observability Analysis

The observability analysis begins by considering the augmented LPV system described in (4.9), and in (4.10). This system is said to be structurally observable if the observability matrix, $\mathcal{O}(\rho)$, has full column rank for any $\rho(t)$, $\forall t$ (i.e.: rank $\mathcal{O}(\rho) = n_{x_a}$). The observability matrix is defined in (4.13).

$$\mathcal{O}(\rho) = \begin{bmatrix} C_a \\ C_a \cdot A_a(\rho) \\ \vdots \\ C_a \cdot A_a^{n_{x_a}-1}(\rho) \end{bmatrix} \tag{4.13}$$

In order to evaluate the possibility of using a minimum amount of sensors for accurate state estimation, the system observability check is performed for three formulations of the augmented LPV model, described in (4.9). First, the full sensor information case is checked, for which the output, $y(t)$, is described by (4.10).

Next, the Hall sensor measurement only case (i.e.: the angular velocity, and the rotor electrical angular position are obtained from the digital Hall sensor measurements, as described in Section 2.2.2, and Section 2.2.3) is checked. In this case, the output, $y(t)$, is given by (4.14).

$$y(t) = \begin{bmatrix} 0 & 0 & 1 & 0 & 0 & 0 & 1 & 0 \\ 0 & 0 & 0 & 1 & 0 & 0 & 0 & 0 \end{bmatrix} \cdot \begin{bmatrix} i_d \\ i_q \\ \omega_m \\ \theta_e \\ v_{d_d} \\ v_{d_q} \\ \omega_{m_{err}} \\ T_l \end{bmatrix} \tag{4.14}$$

Finally, the two voltage disturbances, $v_{d_d}(t)$, and $v_{d_q}(t)$, are removed from the augmented model, and the Hall sensor measurement only case is checked once again. The output, $y(t)$, is now given by (4.15).

$$y(t) = \begin{bmatrix} 0 & 0 & 1 & 0 & 1 & 0 \\ 0 & 0 & 0 & 1 & 0 & 0 \end{bmatrix} \cdot \begin{bmatrix} i_d \\ i_q \\ \omega_m \\ \theta_e \\ \omega_{m_{err}} \\ T_l \end{bmatrix} \tag{4.15}$$

In order to evaluate the observability of the system, the observability matrix is computed for all the values of $\rho(t)$. The parameters $\rho_1(t)$, $\rho_2(t)$, and $\rho_3(t)$ are, therefore, varied throughout their respective ranges. The rank of each matrix is then obtained by using its singular value decomposition (SVD) [23].

The results of the observability check for all three cases are presented in Table 4.2. It can be observed that the full sensor information case is observable for all values of the parameter vector $\rho(t)$.

In the second case, it can be observed that the two disturbance voltages, $v_{d_d}(t)$, and $v_{d_q}(t)$, are not observable for any value of $\rho(t)$.

Lastly, in the third case, the system is observable, although for $\rho_2(t) = 0$, the observability matrix loses rank. However, performing the Hautus test shows that the system is detectable for $\rho_2(t) = 0$.

Table 4.2: Results of the observability check performed for different state measurements.

Number of States	Measured States	rank $\mathcal{O}(\rho)$		Hautus Test	
		$\rho_2 \neq 0$	$\rho_2 = 0$	$\rho_2 \neq 0$	$\rho_2 = 0$
8	$\begin{bmatrix} i_d & i_q & \omega_m & \theta_e \end{bmatrix}^T$	8	8	n/a	n/a
8	$\begin{bmatrix} \omega_m & \theta_e \end{bmatrix}^T$	6	5	fail	fail
6	$\begin{bmatrix} \omega_m & \theta_e \end{bmatrix}^T$	6	5	n/a	pass

4.2.4. Observer Problem Formulation and Synthesis

In order to synthesize the observer, the following LPV system representation is used for the augmented reaction wheel model:

$$\begin{aligned} \dot{x}_a(t) &= A_a(\rho)\,x_a(t) + B_a u(t) + w(t) \\ y(t) &= C_a x_a(t) + v(t) \end{aligned} \tag{4.16}$$

where $x_a(t) \in \mathbb{R}^{n_{x_a}}$ is the augmented state vector, $u(t) \in \mathbb{R}^{n_u}$ is the known voltage input vector, $y(t) \in \mathbb{R}^{n_y}$ is the measurement output vector, and $\rho(t) \in \mathbb{R}^{n_\rho}$ contains the varying system parameters, as defined in Section 4.2.2. The matrices $A_a(\rho) \in \mathbb{R}^{n_{x_a} \times n_{x_a}}$, $B \in \mathbb{R}^{n_{x_a} \times n_u}$, and $C_a \in \mathbb{R}^{n_y \times n_{x_a}}$ have also been defined in Section 4.2.2.

The signals $v(t) \in \mathbb{R}^{n_v}$, and $w(t) \in \mathbb{R}^{n_w}$ are assumed to be zero-mean, white noise signals. These signals are used to introduce additive noise disturbances into the reaction wheel model. This is done in order to account for both sensor noise, as well as for modelling inaccuracies. The joint covariance matrix of $v(t)$, and $w(t)$ is given by (4.17).

$$E\left[\begin{bmatrix} v(t) \\ w(t) \end{bmatrix} \cdot \begin{bmatrix} v(t)^T & w(t)^T \end{bmatrix}\right] = \begin{bmatrix} R & S^T \\ S & Q \end{bmatrix} \cdot \sigma(t) \tag{4.17}$$

where $Q = Q^T,\ Q \succ 0,\ Q \in \mathbb{R}^{n_{x_a} \times n_{x_a}}$, and $R = R^T,\ R \succ 0,\ R \in \mathbb{R}^{n_y \times n_y}$, with

$$\sigma(t) = \begin{cases} 1, \text{ for } t = 0 \\ 0, \text{ for } t \neq 0 \end{cases} \tag{4.18}$$

and with

$$E\Big[v(t)\Big] = E\Big[w(t)\Big] = 0 \tag{4.19}$$

Since $v(t)$, and $w(t)$ are assumed to not be correlated, the cross-covariance matrix is set to $S = 0$.

The state estimator dynamics are then defined in (4.20).

$$\begin{aligned} \dot{\hat{x}}_a(t) &= A_a(\rho)\,\hat{x}_a(t) + B_a u(t) + L(\rho)\Big(y(t) - \hat{y}(t)\Big) \\ \hat{y}(t) &= C_a \hat{x}_a(t) \end{aligned} \tag{4.20}$$

where $L(\rho)$ is the observer gain matrix, having an affine parametrisation in $\rho(t)$, as described in (4.21).

$$L(\rho) = L_0 + \rho_1 \cdot L_1 + \rho_2 \cdot L_2 + \rho_3 \cdot L_3 \tag{4.21}$$

The dynamics of the estimation error, $\xi_a(t) = x_a(t) - \hat{x}_a(t),\ \xi_a(t) \in \mathbb{R}^{n_{x_a}}$, are described in (4.22).

$$\dot{\xi}_a(t) = \Big(A_a(\rho) - L(\rho) \cdot C_a\Big) \cdot \xi_a(t) + \Big(w(t) - L(\rho) \cdot v(t)\Big) \tag{4.22}$$

As can be observed from (4.22), the error dynamics are driven by the measurement noise signal $v(t)$, and by the process noise signal $w(t)$. It must be noted that the expected value of the estimation error, $E\Big[\xi_a(t)\Big]$, is a deterministic, time-varying quantity, described by the relation given in (4.23).

$$E\Big[\dot{\xi}_a(t)\Big] = \Big(A_a(\rho) - L(\rho) \cdot C_a\Big) \cdot E\Big[\xi_a(t)\Big] \tag{4.23}$$

The goal of the observer is to obtain an accurate, un-biased estimate of the augmented state vector, $\hat{x}_a(t)$, by employing knowledge of the reaction wheel's state dynamics, as well as measurements of a part of the system's states. In order to obtain an un-biased estimate, the expected value of the estimation error, $E\Big[\xi_a(t)\Big]$, must go to zero over time, as described by (4.24).

$$\lim_{t\to\infty} E\Big[\xi_a(t)\Big] = 0 \tag{4.24}$$

The condition for an un-biased estimate, described in (4.24), is fulfilled if the matrix $A_a(\rho) - L(\rho) \cdot C_a$ is Hurwitz.

In order to obtain an accurate estimate, the mean squared estimation error must be minimized. This is equivalent to minimizing the variance of the estimation error, given in (4.25).

$$P(t) = E\Big[\xi_a(t) \cdot \xi_a^T(t)\Big] \tag{4.25}$$

with $P(t) = P^T(t),\ P(t) \succ 0,\ P(t) \in \mathbb{R}^{n_{x_a} \times n_{x_a}}$ being the estimation error covariance matrix. The diagonal of the covariance matrix $P(t)$ contains the estimation error variance of each state of the augmented reaction wheel model, as shown in (4.26).

$$P(t) = \begin{bmatrix} E\Big[\xi_{a_1}(t) \cdot \xi_{a_1}^T(t)\Big] & E\Big[\xi_{a_1}(t) \cdot \xi_{a_2}^T(t)\Big] & \cdots & E\Big[\xi_{a_1}(t) \cdot \xi_{a(n_{x_a}-1)}^T(t)\Big] & E\Big[\xi_{a_1}(t) \cdot \xi_{a_{n_{x_a}}}^T(t)\Big] \\ E\Big[\xi_{a_2}(t) \cdot \xi_{a_1}^T(t)\Big] & E\Big[\xi_{a_2}(t) \cdot \xi_{a_2}^T(t)\Big] & \cdots & E\Big[\xi_{a_2}(t) \cdot \xi_{a(n_{x_a}-1)}^T(t)\Big] & E\Big[\xi_{a_2}(t) \cdot \xi_{a_{n_{x_a}}}^T(t)\Big] \\ \vdots & \vdots & \ddots & \vdots & \vdots \\ E\Big[\xi_{a_{n_{x_a}}}(t) \cdot \xi_{a_1}^T(t)\Big] & E\Big[\xi_{a_{n_{x_a}}}(t) \cdot \xi_{a_2}^T(t)\Big] & \cdots & E\Big[\xi_{a_{n_{x_a}}}(t) \cdot \xi_{a(n_{x_a}-1)}^T(t)\Big] & E\Big[\xi_{a_{n_{x_a}}}(t) \cdot \xi_{a_{n_{x_a}}}^T(t)\Big] \end{bmatrix} \tag{4.26}$$

Since the trace of the estimation error covariance matrix $P(t)$ represents the sum of the mean squared estimation errors, it directly follows that by minimizing the value of the trace of $P(t)$, the mean squared estimation error of each state is also minimized.

Seeing that the estimation error covariance matrix, $P(t)$, is time-variant, its rate of change, $\dot{P}(t)$, can be computed. First, the initial relation for $\dot{P}(t)$ is given in (4.27).

$$\dot{P}(t) = E\Big[\dot{\xi}_a(t) \cdot \xi_a^T(t) + \xi_a(t) \cdot \dot{\xi}_a^T(t)\Big] \tag{4.27}$$

By expanding (4.27), the explicit relation for $\dot{P}$ is given in (4.28).

$$\dot{P}(t) = \Big(A_a(\rho) - L(\rho) \cdot C_a\Big) \cdot P(t) + P(t) \cdot \Big(A_a(\rho) - L(\rho) \cdot C_a\Big)^T + Q + L(\rho) \cdot R \cdot L^T(\rho) \tag{4.28}$$

Since the objective is to minimize the steady-state estimation error, $\xi_a(t)$, the steady-state value, P_{ss}, of the covariance matrix , $P(t)$, must be minimized. Evidently, the covariance matrix reaches steady-state when its rate of change becomes zero, i.e. $\dot{P}(t) = 0$. The optimization problem, described in (4.29), can, thus, be formulated in order to obtain the minimum variance reaction wheel state estimates.

$$\begin{aligned} &\underset{L(\rho),\, P_{ss}}{\text{minimize}} && \operatorname{trace}(P_{ss}) \\ &\text{subject to} && \Big(A_a(\rho) - L(\rho) \cdot C_a\Big) \cdot P_{ss} + P_{ss} \cdot \Big(A_a(\rho) - L(\rho) \cdot C_a\Big)^T + Q + L(\rho) \cdot R \cdot L^T(\rho) = 0, \\ &&& P_{ss} \succ 0. \end{aligned} \tag{4.29}$$

As it can be observed, the optimization given in (4.29) is subject to an equality constraint. This constraint is, in fact, an algebraic Ricatti equation (ARE), which can be replaced by an algebraic Riccati inequality (ARI), by choosing an appropriate matrix $X = X^T,\ X \succ 0,\ X \in \mathbb{R}^{n_{x_a} \times n_{x_a}}$, such that $X \succ P_{ss}$. Thus, the optimization problem in (4.29) can be re-formulated to the problem described in (4.30).

$$\begin{aligned} &\underset{L(\rho),\, X}{\text{minimize}} && \operatorname{trace}(X) \\ &\text{subject to} && A_a(\rho) \cdot X - L(\rho) \cdot C_a \cdot X + X \cdot A_a^T(\rho) - X \cdot C_a \cdot L^T(\rho) + Q + L(\rho) \cdot R \cdot L^T(\rho) \prec 0, \\ &&& X \succ 0. \end{aligned} \tag{4.30}$$

By utilizing a congruence transformation with $Y = X^{-1}$, then introducing $Z(\rho) = Y \cdot L(\rho)$, and applying the Schur complement twice [6], the optimization problem defined in (4.30) is transformed into the optimization problem given in (4.31).

$$\begin{aligned} &\underset{Y,\, Z(\rho)}{\text{maximize}} \quad \operatorname{trace}(Y) \\ &\text{subject to} \quad \begin{bmatrix} -\left(Y \cdot A_a(\rho) - Z(\rho) \cdot C\right) - \left(Y \cdot A_a(\rho) - Z(\rho) \cdot C\right)^T & Y & Z(\rho) \\ Y & Q^{-1} & 0 \\ Z^T(\rho) & 0 & R^{-1} \end{bmatrix} \succ 0. \end{aligned} \tag{4.31}$$

The optimization problem given in (4.31) is then solved with the help of the YALMIP toolbox [18], [19].

4.2.5. Performance Evaluation

In order to explore the possibility of using less sensors on the reaction wheel system, two observers have been synthesised using the same technique that is presented in Section 4.2.4. The first observer is designed using all the measurements available on the reaction wheels (**FS** will be used as the identifier for this observer), while the second one uses only Hall-sensor based rotor position and angular velocity measurements (**HS** will be used as the identifier for this observer).

Performance evaluation tests have been developed in order to study the behaviour of the two designed observers. The steady-state accuracy test, performed in Section 4.2.5.1, allows the verification of the achievable state estimation accuracy of each observer. The zero-speed crossing tests, discussed in Section 4.2.5.2, show to what extent the two observers can handle the reduced amount of rotor position and speed measurement data, which occurs around zero angular velocity. The observer robustness test s, performed in Section 4.2.5.3, are meant to bring out the ability of the designed observers to cope with modelling inaccuracies, as well as with certain temperature measurement inaccuracies.

4.2.5.1. Steady-State Accuracy

For the steady-state accuracy test, the reaction wheel system simulation is driven to an angular velocity of approximately $260\ rad/s$ (reached at approximately $t = 6$ seconds), and held at that rotation speed, all while computing the state estimation error. The observer error distribution is then obtained using the data collected between $t = 20$ seconds, and $t = 30$ seconds.

The full sensor information observer (FS observer) is the first to be tested. The estimation error over time is presented in Figure 4.7, and the observer error distribution, together with a beta distribution fit, is presented in Figure 4.9.

As it can be observed, the direct current, i_d, and quadrature current, i_q, estimate errors have standard deviations of $\sigma_{i_d} = 134.287\ \mu A$, and $\sigma_{i_q} = 5.152\ \mu A$, respectively. As it can be observed from Figure 4.9, estimate errors have means $\mu_{i_d} = -448.286\ \mu A$, and $\mu_{i_q} = 16.495\ \mu A$. This is presumably due to the fact that the estimated angular position is used in the Park transform that is used to obtain the i_d, and i_q current vectors. Moreover, the inverse Park transform is used to transform the direct and quadrature voltages, v_d, and v_q, respectively, into the the three phase voltages used to drive the wheel's motor. Thus, the non-zero mean values of the two current vectors appear due to the sensitivity of the Park and inverse Park transforms to small inaccuracies in the position value.

The position estimation error has a very small, non-zero mean $\mu_{\theta_e} = -7.467 \cdot 10^{-5}\ rad$, and a standard deviation of $\sigma_{\theta_e} = 2.554 \cdot 10^{-4}\ rad$. Seeing that the rotor electrical position, obtained purely from the Hall sensors, results in a peak position error of $\pm 0.5236\ rad$ (i.e. $\pm\pi/6\ rad$), the 5σ accuracy band of the estimated rotor position error (i.e. $\pm 12.77 \cdot 10^{-4}\ rad$) shows a factor of 410 improvement in the rotor position information.

In the case of the angular velocity, ω_m, the state observer is able to provide an estimate with a standard deviation $\sigma_{\omega_m} = 2.191 \cdot 10^{-3}\ rad/s$. Considering that the objective for angular velocity control accuracy is to have an accuracy of $\pm 0.1\ rad/s$, the 5σ accuracy band of the obtained angular velocity estimate is $\pm 10.955 \cdot 10^{-3}\ rad/s$, thus, the estimate easily fulfils the requirement.

The Hall-sensor only observer (HS observer) estimation error over time is presented in Figure 4.8, and the error distribution, together with a beta distribution fit, is presented in Figure 4.10. As can be observed from the estimation error distribution, the direct current, i_d, and quadrature current, i_q, estimates have standard deviations of $\sigma_{i_d} = 3236.117\ \mu A$, and $\sigma_{i_q} = 117.289\ \mu A$, respectively. The non-zero mean of the two current vector estimations is due to the inverse Park transform that is used to obtain the three-phase voltages from v_d, and v_q. Since the inverse Park transform is sensitive to the inaccuracies of the estimated position used in it, the mismatch in the current estimate appears.

The estimate of the angular velocity, ω_m, has a standard deviation $\sigma_{\omega_m} = 7.392 \cdot 10^{-3}\ rad/s$, for which the 5σ accuracy band (i.e. $\pm 36.96 \cdot 10^{-3}\ rad/s$) also satisfies the required estimation accuracy for angular velocity control within $\pm 0.1\ rad/s$. The rotor electrical angular position estimation has a standard deviation of $\sigma_{\theta_e} = 6.605 \cdot 10^{-3}\ rad$, giving a factor of 15.8 improvement in the rotor position information, when considering the 5σ accuracy band of the estimated rotor position error (i.e. $\pm 33.025 \cdot 10^{-3}\ rad$).

It is worth noting that the accuracy of the state estimates, obtained by using the HS observer is, in fact, dependent on the angular velocity of the reaction wheel since it decreases with an increasing angular velocity, which can be observed in Figure 4.14. This behaviour is due to the fact that the frequency of position and velocity measurement updates, obtained only from the wheel's Hall sensors, rises with the increase of the reaction wheel angular velocity.

Lastly, the estimation error distribution of the HS observer can be explained by the fact that the observer uses only Hall-sensor based measurements. As it can be observed from Figure 4.8, the state estimate error is characterised by a 'spiky' profile. These spikes occur at the time of every Hall sensor transition, thus, the estimation error shape in between two Hall sensor transitions can be viewed as the observer interpolating in between samples.

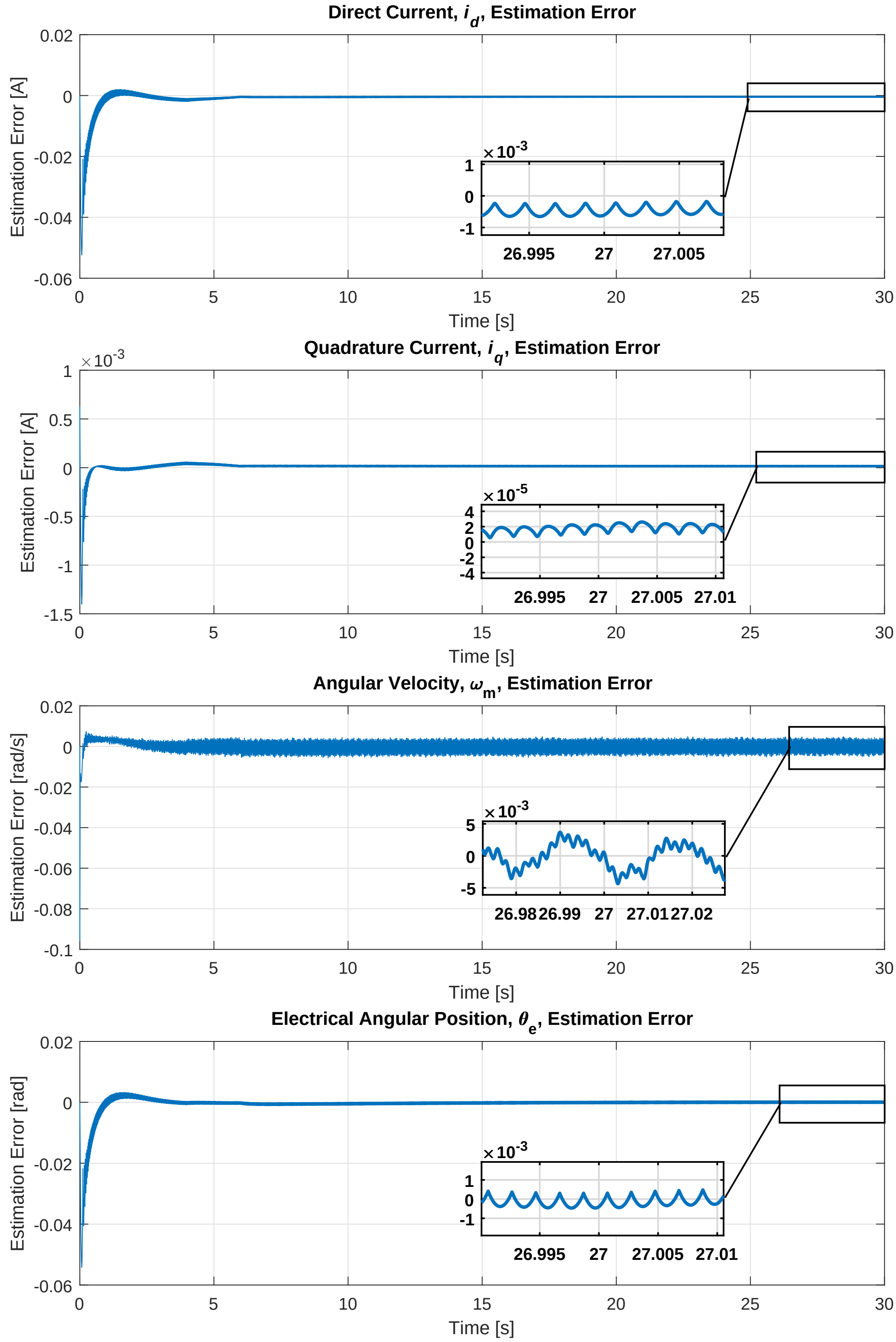

Figure 4.7: Estimation error of the reaction wheel states, in steady-state. Evaluation performed at $\omega_m \approx 260\ rad/s$, constant angular velocity. Sensing of i_d, i_q, ω_m, and θ_e.

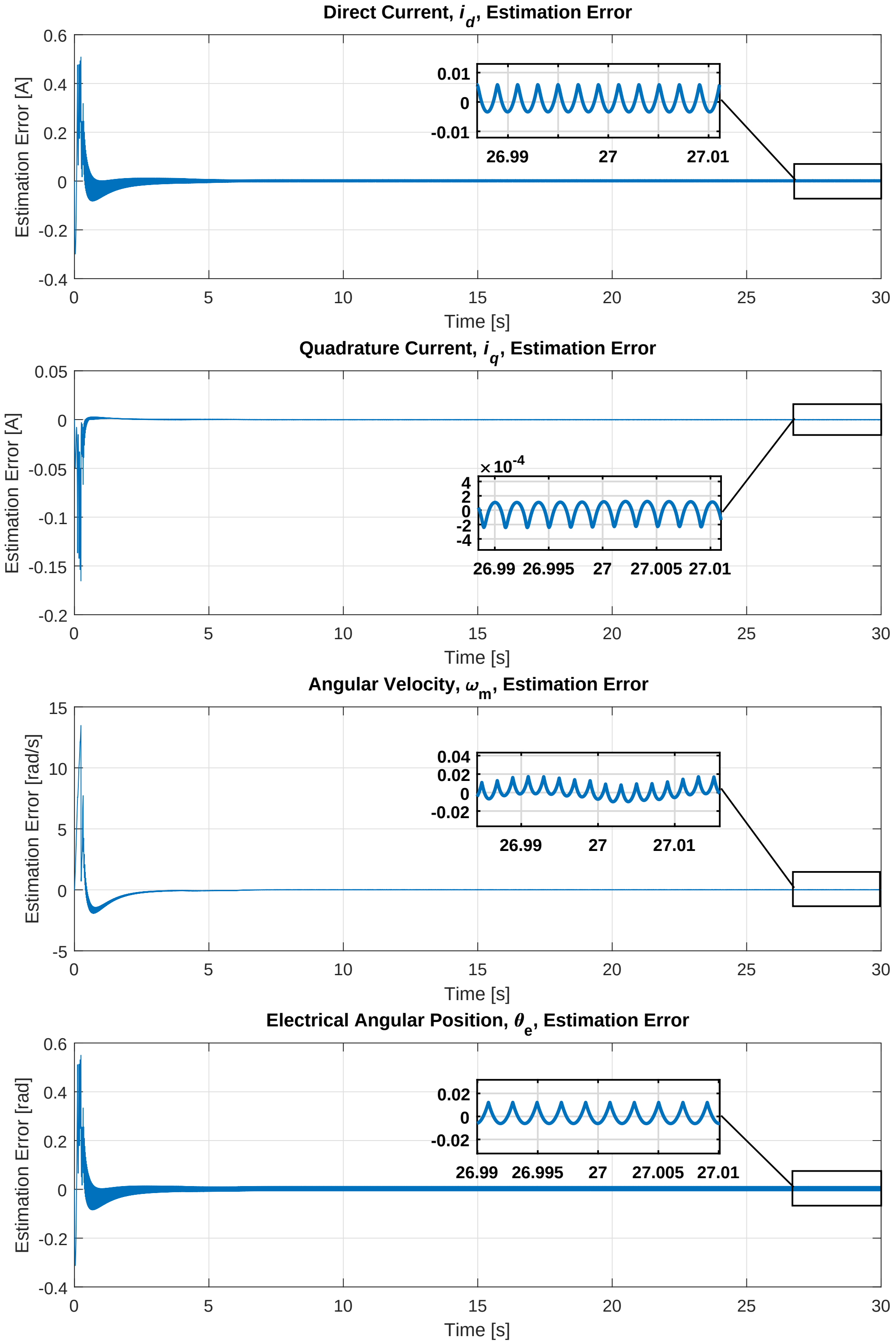

Figure 4.8: Estimation error of the reaction wheel states, in steady-state. Evaluation performed at $\omega_m \approx 260\ rad/s$, constant angular velocity. Sensing of ω_m, and θ_e only. No current sensing.

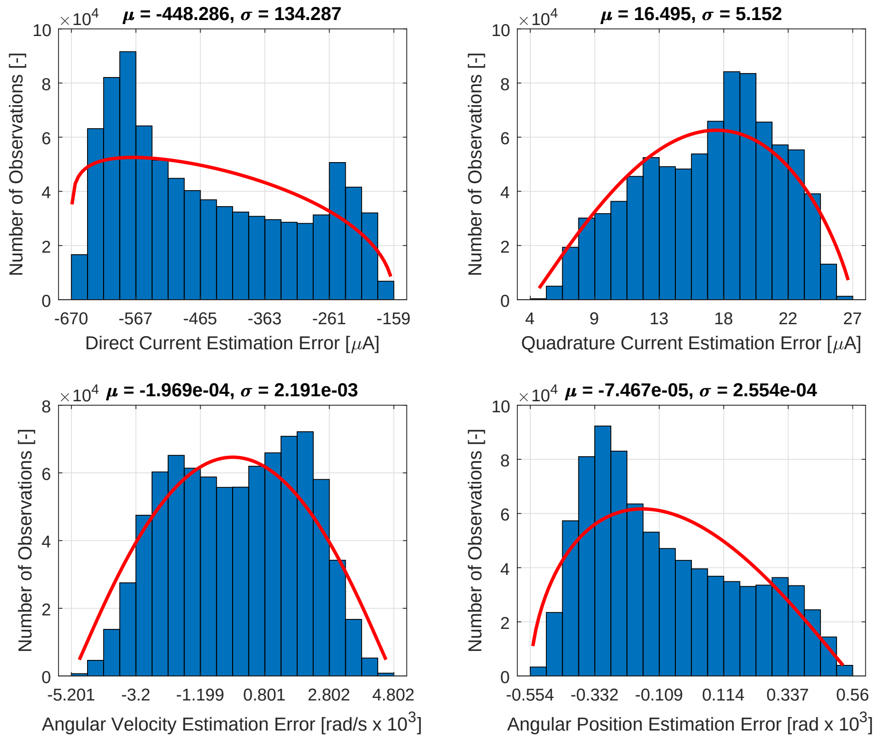

Figure 4.9: Estimation error distribution of the reaction wheel states. Evaluation performed at $\omega_m \approx 260\ rad/s$, constant angular velocity. Sensing of i_d, i_q, ω_m, and θ_e.

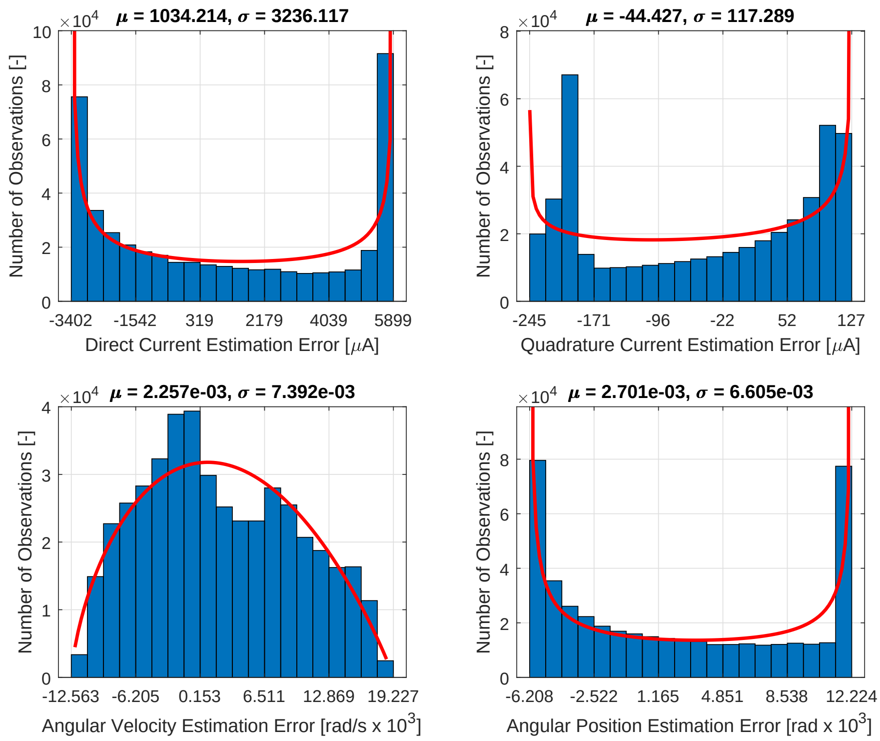

Figure 4.10: Estimation error distribution of the reaction wheel states. Evaluation performed at $\omega_m \approx 260\ rad/s$, constant angular velocity. Sensing of ω_m, and θ_e only. No current sensing.

4.2.5.2. Zero-Speed Crossing Analysis

In the case of the zero-speed crossing test, the reaction wheel system simulation is first driven to an angular velocity of approximately $40\ rad/s$ (reached at approximately $t = 3$ seconds), after which it is driven to $-40\ rad/s$ (reached at approximately $t = 12$ seconds). This results in a zero-speed crossing, at $t = 8.5$ seconds, with a deceleration/acceleration value of $20\ rad/s^2$.

The behaviour of the FS observer estimation error during the zero-speed crossing is shown in Figure 4.11. As it can be observed, all state estimates are affected by the zero-speed crossing. In the case of the angular position estimate, a maximum deviation of $\approx 0.13\ rad$ occurs. The direct current, i_d, and the quadrature current, i_q, have peak deviations of $\approx 0.05\ A$, and $\approx 0.0036\ A$, respectively. Once again, due to the fact that the position dependent Park and inverse Park transforms are used, the current measurements in the rotating reference frame are linked to the angular position behaviour. The angular velocity estimate has a maximum deviation of $\approx -0.08\ rad/s$, which is still within the $0.1\ rad/s$ requirement.

The estimation error of the HS observer during the zero-speed crossing is far worse, as can be observed in Figure 4.12. This is to be expected, since this observer relies solely on the Hall sensor measurements. A particularly interesting phenomenon can be observed, namely the fact that the estimate errors for the currents and the angular velocity start to deviate well before the reaction wheel simulation is close to crossing zero-speed. This phenomenon appears due to two factors. First, the angular deceleration/acceleration causes the real angular velocity of the reaction wheel to not match the angular velocity obtained from Hall-sensor measurements, due to the inherent averaging property of the Hall-sensor based measurement. Secondly, the low angular velocity results in low frequency updates of the velocity measurement. Thus, digital Hall-sensor based measurements of the rotation speed cannot capture the fast changes in the angular velocity caused by a high angular deceleration/acceleration value.

4.2.5.3. Robustness Analysis

Micro-vibration Disturbances Micro-vibration disturbances are present throughout all the performed simulations/tests, since they have been included into the reaction wheel simulation. As it can be observed from the performance results, both observer types are able to handle the micro-vibration disturbances while also maintaining a high accuracy for the state estimates.

Friction Curve Mismatch In this test case, both observer types are used to estimate the states of the reaction wheel system that has a completely different friction curve than what the observer model contains. Thus, the reaction wheel simulation contains the friction curve for the reaction wheel at $-20°C$, while the observer model contains the friction curve specific to the reaction wheel at $+40°C$. Both friction curves have been discussed in Section 3.1. The simulated wheel is first driven to $35\ rad/s$, held constant until $t = 6$ seconds, then the driving voltage is increased to its maximum value (reached at $t = 15$ seconds), following a ramp profile. The simulation is run for another 10 seconds from that point (i.e. the simulation is run for a total of 25 seconds). Therefore, this test goes through the entire, one-sided, speed range of the wheel.

As it can be observed from both Figure 4.13, and Figure 4.14, the state estimation error of both observers is not affected by the mismatching friction curves. The same test profile is run for precisely matching friction curves, in order to act as a check for the behaviour of the two observers. However, the results from that test run do not need to be displayed, since they are the same as the results shown in Figure 4.13, and Figure 4.14.

The behaviour of the FS observer can be explained by the fact that it converges rather slow, thus, requiring a longer time to converge when the reaction wheel is accelerating. Furthermore, with the increasing angular velocity, the micro-vibration disturbances' effect on the estimates becomes more visible. Hence the increase in the estimation error amplitude of the quadrature current, and of the angular velocity since these two states are the most sensitive to torque variations. Nonetheless, even when not yet converged, the estimated states obtained by the FS observer are still approximately a factor 2 better than the converged state estimates of the HS observer.

In the case of the HS observer, the transient behaviour shown at $t = 6$ seconds is due to the increase in angular acceleration of the wheel. The observer is quicker to converge than the FS observer, however, the state estimates are not as accurate.

Stator Coil Resistance Mismatch For the coil resistance mismatch test, the reaction wheel system simulation is driven to an angular velocity of approximately $260\ rad/s$ (reached at approximately $t = 6$ seconds), and held at that rotation speed. This is then followed by a ramp-like temperature change, starting from $+30°C$, at $t = 10$ seconds, and ending with $+36°C$, at $t = 14$ seconds, resulting in the variation of the stator coil's resistance.

The FS observer is rather slow in cancelling out the estimation error (bias) introduced by the coil temperature mismatch into the angular velocity and position, as can be observed from Figure 4.15. It is possible to tune the FS observer in order to obtain a better behaviour, however, due to time constraints, this has not been investigated further.

The HS observer, as expected, is not able to account for this mismatch (see Figure 4.16), due to the fact that it does not have any way of detecting it. However, the angular velocity and position estimates are not affected by this coil resistance mismatch. It should be noted that the estimation error of the direct current, i_d, is so high that the effect of the coil resistance mismatch is not visible.

4.3. Conclusion

In the first part of this chapter, a method is proposed for determining the real position of the Hall-effect sensors around the stator of the reaction wheel motor. The performance of the method is evaluated for different sampling rates, showing that its estimation error reduces with increasing sampling rate.

Throughout the second part of this chapter, two LPV reaction wheel state estimators are designed and synthesised. The first observer (FS) makes use of phase current, angular position, and angular velocity measurements, while the second observer (HS) uses only angular position and velocity measurements. The accuracy, as well as the robustness against reaction wheel disturbances of the state estimators are evaluated.

Both observers are able to provide current, angular position and velocity information with a greatly improved accuracy. While both estimators are robust against friction mismatch, only the FS observer is able to eventually compensate for stator coil resistance mismatches. The FS observer, however, is slower in converging than the HS observer.

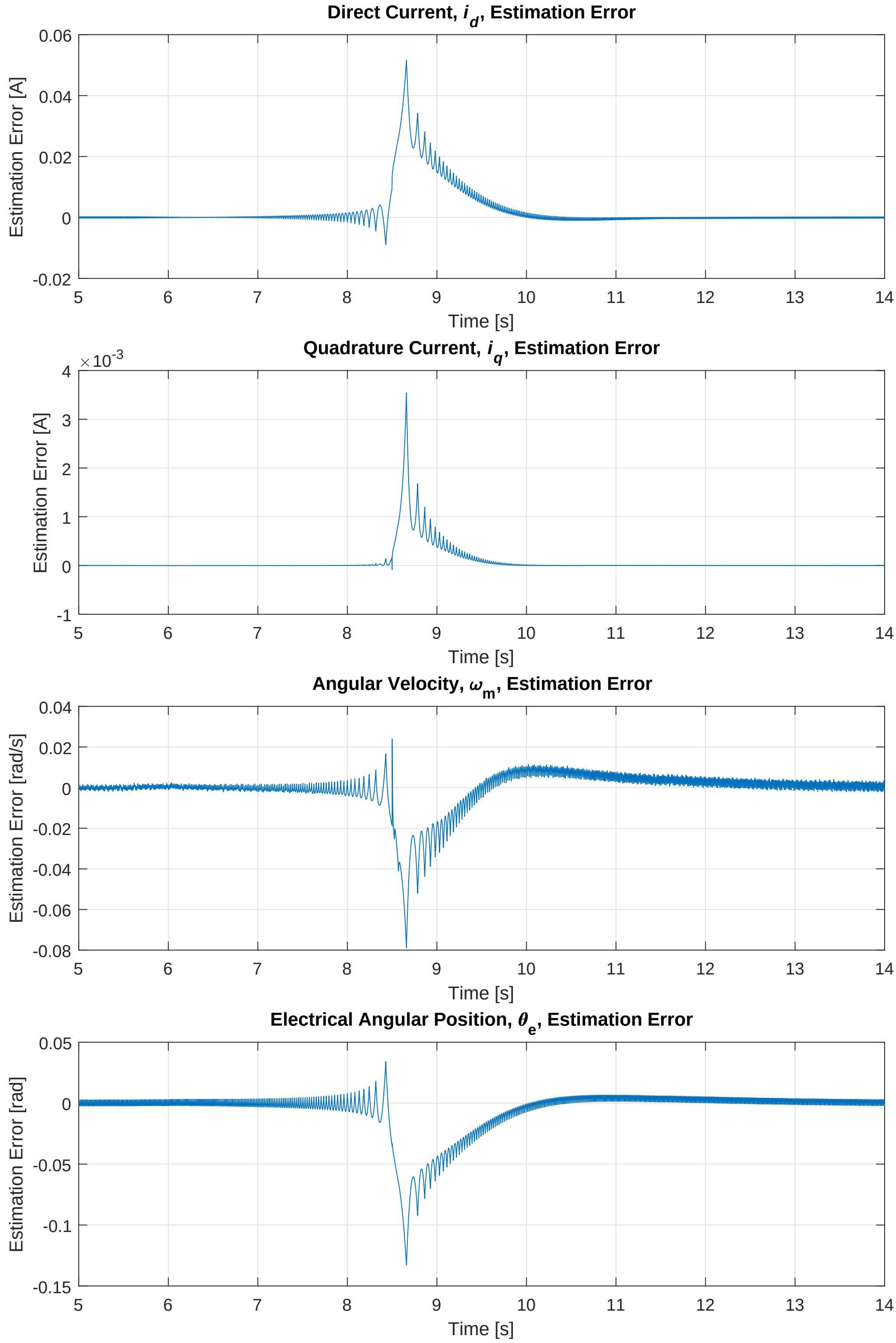

Figure 4.11: Estimation error of the reaction wheel states during a change in the spinning direction of the reaction wheel (zero-speed crossing), at $t \approx 8.5\ s$. Sensing of i_d, i_q, ω_m, and θ_e.

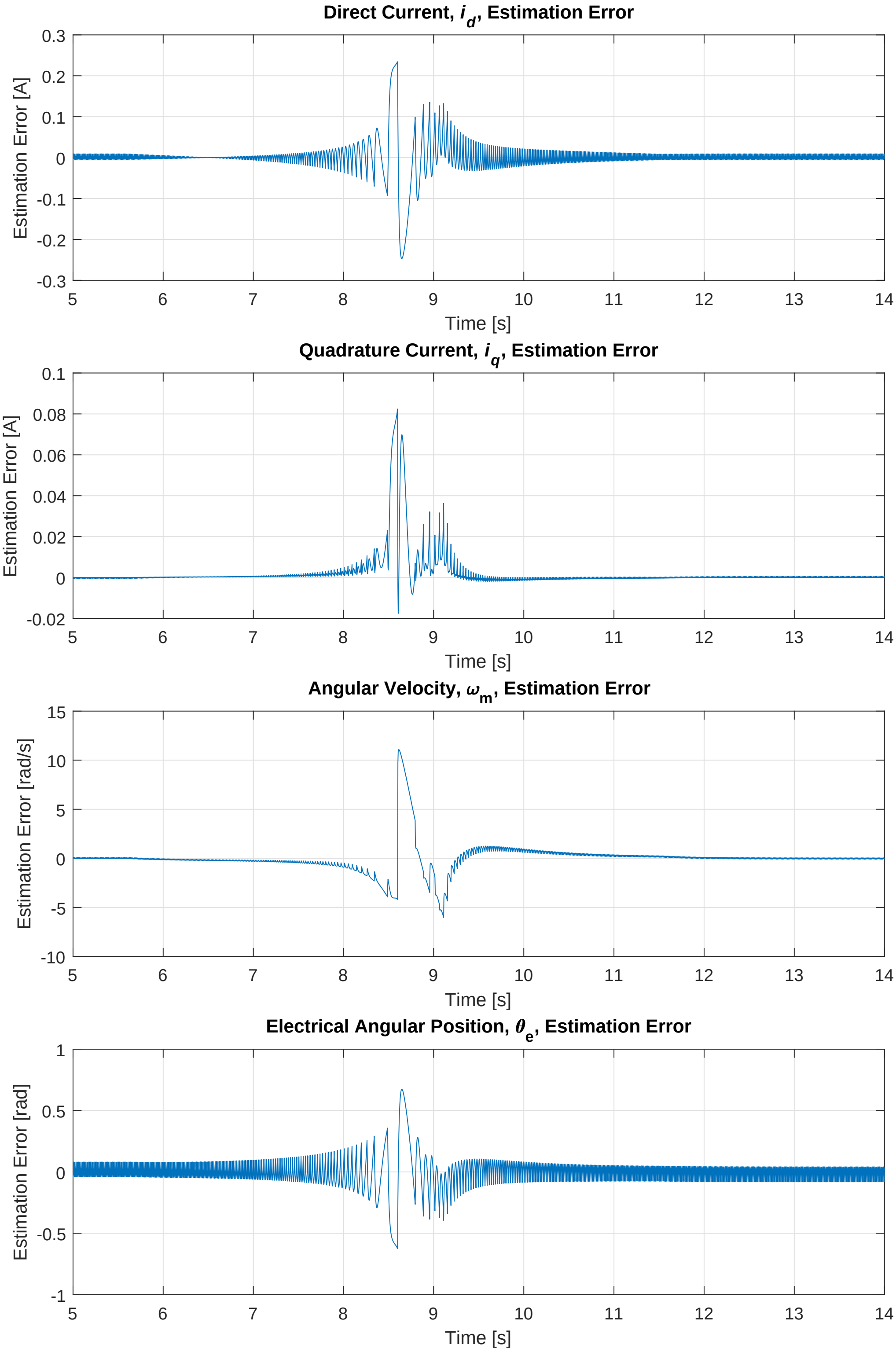

Figure 4.12: Estimation error of the reaction wheel states during a change in the spinning direction of the reaction wheel (zero-speed crossing), at $t \approx 8.5\ s$. Sensing of ω_m, and θ_e only. No current sensing.

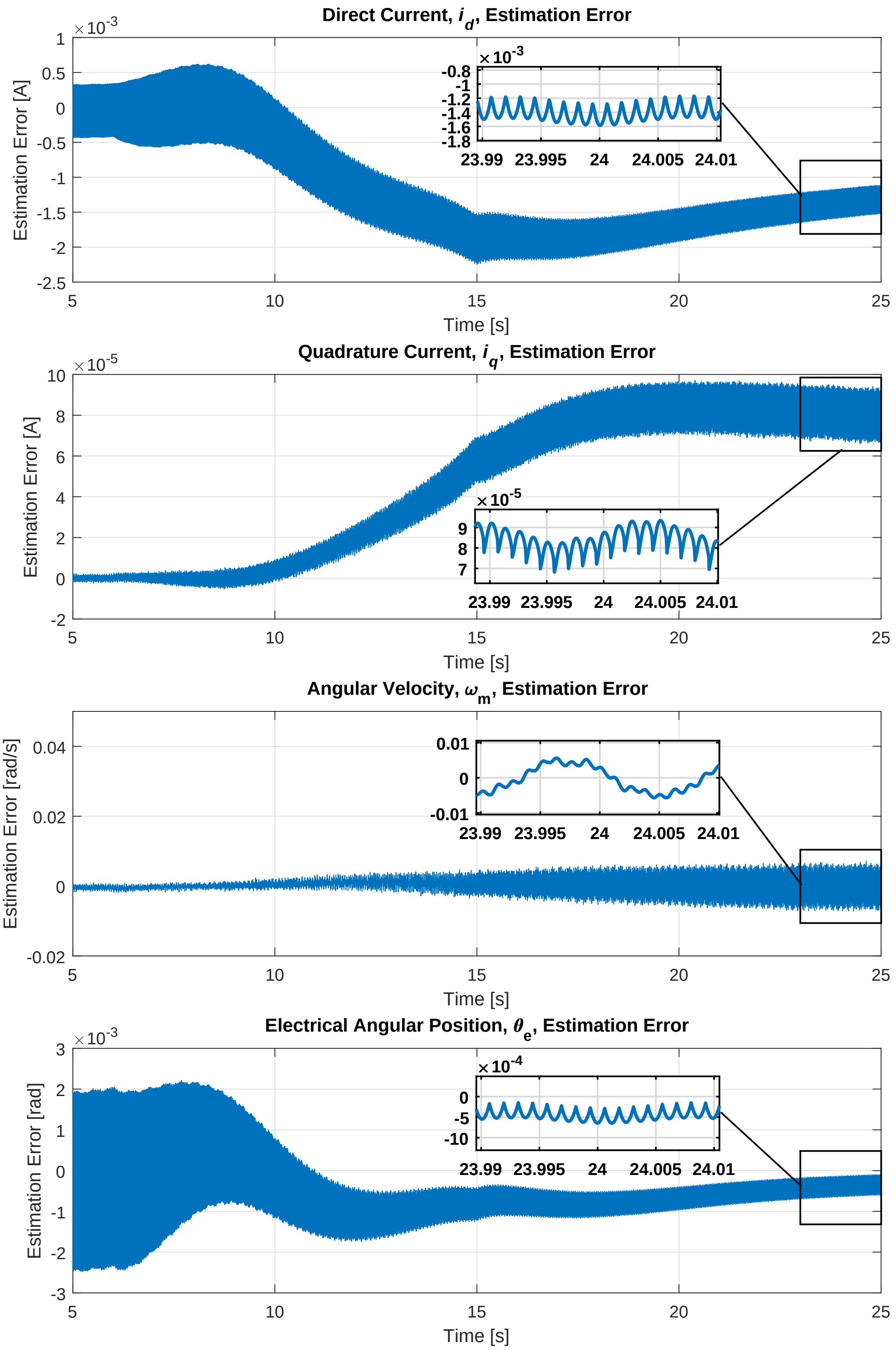

Figure 4.13: Estimation error of the reaction wheel states, using an incorrect friction curve. Sensing of i_d, i_q, ω_m, and θ_e.

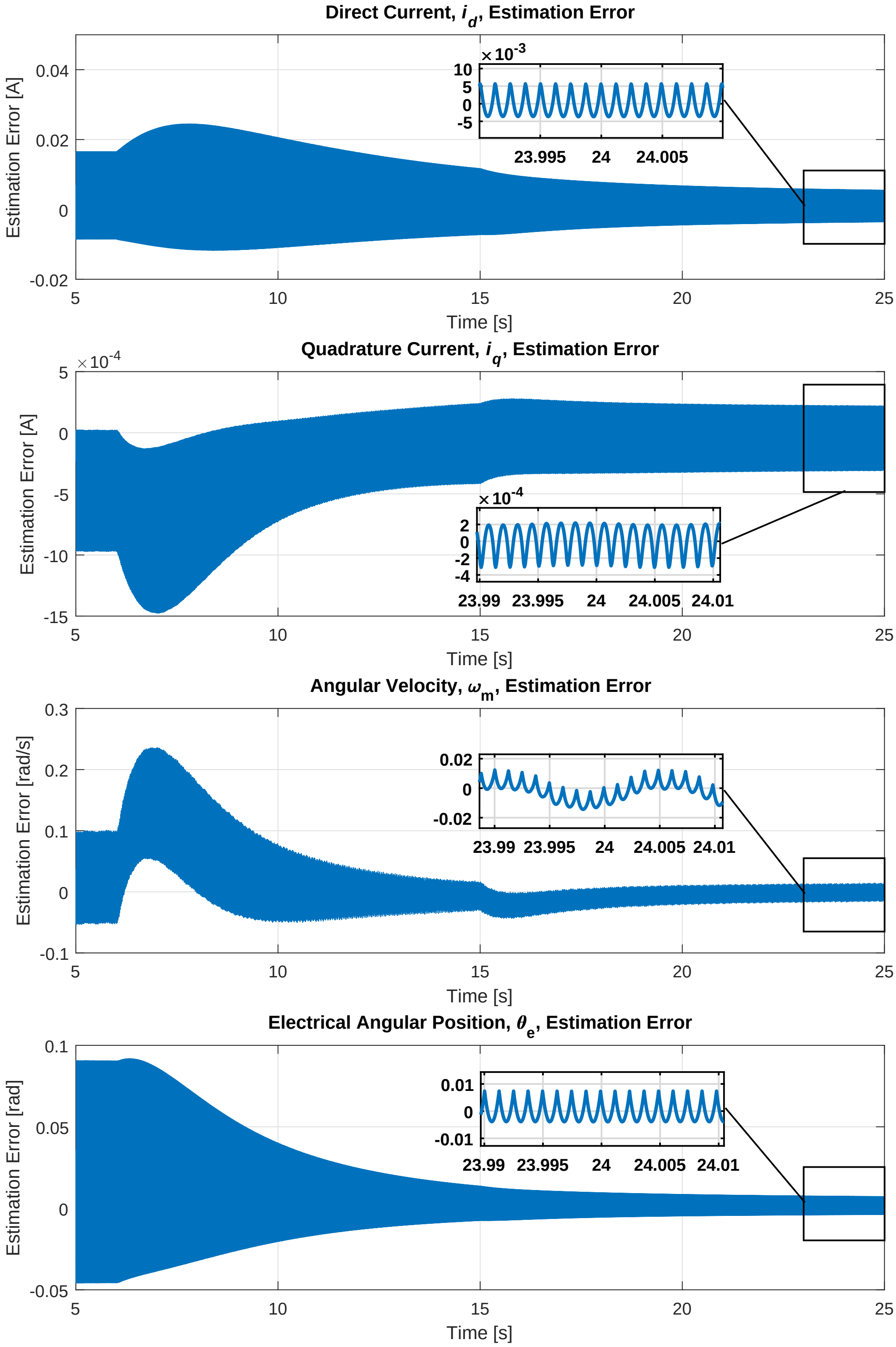

Figure 4.14: Estimation error of the reaction wheel states, using an incorrect friction curve. Sensing of ω_m, and θ_e only. No current sensing.

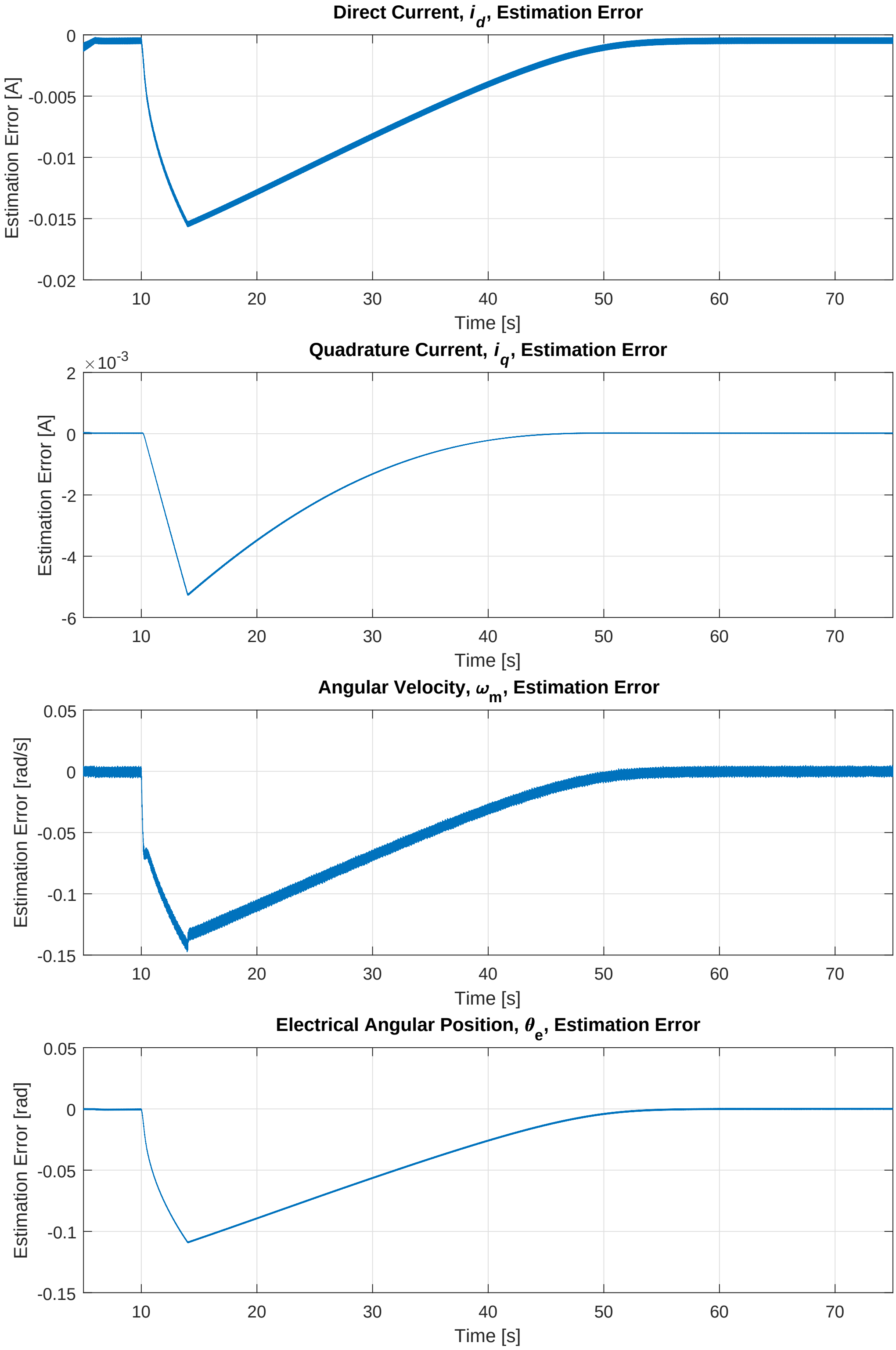

Figure 4.15: Estimation error of the reaction wheel states, using inaccurate stator coil temperature measurements. Sensing of i_d, i_q, ω_m, and θ_e.

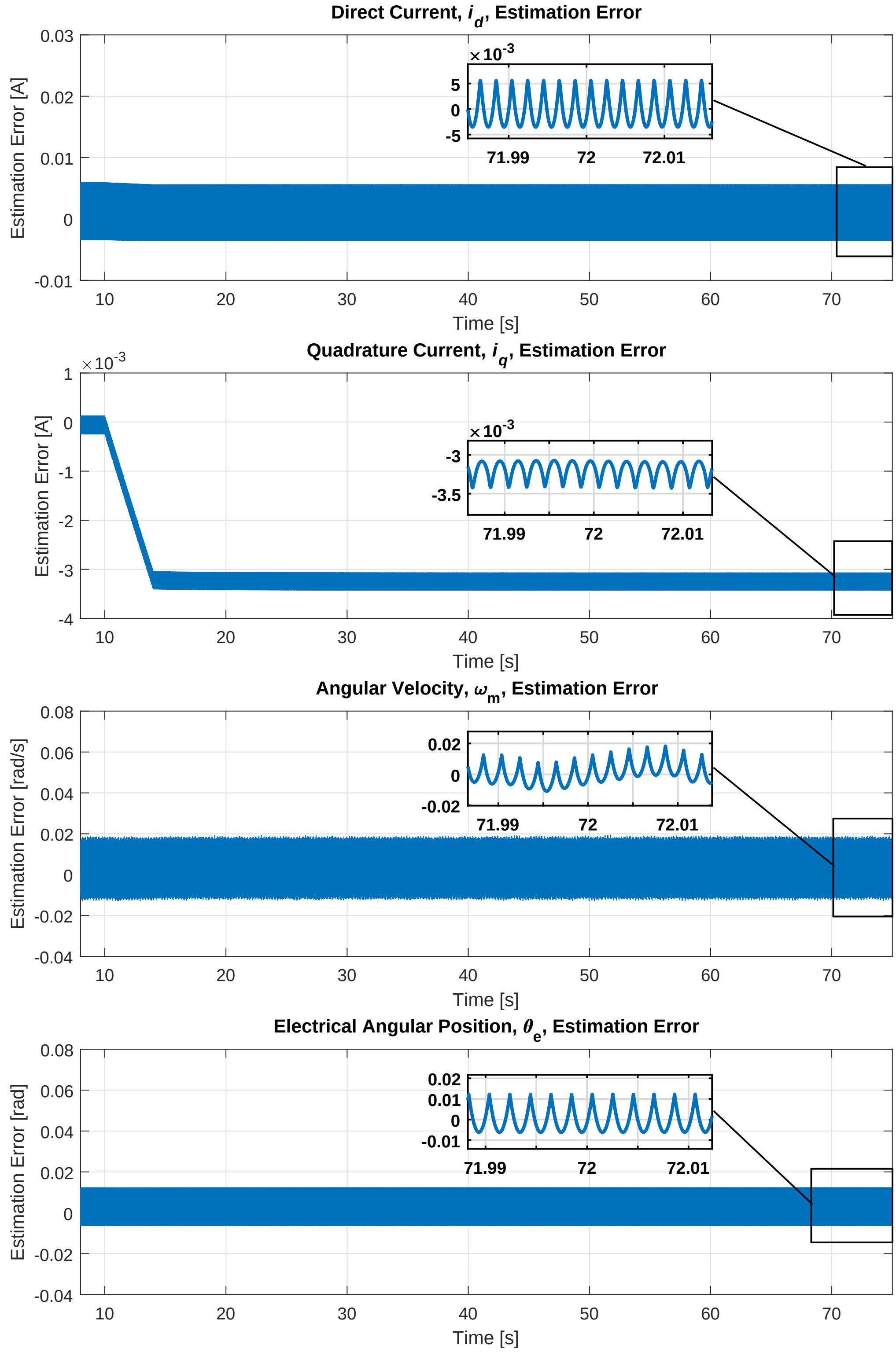

Figure 4.16: Estimation error of the reaction wheel states, using inaccurate stator coil temperature measurements. Sensing of ω_m, and θ_e only. No current sensing.

5 Conclusions and Recommendations

In this final chapter, conclusions are drawn, in Section 5.1, on the work that has been carried out throughout the thesis. A few recommendations for future investigation are then given in Section 5.2.

5.1. Conclusions

The work performed throughout the project has led to various degrees of completion of the objectives described in Chapter 1. The main objective of obtaining an un-biased, higher accuracy estimate of the reaction wheel states (i.e.: angular position, angular velocity, and currents) has been achieved. This objective has been achieved in two steps, as described in Chapter 4. First, a Hall sensor position estimator is designed, and verified. This estimator is then used to compensate the error in the Hall-sensor based rotor position measurements.

In the second step, two quasi-LPV state observers (one making use of both Hall-sensor and current sensor measurements - FS observer, and the other making use of only the Hall-sensor measurements - HS observer) are formulated as optimization problems, subjected to parameter dependent matrix inequalities. The accuracy of each of the two observers is then verified using the detailed simulation of the HT-RW4xx reaction wheel that has been developed throughout Chapter 2, and Chapter 3. Both observers provide a highly improved estimate of the reaction wheel states. As expected, the FS observer provides a better estimate of the position, and velocity of the reaction wheel throughout its entire speed range. However, the estimate of the HS observer improves with increasing angular velocity.

The robustness of the two observers is also evaluated by using the detailed RW model. Both estimators show very good behaviour in the face of friction curve mismatches, and micro-vibration type disturbances. In the case of stator coil resistance mismatch, the FS observer is able to eventually eliminate the bias that is introduced in the estimates, while the HS observer is not able to eliminate the bias due to the fact that it does not contain any precaution for this case.

It can, thus, be concluded that a significantly higher accuracy reaction wheel state estimate can be obtained. Hall-sensor only measurements can be used for state estimation, however, the HS sensor is subject to more issues. Nonetheless, a method that returns an accurate stator coil resistance value will improve the performance of both the FS, and the HS observers.

5.2. Recommendations and Future Work

As observed from Section 4.2.5.3, the FS observer is rather slow in rejecting the error introduced by the mismatching coil resistance values. This is likely due to the fact that the closed-loop poles that correspond to the voltage disturbance, introduced into the current equations, are not fast enough. The issue can be solved by better tuning of the observer, by varying the Q, and R matrices until a better result is obtained, which can become quite cumbersome. One path to explore would be to formulate constraints to the optimization problem used in synthesizing the observer such that the poles are guaranteed to be in a certain region.

The HT-RW4xx reaction wheels have a constant acceleration output mode that is currently implemented as a ramp, with an adjustable slope, which is used as the reference input for the wheel's angular velocity controller. By expanding the state vector of the observer model to include the angular acceleration of the wheel, it will give the possibility to directly control the angular acceleration, and, thus, the output torque of the reaction wheel.

Determining the resistance of the stator coil proved to be of high importance since it has a significant impact on the state estimator's performance. Knowing that the coil resistance varies with temperature, placement of the coil temperature sensor is crucial. Additional characterisation of the stator coil resistance variation over temperature, as measured by the coil temperature sensor, should be performed. Moreover, the coil temperature variation created by the power fed into the motor coil should be characterised as well. These characterisation experiments will allow the improvement of the reaction wheel simulation, and, most importantly, will allow for the implementation of a curve that accurately fits the coil resistance variation over temperature.

Bibliography

[1] What is 'Field Oriented Control' and what good is it? Technical report, Copley Controls Corporation, .

[2] Sensorless Field Oriented Control for Permanent Magnet Synchronous Motors. Presentation, Microchip Technology, 2007.

[3] Park, Inverse Park and Clarke, Inverse Clarke Transformations MSS Software Implementation User Guide. Technical report, Microsemi, 2013.

[4] CubeSat Design Specification . Technical report, California Polytechnic State University, 2014.

[5] Bill Bialke. Microvibration Disturbance Fundamentals for Rotating Mechanisms. In *Proceedings of the 34th Annual AAS Rocky Mountain Section Guidance and Control Conference*, volume 141 of *Advances in the Astronautical Sciences*, February 2011.

[6] Stephen Boyd, Laurent El Ghaoui, Eric Feron, and Venkataramanan Balakrishnan. *Linear Matrix Inequalities in System and Control Theory*, volume 15. SIAM, 1994.

[7] Edoardo Cocci. Optimal Control of Reaction Wheels Disturbance Transients. mathesis, Technische Universiteit Delft, 2016.

[8] Radu-Florin Florea. State Estimation, and Friction Compensation for Brushless DC Motors used in Reaction Wheel Systems. Literature review, TU Delft, 2017.

[9] David Gonçalves, António Vieira, António Carneiro, Armando V. Campos, and Jorge H. O. Seabra. Film Thickness and Friction Relationship in Grease Lubricated Rough Contacts. *Lubricants*, 5(3), 2017. doi: 10.3390/lubricants5030034.

[10] Horst Heimel. Spacewheel Microvibration – Sources, Appearance, Countermeasures. In *8th International ESA Conference on Guidance, Navigation & Control Systems*, 2011.

[11] Jaromír Jezný and Miloslav Čurilla. Position Measurement with Hall Effect Sensors. *American Journal of Mechanical Engineering*, 1(7):231–235, November 2013. doi: 10.12691/ajme-1-7-16.

[12] Sang-Hoon Kim. Chapter 7 - Pulse width modulation inverters. In Sang-Hoon Kim, editor, *Electric Motor Control:DC, AC, and BLDC Motors*, pages 265 – 340. Elsevier, 2017. ISBN 978-0-12-812138-2. doi: 10.1016/B978-0-12-812138-2.00007-6.

[13] Sang-Hoon Kim. Chapter 9 - Speed estimation and sensorless control of alternating current motors. In Sang-Hoon Kim, editor, *Electric Motor Control:DC, AC, and BLDC Motors*, pages 373 – 388. Elsevier, 2017. ISBN 978-0-12-812138-2. doi: 10.1016/B978-0-12-812138-2.00009-X.

[14] Marcus Kirsch, Jim Martin, Mauro Pantaleoni, Richard T. Southworth, Frederic Schmidt, Detlef Webert, and Uwe Weissmann. Cage Instability of XMM-Newton's Reaction Wheels Discovered during the Development of an Early Degradation Warning System. In *AIAA SpaceOps Conference*, 2012.

[15] Tony R. Kuphaldt. *Lessons in Electric Circuits, Volume II - AC*. July 2007.

[16] Marek Lazor and Marek Štulrajter. Modified Field Oriented Control for Smooth Torque Operation of a BLDC Motor. In *2014 ELEKTRO*, pages 180–185, May 2014. doi: 10.1109/ELEKTRO.2014.6847897.

[17] Allan Y. Lee and Eric K. Wang. In-Flight Performance of Cassini Reaction Wheel Bearing Drag in 1997-2013. *Journal of Spacecraft and Rockets*, 52(2):470–480, 2015.

[18] Johan Löfberg. YALMIP : A Toolbox for Modeling and Optimization in MATLAB. In *In Proceedings of the CACSD Conference*, Taipei, Taiwan, 2004.

[19] Johan Löfberg. Automatic robust convex programming. *Optimization methods and software*, 27 (1):115–129, 2012.

[20] F. Landis Markley and John L. Crassidis. *Fundamentals of Spacecraft Attitude Determination and Control*. Springer New York, 2014. URL http://www.ebook.de/de/product/23006812/f_landis_markley_john_l_crassidis_fundamentals_of_spacecraft_attitude_determination_and_control.html.

[21] Doug Sinclair, Cordell C. Grant, and Robert E. Zee. Enabling Reaction Wheel Technology for High Performance Nanosatellite Attitude Control. In *Proceedings of the 21st Annual AIAA/USU Conference on Small Satellites*, 2007.

[22] F. Tahri, A. Tahri, E. A. AlRadadi, and A. Draou. Analysis and control of advanced static var compensator based on the theory of the instantaneous reactive power. In *2007 International Aegean Conference on Electrical Machines and Power Electronics*, pages 840–845, Sept 2007. doi: 10.1109/ACEMP.2007.4510559.

[23] Michel Verhaegen and Vincent Verdult. *Filtering and system identification: a least squares approach*. Cambridge university press, 2007.

[24] Ronny Votel and Doug Sinclair. Comparison of Control Moment Gyros and Reaction Wheels for Small Earth-Observing Satellites. In *Proceedings of the 26th Annual AIAA/USU Conference on Small Satellites*, 2012.